Dynamics on graphs and dynamics of graphs in coupled oscillator systems of small, medium and large sizes

Jüttner, Benjamin

Publication date:
2022

Document Version
Publisher's PDF, also known as Version of record

Dynamics on graphs and dynamics of graphs in coupled oscillator systems of small, medium and large sizes

Benjamin Jüttner

Kongens Lyngby 2022

Technical University of Denmark
Department of Applied Mathematics and Computer Science
Richard Petersens Plads, building 324,
2800 Kongens Lyngby, Denmark
Phone +45 4525 3031
compute@compute.dtu.dk
www.compute.dtu.dk

Summary (English)

We investigate the dynamics of N coupled oscillators on (adaptive) graphs. To make progress on the question how synchronization depends on the graph structure or on how much the graph can adapt, we carry out three studies. Firstly, we study a symmetric system of two populations of nonidentical inhibitory Theta neurons in the $N \to \infty$ limit and investigate the dynamics depending on the inter- and the intra-population coupling. Secondly, we study the stochastic Kuramoto model on graphops (generalized graphs of inifinite size), give a critical coupling strength for the onset of partial coherence, and complement this analytical result with numerical experiments on different (finite) graphs. Finally, we study an adaptive Kuramoto model on (un)directed graphs, mainly for $N = 2$ and partly for $N = 50$ oscillators. Although the most complex dynamical behaviour in our studies requires the graph to be directed and adaptive, complicated behaviour can already occur for perfectly symmetric, nonadaptive systems. Moreover, strong irregularities or a relatively low number of edges can weaken the graph's ability to synchronize the oscillators.

Summary (Danish)

Vi undersøger dynamikken af N koblede oscillatorer på (tilpasselige) grafer. For at gøre fremskridt med spørgsmålet, hvordan synkronisering afhænger af grafstrukturen eller af hvor meget grafen kan tilpasses, udfører vi tre undersøgelser. For det første undersøger vi et symmetrisk system af to populationer af forskellige hæmmende neuroner i $N \to \infty$ grænsen og undersøger dynamikken i forhold til koblingen indenfor og mellem populationerne. For det andet undersøger vi den stokastiske Kuramotomodel på grafoperatorer (generaliserede grafer af uendelig størrelse), giver en kritisk koblingsstyrke for begyndelsen af delvis kohærens, og supplerer dette analytiske resultat med numeriske experimenter på forskellige (endelige) grafer. Til sidst undersøger vi en tilpasselig Kuramotomodel på (u)rettede grafer, hovedsageligt for $N = 2$ og delvist for $N = 50$ oscillatorer. Selvom det mest komplekse adfærd i vores undersøgelser kræver at grafen er rettet og tilpasselig, complicert adfærd kan allerede forekomme for aldeles symmetriske, ikke-tilpasselige systemer. Desuden kan stærke uregelmæssigheder eller et forholdsvis lavt antal kanter svække grafens evne til at synkronisere oscillatorerne.

Preface

This PhD thesis is the final written deliverable in the PhD of Benjamin Jüttner. The PhD programme was carried out from the 15^{th} of September 2019 until the 14^{th} of September 2022 at the Department of Applied Mathematics and Computer Science (DTU Compute), Section for Dynamical Systems. The PhD was supervised by Erik A. Martens, Christian Kuehn, Sune Lehmann Jørgensen, and Poul G. Hjorth.

This PhD thesis is based on the following three articles which result from research carried out during this PhD by Benjamin Jüttner and his collaborators:

Birth and destruction of collective oscillations in a network of two populations of coupled type 1 neurons [1], published in *Chaos*, authored by Benjamin Jüttner, Christian Henriksen, and Erik A. Martens,

Graphop Mean-Field Limits and Synchronization for the Stochastic Kuramoto Model [2], forthcoming in *Chaos*, authored by Marios A. Gkogkas, Benjamin Jüttner, Christian Kuehn, and Erik A. Martens,

Complex dynamics in adaptive phase oscillator networks [3], authored by Benjamin Jüttner and Erik A. Martens.

The articles are attached to the very end of this thesis with permission of *Chaos*.

This thesis consists of three Chapters. In Chapter 1, we give a (beginner-friendly) introduction to the field of coupled oscillators, explaining the Kuramoto model and its variants, as well as the Theta neuron model, briefly mentioning research conducted on these models by others. Also, we explain how to

make the transition from finite systems to systems of infinite size. Throughout Chapter 1 we introduce technical terms and mathematical symbols that will be used in a consistent manner in the entire thesis. In Chapter 2 we summarize each of the above listed articles. Finally, in Chapter 3, we compare the results of the three articles and discuss said results, proposing new research questions to follow up on this work.

The results of this thesis are, to the best of our knowledge, original. All statements, equations and ideas originating from other research are marked with references.

Lyngby, 14^{th} of September 2022

Benjamin Jüttner

Acknowledgements

I would like to thank my family, consisting of wonderful individuals without whom I would not be here to study oscillators. I thank my friends, who provided me with unforgettable conversations, heavy boardgaming, sports and other activities throughout this PhD. I express my gratitude to Erik Martens, who acted as my knowledgeable and reliable supervisor for three years, who inspired me to spend time on interesting topics, and who handled his PhD student with great patience. I am grateful to Christian Kuehn, who welcomed me at the Technical University of Munich, who hosted live meetings in which I learned much, and who quickly and precisely responded to all my questions via e-mail. I thank Marios, who took the time to explain to me many a difficult mathematical concept and converse with me about non-mathematical matters too. I am obliged to Sune Lehmann, who gave me emotional and moral support in a difficult phase of the PhD. Finally, I thank Poul Hjorth, who provided a stable frame for my PhD and who gave valuable feedback and hints regarding this thesis.

Notation

Mathematical symbols and technical terms are used consistently throughout the thesis. We made an effort to synchronize the notation of this thesis and the articles [1–3] as best as possible. The remaining mismatch will be handled by the neural adaptivity of the reader.

Mathematical symbols

$\mathbb{T}$	the unit circle, $\mathbb{R}$ mod 2π
ϕ	phase on the unit circle
$\hat{\phi}$	phase on the real line
l, m	oscillator indices
$\omega \sim g(\omega)$	intrinsic freqencies ω are drawn from the (probability) distribution $g(\omega)$
N	number of oscillators = system size
$[N]$	the index set $\{1, \ldots, N\}$
t	time
$\boldsymbol{u}, \boldsymbol{\phi}, \boldsymbol{B}$	vectors (bold face)
c^*	complex conjugate of c
i	the imaginary unit, $\mathrm{i}^2 = -1$
Ω	the vertex set
C	coupling strength (Kuramoto), $C \in \mathbb{R}$
$C^\natural$	critical coupling strength for the onset of partial coherence
$\boldsymbol{\kappa}$	coupling (graph) matrix (bold face), with elements $\kappa_{lm} \in \mathbb{R}$ (the coupling weights)
x, y	points in the vertex set $\Omega = [0, 1]$ for $N \to \infty$
K	coupling graphon, $K = K(x, y)$
A	coupling graphop
z	order parameter (complex number)
r	order parameter (magnitude)
ρ	(probability) density of oscillator mass, $N \to \infty$

All other mathematical symbols will be explained upon first occurrence.

Technical terms

All technical terms used in this thesis are written in *italic* face upon first usage. To make this thesis as easy to read as possible, we avoid using multiple terms for the same thing. Yet, we will often hint at alternative terms used in the literature but not adopted in this thesis. These terms are written in normal face and marked with "".

Abbreviations

OA Ott-Antonsen
ER Erdös-Rényi
ODE ordinary differential equation
SDE stochastic differential equation
PDE partial differential equation
SNIC Saddle-Node on an Invariant Cycle

Contents

Chapter 1

Introduction

This thesis is based on the articles [1–3]. The articles will be summarized and discussed in Chapters 2 and 3, respectively. As a support, we give this Introduction, providing a *concise* overview and a basic understanding of the mathematical concepts and equations typically encountered in the field of (adaptive) phase oscillator dynamics. At the same time, this Introduction sets up a common language with which to compare the articles [1–3].

1.1 Synchronization

1.1.1 A brief history of synchronization

Synchronization is the process in which two or more parts of a system start conforming to each other's behaviour. Synchronization occurs between the Earth and the Moon and between photons in a laser beam. Synchronization occurs between neurons in the reader, between different members of a social group and between engines and generators in a power grid. Synchronization is the reliable force behind many a thing that we take for granted in everyday life. Synchronization is an underlying mechanism of the cosmos that operates on a vast range of time scales and spatial scales. Synchronization is, as S. H. Strogatz puts it,

"perhaps the most pervasive drive in all of nature". Synchronization can be seen as a counter-force to the law of entropy. The former causes organization, the latter disorganization. Etymologically, synchronization comes from the ancient Greek "syn" (together) and "chronos" (time). In this sense, synchronization means that different agents time their behaviour such as to occur *at the same time*. As terms get used and abused with time, the term synchronization has also been extended to spatial contexts, here it means that different agents coordinate their behaviour to occur in the same place.

Synchronization was spotted by pioneers such as C. Huygens (1629 - 1695) who realized that pendulum clocks are able to synchronize [4]. One of the first to study synchronization mathematically was N. Wiener (1894 – 1964) who tried an approach with Fourier integrals [5] which has proven to be unfruitful. A. T. Winfree (1942 – 2002) later formulated synchronization as a large ensemble of limit cycle oscillators who are coupled to each other and are thus coupled to the overall rhythm generated by the entire ensemble [6]. His work attracted the attention of Y. Kuramoto, to whom we owe the elegant Kuramoto model on which much of the work of this thesis is based. Synchronization being an utterly universal phenomenon, the Kuramoto model provides a level of abstraction that makes it applicable to synchronization in a universal context. This viewpoint – which looks at synchronization in general rather than a specific real-world example such as e.g. the synchronization in electric circuits – shall be adopted in this thesis. S. H. Strogatz pushed our understanding of synchronization and the Kuramoto model further and in entertaining ways communicated the topic to a more general audience.[1] Researchers such as E. Ott, T. Antonsen, S. Watanabe, S. H. Strogatz, M. A. Gkogkas and C. Kuehn gave us powerful mathematical techniques that allow us to see the big picture in very large systems of synchronizable oscillators [8–12]. E. A. Martens has furthered our knowledge about special types of synchronization / non-synchronization patterns called chimera states, demonstrated not only in theoretical works as [13, 14], but also by an impressive real-world experiment with metronomes on coupled swings [15].

Synchronization between different parts of a system requires that these parts influence each other. Relations between pairs of parts of a system can be described via *graphs* (also called "networks"). Examples in real life are numerous: the brain and other nervous systems, electric circuits, the internet, Facebook, power grids, railroads, etc. The study of synchronization thus involves the study of dynamics *on* graphs. Indeed, the structure of the graph plays a crucial role and many studies have investigated how synchronization depends on the properties of the underlying graph [16]. In the real world, graphs are often subject to change as time goes by. New connections between nerve cells form when practicing the piano, members of social networks intensify relations to other members,

[1] Yet it was G. A. Gottwald who compared the Kuramoto model to a fruit fly [7].

form new relations or even "unfriend" people on Facebook. A relatively new angle in the study of synchronization is thus the dynamics *of* graphs, where the graph changes over time. We also speak of *adaptive* graphs (or "networks").

This thesis will address some questions in the directions alluded to earlier. We are interested in the dynamic behaviour of (abstract) systems of synchronizable oscillators, and in qualitative changes of this behaviour as parameters vary, these changes are called *bifurcations* (or sometimes "phase transitions"). The systems in question can consist of a small, medium, large or even infinite number of oscillators. The graphs can be constant in time or adaptive. If they are constant, we allow for different types of graphs. The central question is: how does synchronization depend on the graph structure or on the extent to which the graph is able to adapt? To be able to pose this question more specifically and to break it down into sub-questions, we will set up a language in the remainder of this Introduction.

1.1.2 Types of synchronization

In this thesis we consider a system of N phase oscillators with time-dependent phases $\phi_l(t) \in \mathbb{T}$, where $\mathbb{T} = \mathbb{R} \bmod 2\pi$ is the unit circle, and $l \in [N] := \{1, \ldots, N\}$ is the index of the oscillator. N is thus called the *system size*. The *dynamic frequency* $\frac{\mathrm{d}\phi_l}{\mathrm{d}t}$ is the instantaneous speed with which the oscillator's phase rotates around the unit circle. Note that the difference between two phases is taken mod 2π, like the individual phases. Depending on the relative position and (angular) velocity of N phase oscillators we can define various types of *synchronization*:

Definition 1 ***Weak synchronization.*** *A set of N phase oscillators is said to be weakly synchronized if there is a fixed upper bound smaller than 2π such that each pairwise phase difference stays below this bound at all times.*

Definition 2 ***Frequency-synchronization.*** *A set of N phase oscillators with phases $\phi_1, \ldots, \phi_N \in \mathbb{T}$ is said to be frequency-synchronized if all pairwise phase differences are constant in time, or equivalently, if $\frac{d\phi_1(t)}{dt} = \ldots = \frac{d\phi_N(t)}{dt} \ \forall t$.*

Definition 3 ***Phase-synchronization.*** *A set of N phase oscillators with phases $\phi_1, \ldots, \phi_N \in \mathbb{T}$ is said to be phase-synchronized if $\phi_1(t) = \ldots = \phi_N(t) \ \forall t$.*

Clearly, phase-synchronization implies frequency-synchronization implies weak synchronization.[2]

[2] in the literature, phase-synchronization and frequency-synchronization are often referred to as "phase-locking" and "frequency-locking", respectively.

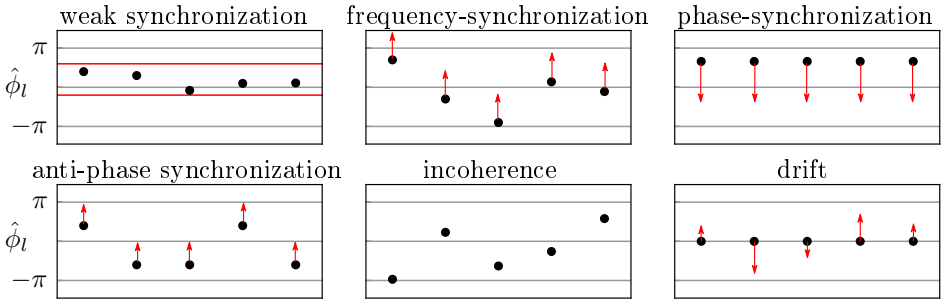

Figure 1.1: Illustration of Definitions 1 to 6. Black dots indicate phases $\hat{\phi}_l$ of oscillators, red arrows indicate constant dynamic frequencies. Absence of arrows indicates that the dynamic frequencies are not important for the definition. In the weakly synchronized panel, red lines indicate a range in which all phases stay at all times. The red lines may move over time, their distance stays constant.

Definition 4 ***Anti-phase-synchronization.*** *A pair of phase oscillators with phases $\phi_1, \phi_2 \in \mathbb{T}$ is said to be anti-phase-synchronized if $\phi_1(t) - \phi_2(t) = \pi \ \forall t$.*

Definition 5 ***Incoherence.*** *A set of N phase oscillators with phases $\phi_1, \ldots, \phi_N \in \mathbb{T}$ is said to be incoherent if the phases are spread (relatively) evenly across the unit circle.*

We intentionally kept the definition of incoherence a bit lax, so as to include states where the oscillators are spread only roughly evenly around the unit circle. This will prove useful when dealing with finite-size effects, see Sec. 1.4.1. A more strict subclass of incoherence is *equidistant phases*,[3] where $\phi_l = 2\pi l/N, \ l \in [N]$. Moreover, a set of many drifting oscillators (see Def. 6) can be incoherent.

So far we only consider the location of an oscillator on the unit circle, and are not concerned with how many times the oscillator has rotated around the unit circle in the past. This viewpoint will suffice for the most part. However, it is sometimes necessary to take the past into account, so we define a phase $\hat{\phi}(t) \in \mathbb{R}$. If an oscillator starts at the position 0.1π on the unit circle and rotates around the circle 3 times, then $\hat{\phi} = 6.1\pi$, while $\phi = 0.1\pi$.

Definition 6 ***Drift.*** *Two oscillators with phases $\hat{\phi}_1$ and $\hat{\phi}_2$ are said to drift (apart from or relative to each other) if $|\hat{\phi}_1 - \hat{\phi}_2| \to \infty$ as $t \to \infty$. A set of N oscillators drifts if at least two of its oscillators drift apart from each other.*

[3] called "splay state" by Berner et al. or "(travelling) waves" by some.

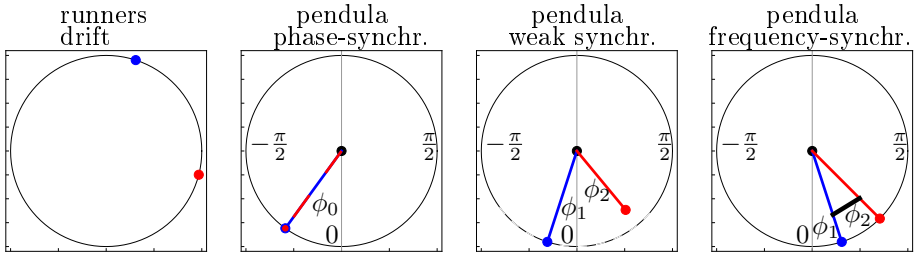

Figure 1.2: Illustration of drift and different types of synchronization. The runners run at different constant speeds and thus rotate, the pendula librate. In the phase-snychronized scenario, both pendula have identical period and initial condition and thus identical phase $\phi_0 := \phi_1 \equiv \phi_2$ at all times. In the weakly synchronized scenario, phases stay confined to the same (dashed) subset of the unit circle. Even if the lengths of the pendula and thus the pendulum frequencies were identical, the pendula would still only be weakly and not frequency-synchronized (assuming nonidentical initial conditions). In the frequency-synchronized case, both pendula are welded together with an iron rod (black).

Definitions 1 to 6 are illustrated in Fig. 1.1. Note that phases (but not the constant dynamical frequencies) are identical in the drifting panel of the Figure. This is to emphasize that despite being momentarily of equal phase, the oscillators are not phase-synchronized.

Imagine two runners on a circular lane. If one runner at all times runs at a larger speed than the other, they drift. The faster runner will alternate between "running away from the other" and "approaching the other from behind". Still, the distance $|\hat{\phi}_1 - \hat{\phi}_2|$ between the runners keeps increasing. In contrast, we will abuse two pendula (Fig. 1.2). The equilibrium position of a pendulum is identified with $\phi_l = 0$. The angle formed by the displaced position of a pendulum and the equilibrium position is identified with ϕ_l. Assume the pendula do not influence each other and never never cross $\phi_l = \pi$ or $\phi_l = -\pi$, so $\phi_l \equiv \hat{\phi}_l$. Clearly, if the two pendula have the same pendulum frequency (given by their length) and are started at the same position, they are phase-synchronized. Now if the two pendula have different pendulum frequencies, their phases ϕ_1, ϕ_2 are neither frequency-synchronized (because $\phi_1(t) - \phi_2(t)$ is not constant in time) nor drifting (because $\phi_1(t) - \phi_2(t)$ is bounded) but weakly synchronized (since the phases always remain in a fixed neighbourhood of each other). If the pendula have the same pendulum frequency but are started at different positions we – somewhat stubbornly, ignoring physics intutition, but faithful to our above definitions – insist that the pendula are not frequency-, but only weakly synchronized (because $\phi_1(t) - \phi_2(t)$ is not constant in time). As a compensation for

this narrow-mindedness, we weld the two pendula together with an iron rod and achieve frequency-synchronization. To complete our definitions, we say that a phase performs a *rotation* if it travels one entire round around the unit circle; in contrast, a phase performs a *libration* if it swings back and forth confined to a mere subset of the unit circle. Thus, in the runners' analogy, the phases perform a series of rotations while in the pendulum analogy the phases perform a series of librations.

Finally, a given set of oscillators might contain subsets which exhibit distinct types of weak / frequency-synchronization. These subsets are called *clusters*. For example, two clusters might be internally phase- or frequency-synchronized but rotate at different speeds, or one cluster is frequency-synchronized while the other is phase-synchronized etc. In such cases we speak of *cluster synchronization*.

1.1.3 Coherence and the order parameter

Systems of many oscillators are usually difficult to handle and interpret when looking at the individual phases, i.e., adopting a microscopic perspective. The question of *coherence* of the phases concerns whether oscillators are spread (roughly evenly) all over the unit circle or whether the phases are (relatively) close together. Here, a macroscopic perspective – which looks at the entirety of all oscillators rather than individual oscillators – is helpful. An elegant macroscopic quantity is the *order parameter*

$$z(t) \equiv r(t)\mathrm{e}^{\mathrm{i}\psi(t)} := \frac{1}{N}\sum_{l\in[N]} \mathrm{e}^{\mathrm{i}\phi_l(t)} \tag{1.1}$$

which is simply the average of the complex phasors obtained from the individual phases. Clearly, $r \in [0,1]$. ψ is a representative or "average" phase of the oscillators.[4] Clearly, ψ is meaningless for $r = 0$. For simplicity of wording, we will use the term *order parameter* to refer to both the complex number z and its magnitude r, and we will always make clear which one is meant.

The order parameter has certain benefits and limitations. First and foremost, the order parameter r offers a convenient way of quantifying how close the phases are together without calculating their pairwise differences. Thus, we can say that the *(level of) coherence* of the oscillators manifests itself in r. Incoherence (see Definition 5) implies $r \approx 0$. *Perfect coherence*, i.e., equality of all phases, is equivalent to $r = 1$. The intermediate regime between incoherence and perfect

[4] The term "average phase" is widely used in the literature and should *not* be interpreted as "arithmetic mean of the phases".

coherence is callled *partial coherence*. In this regime, we say the coherence is low (closer to incoherence) or high (closer to perfect coherence). Thus, partial coherence implies an intermediate value of r. Note that a value of r close or equal to zero might also be caused by states other than incoherence. Take four oscillators with $\phi_1 = \phi_2 = 0, \phi_3 = \phi_4 = \pi$, then $r = 0$. An uncountable number of such and similar non-incoherent states with $r = 0$ or $r \approx 0$ can be constructed. However, in the models studied in this thesis, such special configurations of the phases do not appear out of the blue, they require certain properties of the model in question. Therefore, when seeing an order parameter r close to zero, it is reasonable to expect incoherence. Moreover, the closer r gets to 1, the more it is true that the majority of oscillators have small pairwise phase differences. The order parameter has some relations to the types of synchronization and drift defiend in the previous Section. Like the phases, the order parameter is dynamic; the level of coherence, and thus $r(t)$, typically waxes and wanes over time, unless the oscillators are frequency-synchronized, in which case $r(t)$ =const. The oscillators are phase-synchronized iff. $r(t)$ =const.= 1 (phase-synchronization does not restrict $\psi(t)$). Drifting oscillators cause an order parameter $r(t)$ which stays close to zero at all times.[5] By Definition 1, weak synchronization implies partial coherence.

The technical terms learned in this Section by definition overlap to some extent but do not contradict each other, and hopefully make sense to the reader. Such a system of definitions is however not needed in every publication. Thus, the reader is warned that these technical terms are used in different ways in the literature.[6]

1.2 Graph theory

Having established an understanding of synchronization, we may ask how synchronization or a certain level of coherence come about. Oscillators might of course synchronize by accident, but in the context of this thesis, they move closer together in their phase or show some kind of synchronization because they influence each other. This influence between oscillators is called *coupling*. Which oscillator influences what other oscillator how strongly is described by a *graph*. We will here introduce the terms from the mathematical field of graph theory that are needed for this thesis. The definitions can be found in standard

[5] As $N \to \infty$, $z(t), r(t)$ will stay closer and closer to zero when oscillators drift. This finite-size effect will become clearer in Secs. 1.4.1 and 1.6.2.

[6] For example, Berner et al. refer to what we call a *frequency-synchronized* state as a "phase-locked" state. *(Partial) coherence* is often referred to as "(partial) synchrony" or "(partial) synchronization".

textbooks, e.g. [17].

Definition 7 ***Graph.*** *A graph is a structure with N vertices. Each pair of vertices l, m are either neighbours, via an edge, or not. $\Omega \equiv [N]$ is called the vertex set and $\mathcal{E} \subseteq \Omega \times \Omega$ is called the edge set of the graph. Iff. l and m are neighbours, $(l, m) \in \mathcal{E}$.*

In our context, there is a one-to-one correspondence between an oscillator and a vertex in the graph. The graph determines exactly how the oscillators are coupled. We will in this thesis only use the term *(coupling) graph*, while other authors in the field of coupled oscillators often use the terms (coupling) "network" or (coupling) "topology".

Definition 8 ***Weighted edge.*** *An edge is called weighted if it has a real number attached to it, the weight of the edge. An edge with weight 0 is considered non-existent, an edge with weight 1 is considered unweighted.*

Definition 9 ***Weighted graph.*** *A graph is called weighted if it contains a weighted edge, otherwise the graph is called unweighted.*

Definition 10 ***Directed edge.*** *An edge (l, m) is called directed if is interpreted to start at vertex l and end at vertex m. If l and m are not interpreted as start- or end- vertex of the edge (l, m), then (l, m) is called undirected.*

Note: For the purposes of this thesis, an undirected edge can be viewed as bidirectional. In fact, if both (l, m) and (m, l) exist as directed edges in the same graph (and have the same weight w if the graph is weighted), then they can be (thought of as) deleted and replaced by an undirected edge (l, m) (with weight w).

Definition 11 ***Directed graph.*** *A graph is called directed if it contains a directed edge, otherwise the graph is called undirected.*

Definition 12 ***Self-loop.*** *A self-loop is a (weighted or unweighted) undirected edge between a vertex and itself.*

Definition 13 ***(Weighted) adjacency matrix.*** *Every graph with N vertices can be represented by a (weighted) adjacency matrix $\boldsymbol{\kappa} \in \mathbb{R}^{N \times N}$ with κ_{lm} being the weight of the edge (m, l) (from m to l), for all $l, m \in [N]$. A graph is unweighted iff. all entries of $\boldsymbol{\kappa}$ are either 0 or 1. In this case $\boldsymbol{\kappa}$ is simply called adjacency matrix. A graph is undirected iff. $\boldsymbol{\kappa}$ is symmetric. (Weighted) self-loops are represented by the non-zero diagonal elements of $\boldsymbol{\kappa}$.*

Note: For simplicity of wording, we will refer to both a graph and its ((weighted) adjacency) matrix by $\boldsymbol{\kappa}$.

Definition 14 ***Degree.*** *In an unweighted undirected graph, the degree of a vertex is the number of its neighbours. A regular graph is a graph in which every vertex has the same degree.*

In an unweighted undirected graph, the *neighbourhood* of a vertex l is the set of neighbours of l. For weighted graphs we generalize the notion as follows:

Definition 15 ***Neighbourhood.*** *In a weighted undirected graph, the neighbourhood of l is the lth column (or row) of $\boldsymbol{\kappa}$.*

Note: the notions of degree and neighbourhood can be extended to directed graphs, but this is not needed in this thesis.

Definition 16 ***Connected.*** *In an undirected graph, two vertices are connected if one can be reached from the other by a path of undirected edges.*

Note the difference between *neighbouring* and *connected* (the former implies the latter).

Definition 17 ***Connected graph.*** *An undirected graph is called connected if every vertex is connected to every other vertex.*

Definition 18 ***Complete graph.*** *The undirected, unweighted graph where every vertex is a neighbour of every other vertex is called the complete graph.*

Note: we (and many other authors) will also refer to the complete graph as *all-to-all coupling*.

Definition 19 ***Complete bipartite graph.*** *A complete bipartite graph is an undirected, unweighted graph whose vertex set Ω can be subdivided into two groups such that for all $l, m \in \Omega$ we have $(l, m) \in \mathcal{E}$ iff. l and m belong to distinct groups.*

1.3 Dynamical systems

In this thesis, the models governing how oscillators influence each other are *dynamical systems*, i.e., systems of ordinary (ODE) or stochastic (SDE) differ-

ential equations. We will therefore here give a very brief overview of the field of dynamical systems, simplifying the definitions to avoid details not needed in this thesis. The interested reader is referred to [18–20].

Definition 20 ***Dynamical system.*** *A dynamical system is a system of differential equations governing the temporal evolution of state variables* $\boldsymbol{u}$*. These systems can be written as* $\frac{d\boldsymbol{u}}{dt} = \boldsymbol{f}(\boldsymbol{u})$ *(for systems of ODEs) or* $d\boldsymbol{u} = d\boldsymbol{f}(\boldsymbol{u}) + d\boldsymbol{R}$ *(for systems of SDEs) where* $d\boldsymbol{R}$ *is a noise term.*

Definition 21 ***Trajectory.*** *A trajectory / solution* $\boldsymbol{u}(t)$ *to a dynamical system is the temporal evolution of the state variables that is uniquely defined by the dynamical system itself and an initial condition* $\boldsymbol{u}(0)$*.*

Note: In this thesis, trajectories / solutions are found by numerically *solving* (or "integrating") the dynamical system in question.

Definition 22 ***(Stable) equilibrium.*** *A state* $\boldsymbol{u}^*$ *of a dynamical system is called an equilibrium if the temporal change of the state variables,* $\frac{d\boldsymbol{u}}{dt}$*, vanishes when the system assumes the state* $\boldsymbol{u}^*$*. The equilibrium is called stable if each trajectory* $\boldsymbol{u}(t)$ *whose initial condition* $\boldsymbol{u}(0)$ *lies in a certain fixed neighbourhood of* $\boldsymbol{u}^*$ *asymptotically approaches* $\boldsymbol{u}^*$ *as* $t \to \infty$*.*

Definition 23 ***Stable limit cycle.*** *A closed trajectory* $\boldsymbol{u}_{LC}$ *is called a stable limit cycle if, for some fixed period* $T < \infty$*, any choice of initial condition* $\boldsymbol{u}(0) \in \boldsymbol{u}_{LC}$ *implies* $\boldsymbol{u}(T) = \boldsymbol{u}(0)$*,* $\boldsymbol{u}(t) \in \boldsymbol{u}_{LC}$ $\forall t$ *and each trajectory whose initial condition* $\boldsymbol{u}(0)$ *lies in a certain fixed neighbourhood of* $\boldsymbol{u}_{LC}$ *asymptotically approaches* $\boldsymbol{u}_{LC}$ *as* $t \to \infty$*.*

Definition 24 ***Bifurcation.*** *A bifurcation is a qualitative change in the dynamical behaviour of a dynamical system as a parameter passes through a critical value.*

Note: Bifurcations seen in this thesis can bring about the creation and destruction of equilibria and oscillatory states (such as limit cycles or chaos). Bifurcations can also change the stabilities of states.

1.4 The Kuramoto model

Having established what synchronization is and how it is mediated via graphs, we introduce a widely used dynamical system that enables synchronization via different graphs, classically the complete graph (Sec. 1.4.1).

1.4.1 The classical Kuramoto model

The Kuramoto model [21] is an intuitive and generic model to describe synchronization phenomena. It is stated in its classical form as a system of ODEs

$$\frac{\mathrm{d}\phi_l}{\mathrm{d}t} = \omega_l + \frac{C}{N}\sum_{m=1}^{N}\sin(\phi_m - \phi_l), \quad l \in [N]. \tag{1.2}$$

The ω_l are called *intrinsic frequencies* of the oscillators, C is called *coupling strength*. In this context, sin is called the *coupling function*. Notice the phase-shift invariance of the system:

$$(\phi_1, \ldots, \phi_N) \mapsto (\phi_1, \ldots, \phi_N) + \phi_0 + \omega_0 t, \quad \phi_0 \in \mathbb{T}, \omega_0 \in \mathbb{R} \tag{1.3a}$$

$$(\omega_1, \ldots, \omega_N) \mapsto (\omega_1, \ldots, \omega_N) + \omega_0, \quad \omega_0 \in \mathbb{R} \tag{1.3b}$$

where (1.3b) is a direct consequence of (1.3a). In other words, the behaviour of (1.2) does not change if we add an identical constant ϕ_0 (ω_0) to all phases (intrinsic frequencies). It means that we can wlog. make one of the oscillators the reference frame and set this oscillator's phase constantly to zero. For simplicity, we shall in this thesis always assume that the mean of all ω_l's is zero, which can be achieved using (1.3b). If the ω_l's are all equal (i.e., they are all 0 wlog., using (1.3b)), then we speak of *identical oscillators*. Unless specified otherwise, we will in this thesis assume the ω_l's to follow an even, unimodal distribution $g(\omega)$ (i.e., $g(\omega) = g(-\omega)$ and $g(\omega)$ having its global maximum at $\omega = 0$). Commonly used examples for $g(\omega)$ are the normal distribution or the Lorentzian/Cauchy distribution.

The temporal evolution of the phase $\phi_l(t)$ of the lth oscillator is always a compromise between two competing forces: the first term, ω_l, is the speed at which the oscillator naturally prefers to rotate around the unit circle. The second term, the coupling term, proportional to the coupling strength $C \in \mathbb{R}$, either slows down or speeds up the oscillator l, depending on where its phase stands relative to the other oscillators. The relation between C and (the spread / standard deviation of) the ω_l's thus determines which of the competing forces dominates.

For identical oscillators and $C > 0$, the phases ϕ_l always converge to the phase-synchronized state as $t \to \infty$. For non-identical oscillators, the system's behaviour is more involved. We shall here informally introduce a concept vital to the Kuramoto model, namely the *coherence transition*, i.e., the transition from incoherence over partial coherence to perfect coherence and phase-synchronization, which will be formalized more rigorously in Sec. 1.6.2. The Kuramoto model has a critical coupling strength $C^\natural$ such that for $C < C^\natural$, the oscillators drift (and are incoherent). That means, in a solution to (1.2), the order parameter $z(t)$ will fluctuate around 0. These $\mathcal{O}(N^{-1/2})$ fluctuations are

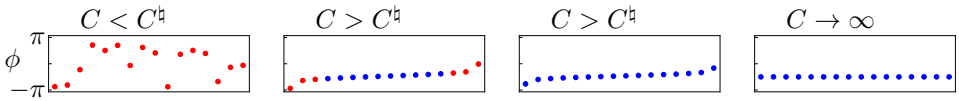

Figure 1.3: Qualitative coherence transition of the Kuramoto model (1.2) with normally distributed intrinsic frequencies. C increases from left to right. Red dots mark drifting oscillators with nonzero, distinct dynamical frequencies, blue dots mark frequency-synchronized oscillators with zero dynamical frequency.

a *finite-size effect*. If $C > C^\natural$, then the oscillators split into two populations. The oscillators of one population are weakly synchronized to each other. The oscillators of the other population drift apart from each other and from the weakly synchronized population. The weakly synchronized population is partially coherent, so its contribution to r is larger than zero. Clearly, the order parameter r still fluctuates. As C is increased above $C^\natural$, the first oscillators leave the drifting population in favour of the weakly synchronized population. Also, the weakly synchronized oscillators draw closer together. This causes the fluctuations to decrease and the temporal mean of r to increase. For C sufficiently large, the drifting population is empty, i.e. *all* oscillators are weakly synchronized. As $C \to \infty$, the oscillators move towards the phase-synchronized state. This transition is illustrated qualitatively in Fig. 1.3. There, weakly synchronized oscillators are even frequency-synchronized. Notice that due to (1.3) we can substract the frequency-synchronized oscillators' dynamical frequency $\frac{\mathrm{d}\phi^*(t)}{\mathrm{d}t}$ from *all* oscillators' dynamical frequencies $\frac{\mathrm{d}\phi_l(t)}{\mathrm{d}t}$, so that the frequency-synchronized oscillators stand still on the unit circle.

As we have just seen, the devil is in the detail already in this simple model. For example, it is counterintuitive that the model does not start to pull the oscillators together as soon as $C > 0$, but instead $C > C^\natural$ is required to see partial coherence. Somewhat suprisingly, the analysis of (1.2) can be put on more solid ground when $N \to \infty$, as we shall see in Sec. 1.6.2. For now, the following basic intutition will suffice. In (1.2), we have many "tame" oscillators with intrinsic frequencies ω_l close to 0, and few "wild" oscillators whose ω's are far from zero. The tame oscillators are the first to weakly synchronize when $C > C^\natural$. The higher C gets, the more of the oscillators weakly synchronize and the closer they draw together. The wildest oscillators need the highest value of C in order the join the synchronized herd.

1.4.2 The Kuramoto-Sakaguchi model

The Kuramoto-Sakaguchi model [22] is given by

$$\frac{\mathrm{d}\phi_l}{\mathrm{d}t} = \omega_l + \frac{C}{N}\sum_{m=1}^{N}\sin(\phi_m - \phi_l + \alpha), \quad |\alpha| \leq \frac{\pi}{4}, \ \ l \in [N]. \tag{1.4}$$

The coupling function is thus a shifted sine, sometimes this shift is used to model signaling delays in real-world systems of oscillators. The *Sakaguchi phase lag* α complicates the coherence transition too: for certain values of $\alpha \neq 0$ and in some intermediate range of $C > C^\natural$, the stable partially coherent state either coexists with or disappears in favour of the stable incoherent state [23, 24].

1.4.3 The Kuramoto model on general coupling graphs

The models (1.2) and (1.4) are based on the assumption that every oscillator influences every other oscillator with the same coupling strength C. The coupling graph is thus the complete graph.[7] However, real-world graphs are often more complicated and less regular. The Kuramoto model on general coupling graphs, defined via a matrix $\boldsymbol{\kappa}$ with entries κ_{lm}, reads

$$\frac{\mathrm{d}\phi_l}{\mathrm{d}t} = \omega_l + \frac{C}{N}\sum_{m=1}^{N}\kappa_{lm}\sin(\phi_m - \phi_l), \quad l \in [N]. \tag{1.5}$$

The coupling weight κ_{lm} is the weight with which oscillator m couples into the dynamics of oscillator l. We see that (1.3) still holds. Moreover, possible self-couplings κ_{ll} have no effect.[8] For any kind of synchronization among *all* oscillators to happen, the graph needs to be connected.

Some coupling graphs are often considered in the literature. First of all, there is the regular ring lattice graph. Here, all vertices can be imagined as arranged in a ring, and each vertex has an edge to its $k \leq N/2$ nearest neighbours to the right and to the left, respectively; this is often called "local coupling". To break this symmetry where every vertex has the same degree, and to introduce "shortcuts" in the graph, the *small-world graph* was invented [25]. Here, every edge of the regular ring lattice graph is, with a probability p_{SW}, replaced by a random edge between *any* two vertices, never allowing duplicate edges. This graph has the "small-world" property, meaning that the path length between any two vertices

[7] this is often called "global coupling" (or, more precisely, "global and identical coupling").

[8] Even if a Sakaguchi phase lag is introduced, the diagonal of $\boldsymbol{\kappa}$ can be set to zero if the ω_l's are adjusted accordingly.

is small on average due to the randomly rewired edges that act as shortcuts even if the two vertices in question are far away on the ring. In the extreme case $p_{\mathrm{SW}} = 1$, the small-world graph is equivalent to the Erdös-Rényi (ER) graph, a graph where every edge of the all-to-all graph exists with a probability p_{ER}. A figure illustrating these three graphs nicely is found in [25](Fig.1).

With such graphs, the behaviour of the model (1.5) deviates from the classical Kuramoto model (1.2) in interesting ways. Firstly, in the regular ring lattice graph, for $k \lesssim 0.34N$, the partially coherent state is not the only attractor, it coexists with stable states called "twisted waves" in [26]. Secondly, the small-world graph has a lower $C^{\natural}$ than the regular ring lattice graph [27](Fig.1).

Another random graph with the small-world property, i.e., small average path length, is the scale-free graph [28]. Such a graph can be constructed by starting with a tiny graph and repeatedly adding vertices and random edges from the new vertices to the existing ones, such that edges are preferably created to vertices that have many neighbours already. In this procedure, we obtain very few *hubs*, i.e., vertices with a huge number of neighbours, while the vast majority of vertices have very low degree. The probability of any vertex to have degree k is proportional to $k^{-\gamma}$ with γ positive. The hubs "keep the graph together" and provide the short average path length. This graph reflects many graphs in the real world (where often $2 < \gamma < 3$), e.g. the internet, with hubs such as Google. The Kuramoto model on scale-free graphs was studied, e.g., in [29, 30]. Importantly, it was found that, in the limit $N \to \infty$, $C^{\natural} = 0$ ($C^{\natural} > 0$) for $2 < \gamma \leq 3$ ($\gamma > 3$) [31].

The Kuramoto model (1.5) has been studied for other graphs too, e.g. the complete bipartite graph [32] and random graphs with various clustering properties [33–38]. Even though interesting behaviour is brought about by non-all-to-all graphs, telling apart the effects of the *individual properties* of a given graph is no easy task [16](p.22).

Finally, it must be mentioned that the values of the ω_l's relative to each other, or the distribution(s) from which these values are drawn, play an important role in the behaviour of the system. The Kuramoto models (1.2) and (1.5) are typically considered for unimodal $g(\omega)$ like the normal or the Lorentzian/Cauchy distribution, or identical oscillators (Dirac delta distribution). Yet, multimodal distributions are worth studying too. For bimodal $g(\omega)$ in the classical Kuramoto model (1.2) the incoherent state can coexist with the partially coherent state [39](Fig. 1b). In [40–44], the oscillators in the model (1.5) were grouped into n populations where each coupling weight κ_{lm} assumes one of n^2 values depending only on which population(s) the oscillators l and m belong to. In some of these works, (population-dependent) Sakaguchi phase lags are added. The oscillators' natural frequencies ω_l are then drawn from distributions that

are individual for each population, e.g. $g(\omega)$ has a different mean for each population or ω_l is identical within populations but distinct across populations (like in [41, 45]). In [45], less regular graphs were allowed and cluster snychronization was studied.

1.4.4 The stochastic Kuramoto model

The stochastic Kuramoto model is given by a system of SDEs

$$\mathrm{d}\phi_l = \mathrm{d}t\left(\omega_l + \frac{C}{N}\sum_{m=1}^{N}\kappa_{lm}\sin(\phi_m - \phi_l + \alpha)\right) + \mathrm{d}R_l, \quad l \in [N] \tag{1.6}$$

where $\mathrm{d}R_l$ is the lth oscillator's *own* realization of some additive noise process common to *all* oscillators. In this thesis we will study a system with $\mathrm{d}R_l = \sigma_B \mathrm{d}B_l$ where each oscillator l has its own realization of Brownian motion, B_l. Brownian motion is, roughly speaking, integrated Gaussian white noise with zero mean and variance σ_B^2, see [46, 47] for an introduction to SDEs. An early work on the stochastic Kuramoto model was done by H. Sakaguchi himself and resulted in an expression for $C^\natural$ that depends on the distribution of the intrinsic frequencies and the variance of the noise [48]. In [49], the influence of the type of noise on the coherence transition in the all-to-all stochastic Kuramoto model was studied, arguing that real-world noise can often not be assumed Gaussian. In [50], the coherence transition of the stochastic Kuramoto model with identical oscillators was studied in the $N \to \infty$ limit and compared with numerical simulations of finite N. The article also briefly discusses how this could extend to more general graphs than the complete graph. In Sec. 2.2, we will adress the same question, but with a far more general graph given by a graphop limit.

1.4.5 The adaptive Kuramoto model

So far we have assumed the coupling graph $\boldsymbol{\kappa}$ to be constant. However, in real-world settings, coupling graphs often change over time, edges can be destroyed or created or change their weight. An adaptive Kuramoto model can be stated in many ways, we here give a formulation inspired by [51],

$$\frac{\mathrm{d}\phi_l}{\mathrm{d}t} = \omega_l + \frac{C}{N}\sum_{m=1}^{N}\kappa_{lm}\sin(\phi_m - \phi_l + \alpha), \quad l \in [N] \tag{1.7a}$$

$$\frac{\mathrm{d}\kappa_{lm}}{\mathrm{d}t} = \varepsilon[f(\phi_l - \phi_m) - \kappa_{lm}], \tag{1.7b}$$

with f bounded and $\varepsilon > 0$. The second term in (1.7b) prevents divergence of the coupling weights. It is often assumed that $0 < \varepsilon \ll 1$, this seperates the time scales of the phase dynamics vs. the adaptation dynamics, since in real-world settings the graph often changes more slowly than the states of the vertices. In [52–55], oscillators are identical and f is a sinusoidal function. A rich variety of cluster synchronization and other phenomena is reported. [56] provides a master stability function to determine synchronization in systems of the form (1.7) and more general systems, assuming that oscillators are identical. The case of non-identical oscillators is mathematically less tractable, and we shall address this case in Sec. 2.3, mainly for $N = 2$ and briefly for $N = 50$.

The field of adaptively coupled oscillators is an emerging field[9] and not limited to Kuramoto oscillators or even systems of ODEs, see [57, 58] for a review. In [59], the creation and deletion of edges of the unweighted coupling graph in the Kuramoto model was implemented via a time-discrete update rule that favours edges between nearly-phase-synchronized pairs of oscillators. It is found that the strongest amount of rewiring occurs at *intermediate* values of C. Also, the stationary graph reached by this model has small-world properties.

1.5 The Theta neuron

The Theta neuron (first derived in [60]) is a generic model for a so-called "class-I excitable oscillator" [61]. Entertaining this neurobiological analogy, a Theta neuron can be provoked to send a spike when receiving an input current I. The Theta neuron is governed by the ODE

$$\frac{\mathrm{d}\phi}{\mathrm{d}t} = 1 - \cos\phi + (1 + \cos\phi)I. \tag{1.8}$$

It is easy to check that for $I < 0$ there exist a stable and an unstable equilibrium on the unit circle, which coalesce at $I = 0$ and are absent for $I > 0$, i.e., a *Saddle-Node on an Invariant Cycle* (SNIC) bifurcation occurs at $I = 0$. In the abscence of equilibria, the neuron's phase rotates around the unit circle repeatedly, and every time it reaches $\phi = \pi$ we say that the neuron *spikes* or *fires*. When the equilibria exist and thus keep the neuron's phase from rotating forever, we say that the neuron is *quiescent*. While this one-dimensional model is already non-trivial due to its bifurcation (unlike the Kuramoto model, which is meaningless with $N = 1$), one can couple N Theta neurons in a system of ODEs:

$$\frac{\mathrm{d}\phi_l}{\mathrm{d}t} = 1 - \cos\phi_l + (1 + \cos\phi_l)[\eta_l + I_l(\boldsymbol{\kappa}, \boldsymbol{\phi})], \quad l \in [N] \tag{1.9}$$

[9] this area of research is also referred to as "adaptive networks", "co-evolutionary networks", "temporal networks", etc.

where η_l is an individual bias of the lth neuron towards spiking ($\eta_l > 0$) or quiescence ($\eta_l < 0$), and I_l is a coupling term (still called *input current* to underline the neuronal analogy) depending on the graph and the phases. There are several possibilities of designing the input current I_l such that it models how the spikes of other neurons influence the neuron l in its own spiking activity. In [62], the pulse function P models the amount of excitatory output that a neuron generates, depending on how close the neuron's phase ϕ is to the spiking state $\phi = \pi$:

$$P(\phi) = \frac{1}{2}(1 - \cos\phi). \tag{1.10}$$

The input current to the lth neuron is then simply

$$I_l(\boldsymbol{\kappa}, \boldsymbol{\phi}) = \frac{1}{N} \sum_{m \in [N]} \kappa_{lm} P(\phi_m). \tag{1.11}$$

Finally, the η's can be drawn from a distribution; in [62] the Lorentzian/Cauchy distribution is chosen:

$$g(\eta) = \frac{\Delta_\eta}{\pi[(\eta - \hat{\eta})^2 + \Delta_\eta^2]}. \tag{1.12}$$

The studies [62–64] take the system to the $N \to \infty$ limit and study it macroscopically (see Sec. 1.6.3), and we shall follow them in this approach. In [62], $\boldsymbol{\kappa}$ is taken as the complete graph and a comprehensive bifurcation analysis is carried out. The article reports macroscopic spiral and node equilibria, as well as macroscopic limit cycles, with different levels of coherence and spiking activity. In [63], an external time-dependent forcing is added. In [64], the graph is subdivided into two populations where one population influences the other unidirectionally. In the latter two articles, more complicated states such as macroscopic periodic, quasiperiodic and chaotic states are observed.

In Sec. 2.1 we adopt the idea of [64] and again split the neurons into two populations (of equal size), which roughly model two brain regions. However, we assume that populations influence each other with the same strength and that coupling is stronger within a population than across populations, so the matrix $\boldsymbol{\kappa}$ simplifies to

$$\kappa_{lm} := \begin{cases} \kappa & l, m \text{ belong to the same population} \\ a\kappa & l, m \text{ belong to different populations} \end{cases} \tag{1.13}$$

where $|\kappa| \geq |a\kappa|$. In the jargon of graph theory, the coupling of a population to itself is given by a complete graph (with weights κ), while the coupling between populations is given by a complete bipartite graph (with weights $a\kappa$).

1.6 Taking the limit $N \to \infty$

Coupled oscillator systems with large N are hard to analyze both analytically and numerically since the systems of ODEs have $\mathcal{O}(N)$ state variables; if the graph is adaptive, the number of state variables is even $\mathcal{O}(N^2)$. Yet, most research questions regarding coupled oscillator systems are only meaningful if N is large. Thankfully, taking the limit $N \to \infty$ often simplifies (or enables) the analytical treatment of the system from a *macroscopic* viewpoint. In this viewpoint, all *microscopic* information (i.e., the dynamical behaviour of the individual oscillators) is sacrificed, instead statistical information (e.g. the order parameter) regarding the behaviour of the entirety of oscillators is accessed. Letting go of microscopic information naturally makes it much harder to identify any types of synchronization as of Definitions 1-4.

1.6.1 Treating inifinitely many oscillators with probability densities

If the system at hand employs inifinitely many oscillators, one can no longer speak of an individual, labelled oscillator (or vertex). Instead, we deal with a *mass* of oscillators that is more dense in some places than in others. The mass can move around over time, become more dense in some places and thin out in others, yet the total mass stays constant all the time ("conservation of oscillators").[10] This notion is formalized by a joint probability density function, or simply *(probability) density*, describing some distribution. Indeed, $\rho(t, \phi, \omega)$ is the joint probability density of oscillators with intrinsic frequency ω that assume the phase ϕ at time t. The integral $\int_{\phi_a}^{\phi_b} \int_{\omega_a}^{\omega_b} \rho(t, \phi, \omega) \mathrm{d}\omega \mathrm{d}\phi$ quantifies, at time t, the probability of an oscillator to have an intrinsic frequency in the range $\omega_a \leq \omega \leq \omega_b$ and a phase in the range $\phi_a \leq \phi \leq \phi_b$ [9]. As a consequence,

$$\int_{\mathbb{T}} \int_{\mathbb{R}} \rho(t, \phi, \omega) \mathrm{d}\omega \mathrm{d}\phi = 1 \quad \forall t. \tag{1.14}$$

Moreover, there is $g(\omega)$, the prior probability density of the intrinsic frequencies of the oscillators (e.g., given by the normal or Lorentzian/Cauchy distribution). $g(\omega)$ is time-independent: the intrinsic frequencies of the individual oscillators, as well as the total amount of oscillators, are constant in time in the $N < \infty$ setting; intuitively, this continues to be the case in the $N \to \infty$ setting. $g(\omega)$

[10] The limit $N \to \infty$ is also called "continuum limit" (as the set $[N]$ is replaced by a continuum of oscillators), "thermodynamic limit" (imagining the oscillators as molecules in a gas, moving around due to their temperature being above 0K, so numerous that they can only be treated with macroscopic equations) or "mean-field limit".

can also be understood as a marginal distribution [8, 9]

$$g(\omega) = \int_{\mathbb{T}} \rho(t, \phi, \omega) \mathrm{d}\phi \quad \forall t. \tag{1.15}$$

Like any joint distribution, $\rho(t, \phi, \omega)$ can be separated into the prior distribution $g(\omega)$ and the conditional distribution[11] $\rho(t, \phi|\omega)$:

$$\rho(t, \phi, \omega) \equiv \rho(t, \phi|\omega) g(\omega). \tag{1.16}$$

Consequently [65], and as is the case for any conditional distribution,

$$\int_{\mathbb{T}} \rho(t, \phi|\omega) \mathrm{d}\phi = 1 \quad \forall \omega, t. \tag{1.17}$$

At time t, the integral $\int_{\phi_a}^{\phi_b} \rho(t, \phi|\omega) \mathrm{d}\phi$ quantifies the conditional probability of an oscillator to have a phase $\phi_a \leq \phi \leq \phi_b$ *given* that this oscillator has the intrinsic frequency ω.

$\rho(t, \phi, \omega)$ tells us how, at time t, the oscillator mass is spread over the ϕ, ω cylinder. Interested in the *dynamics* of coupled oscillators, we also want to know how the oscillator mass *moves*, i.e., how $\rho(t, \phi, \omega)$ changes with t. The temporal evolution of the oscillator mass is governed by a continuity/transport equation [66]

$$0 = \frac{\partial \rho(t, \phi, \omega)}{\partial t} + \frac{\partial [\rho(t, \phi, \omega) v(t, \phi, \omega)]}{\partial \phi}. \tag{1.18}$$

Note carefully that ρ is the solution to this partial differential equation (PDE) and v is (in this PDE) an independent external forcing. In fact, $v(t, \phi, \omega)$ describes how the portion of the oscillator mass that has intrinsic frequency ω and that at time t has the phase ϕ is *driven* by the phase dynamics, v is thus called a *characteristic field*. Note that the PDE (1.18) does not change $\rho(t, \phi, \omega)$ in ω direction, in keeping with the underlying assumption that the oscillators' intrinsic frequencies (and thus their density $g(\omega)$) are constant in time. Thus, (1.18) governs the phase evolution of "the oscillators", just as the set of ODEs $\frac{\mathrm{d}\boldsymbol{\phi}}{\mathrm{d}t} = \boldsymbol{f}(\boldsymbol{\phi})$ does in the $N < \infty$ case. Intuitively, (1.18) states the conservation of oscillators: for each ω and each t, the temporal increase of the density ρ at a certain point ϕ on the unit circle (first term) has to cancel out with the outflux ρv of oscillator mass from ϕ into the neighbouring point $\phi + \mathrm{d}\phi$ (second term). The total oscillator mass thus remains constant at all times.

[11] Most authors do not use the term "conditional distribution" explicitly, even though it is implied in their equations, and they also do not use the symbol "|", but use a comma instead. Since we deal with both joint and conditional distributions in this thesis and need to distiguish between these, we decided to adopt the "|" notation, which is standard in statistics.

Finally, we can once more define the order parameter z, which is still just an average of complex numbers $\mathrm{e}^{\mathrm{i}\phi}$:

$$z(t) \equiv r(t)\mathrm{e}^{\mathrm{i}\psi(t)} := \int_{\mathbb{T}}\int_{\mathbb{R}} \rho(t,\phi,\omega)\mathrm{e}^{\mathrm{i}\phi}\mathrm{d}\omega\mathrm{d}\phi = \int_{\mathbb{T}}\int_{\mathbb{R}} \rho(t,\phi|\omega)g(\omega)\mathrm{e}^{\mathrm{i}\phi}\mathrm{d}\omega\mathrm{d}\phi. \tag{1.19}$$

Another advantage of the $N \to \infty$ limit is that finite-size effects vanish, so we can tighten the definition of incoherence. In the $N \to \infty$ setting, the oscillators are incoherent at time t iff. their phases are uniformly distributed around the unit circle, i.e., $\rho(t,\phi|\omega) = 1/(2\pi)$ for all ω. The order parameter is then exactly zero.

With this, we have established the language that allows us to speak of the oscillator phase dynamics in the $N \to \infty$ setting. We can now go even further. Firstly, we can describe not only deterministic dynamical systems (as above), but also stochastic ones. If we add Gaussian white noise with variance σ_B^2 to the phase dynamics (like in (1.6)), we have to add a diffusion term to (1.18) so that the dynamics of the oscillator mass is now governed by the Fokker-Planck equation

$$0 = \frac{\partial\rho(t,\phi,\omega)}{\partial t} + \frac{\partial[\rho(t,\phi,\omega)v(t,\phi,\omega)]}{\partial\phi} + \frac{\sigma_B^2}{2}\cdot\frac{\partial^2\rho(t,\phi,\omega)}{\partial\phi^2}. \tag{1.20}$$

Importantly, v is only the *deterministic* driving force of the oscillator mass. The diffusion term describes the *stochastic* influence that the oscillator mass experiences. As an illustrative example, assume $v \equiv 0$, then (1.20) is simply the heat equation [67] and

$$\lim_{t\to\infty} \rho(t,\phi,\omega) = g(\omega), \tag{1.21a}$$

$$\lim_{t\to\infty} \rho(t,\phi|\omega) = \frac{1}{2\pi}\ \forall\omega, \tag{1.21b}$$

regardless of the initial condition $\rho(0,\phi,\omega)$. In other words, the oscillator mass always spreads out evenly on the unit cicle. This illustrates how, with time, the stochasticity destroys all phase information, even for special initial conditions where each oscillator's phase is known *exactly* in the beginning.[12] As can be expected, if v describes a (sufficiently strong) coupling between oscillators, this counteracts the stochasticity, causing the system to reach a partially coherent state rather than the incoherent state (1.21).

Secondly, we can can work with non-all-to-all coupling graphs. We then deal with joint probability densities $\rho(t,\phi,x,\omega)$ where x is an element of a vertex set

[12] this can be achieved by choosing a family of Dirac delta distributions as initial condition, $\rho(0,\phi,\omega) = g(\omega)\delta[\phi(\omega)]$.

Ω. Models using this form of ρ are found in [11, 12, 68][13] and Sec. 2.2. Having ρ depend on ω *and* x might seem odd. After all, in the $N < \infty$ setting, each vertex (= oscillator) has exactly one intrinsic frequency and exactly one phase at each time. However, phase and intrinsic frequency of "a vertex" are typically not known exactly in the $N \to \infty$ setting. Here, for each location x in the vertex set, $\rho(t, \phi, x, \omega)$ describes the probability density of "this vertex" having the intrinsic frequency ω and phase ϕ at time t. Frequency and phase of "a vertex" x at time t can only be determined *exactly* if for x and t, $\rho(t, \phi, x, \omega)$ is a Dirac delta distribution in some point (ϕ_0, ω_0).

1.6.2 Kuramoto's coherence transition for $N \to \infty$

In Sec. 1.4.1 we informally introduced the critical coupling strength $C^\natural$ of the classical Kuramoto model (1.2). This bifurcation point can be observed numerically for large but finite N. Y. Kuramoto himself analytically investigated this bifurcation in the $N \to \infty$ limit, and since this is a central result in the Kuramoto model, we shall walk through it here, in a manner inspired by [65].

We assume an even distribution $g(\omega)$. The first step is to translate the model (1.2) to the $N \to \infty$ setting. Applying (1.3a), we can set $\psi = 0$ in the Kuramoto model, so $z = r$, which is in turn given by (1.19). As was explained in the previous Section, the dynamics of the oscillator mass is governed by the PDE (1.18), here the characteristic field v is simply given by

$$v(t, \phi, \omega) = \omega - Cr \sin \phi \tag{1.22}$$

(a derivation for this expression of v is given in Appendix A). We are now looking for steady-state solutions where r is constant, i.e., equilibria in the order parameter. That means the dynamics of the oscillator mass "decouples" in the sense that at each location ϕ on the unit circle, v only depends on ϕ and depends on the rest of the oscillator mass "only" via the constant r. Solutions can only be valid if they are still consistent with the assumptions $r =$const. and $\psi = 0$. The key is to treat the frequency-synchronized and the drifting oscillator mass separately. Frequency-synchronization implies (1.22) $= 0$, which in turn requires $|\omega| \leq Cr$. The drifting part of the oscillator mass is thus the part for which $|\omega| > Cr$. The existence of drift while at the same time $r =$const. may seem paradoxical, but it is possible if the distribution of the drifting oscillator mass is steady in time. Such a stationary density $\rho_{\text{drift}}(\phi|\omega)$ must be inversely proportional to the speed v at phase ϕ so that the density is high (low) where the flow on the unit circle is slow (fast). Making sure that the density integrates

[13] Note that in [11, 12], their symbol "$\rho(t, \phi, x, \omega)$" is meant as a conditional probability density (conditioned on ω), equal to our $\rho(t, \phi, x|\omega)$ that we will use in (1.51),(1.54),(1.55).

to 1 for each ω [65], we get

$$\rho_{\text{drift}}(\phi|\omega) = \frac{\sqrt{\omega^2 - (Cr)^2}}{2\pi|\omega - Cr\sin\phi|}. \tag{1.23}$$

We can split up the order parameter $r = r_{\text{fs}} + r_{\text{drift}}$ by splitting up the inner integral in (1.19) at the boundary $|\omega| = Cr$. For the drifting population we get

$$r_{\text{drift}} = \int_{\mathbb{T}} \int_{|\omega|>Cr} \rho_{\text{drift}}(\phi|\omega) g(\omega) \mathrm{e}^{\mathrm{i}\phi} \mathrm{d}\omega \mathrm{d}\phi. \tag{1.24}$$

Conveniently, due to $g(\omega) = g(-\omega)$ and the fact that $\rho_{\text{drift}}(\phi|\omega) = \rho_{\text{drift}}(\phi + \pi|-\omega)$ (which follows from (1.23)), we get $r_{\text{drift}} = 0$, so $r = r_{\text{fs}}$. This is what we would expect intuitively: the drifting oscillator mass is incoherent and makes a zero contribution to the order parameter. For the frequency-synchronized oscillator mass we get

$$r = \int_{|\omega|\leq Cr} g(\omega) \mathrm{e}^{\mathrm{i}\phi} \mathrm{d}\omega = \int_{|\omega|\leq Cr} g(\omega) \cos\phi \mathrm{d}\omega, \tag{1.25}$$

with ϕ defined via (1.22) $= 0$. The rightmost expression in (1.25) simply follows from the fact that $g(\omega) = g(-\omega)$ for which reason the phases are spread out symmetrically about $\phi = 0$, causing the sine contribution to the complex exponential to vanish. Remembering that $\omega = Cr\sin\phi$ has to be fulfilled due to (1.22) $= 0$, and using a change of variables we get what S. H. Strogatz calls the "self-consistency condition", i.e., the condition ensuring that the original assumptions $r =$const. and $\psi = 0$ still hold:

$$r = Cr \int_{|\phi|\leq\pi/2} g(Cr\sin\phi) \cos^2\phi \mathrm{d}\phi. \tag{1.26}$$

This always has the trivial incoherent solution $r = 0$. There is another branch of solutions, the partially coherent branch with $r > 0$, given by

$$1 = C \int_{|\phi|\leq\pi/2} g(Cr\sin\phi) \cos^2\phi \mathrm{d}\phi, \tag{1.27}$$

which is created in a pitchfork bifurcation at $C = C^\natural$ and exists for $C \geq C^\natural$. The value

$$C^\natural = \frac{2}{\pi g(0)} \tag{1.28}$$

is found by letting $r \to 0^+$ in (1.27). If we take g to be the Lorentzian/Cauchy density $g(\omega) = \Delta/[\pi(\omega^2 + \Delta^2)]$, then (1.27) can be integrated exactly to get

$$r = \sqrt{1 - C^\natural/C}, \quad C \geq C^\natural. \tag{1.29}$$

We see that the partially coherent solution becomes phase-synchronized in the limit $C \to \infty$ with $r = 1$. S. H. Strogatz and R. E. Mirollo later found that the incoherent state $r = 0$ is only neutrally stable for $C < C^\natural$ and unstable for $C > C^\natural$ [69].

1.6.3 The Ott-Antonsen reduction

Y. Kuramoto's ingenious approach to the coherence transition was in 2008 superseded by a more general and more powerful technique. The *Ott-Antonsen (OA) reduction* [8, 9] allows to *exactly* capture the macroscopic behaviour of a coupled oscillator system in its $N \to \infty$ limit, using only a small number of ODEs. We thereby *reduce* a system of ODEs with many variables (due to $1 \ll N < \infty$) to a system with a small number of variables. This and other reduction techniques are also referred to as "mean-field reductions", see [70] for a review.

A requirement for the OA reduction is that the characteristic field v of the coupled oscillator system in its $N \to \infty$ limit can be expressed in the form

$$v(t, \phi, \omega) = \omega + \mathrm{Im}\left(H \mathrm{e}^{-\mathrm{i}\phi}\right) \tag{1.30}$$

where H can be complex and can depend on t, z, ω. For convenience, we restate the transport equation, which governs the oscillator dynamics, and the order parameter:

$$0 = \frac{\partial \rho(t, \phi, \omega)}{\partial t} + \frac{\partial [\rho(t, \phi, \omega) v(t, \phi, \omega)]}{\partial \phi} \tag{1.31a}$$

$$z(t) = \int_{\mathbb{T}} \int_{\mathbb{R}} \rho(t, \phi, \omega) \mathrm{e}^{\mathrm{i}\phi} \mathrm{d}\omega \mathrm{d}\phi. \tag{1.31b}$$

E. Ott and T. Antonsen had the idea to describe $\rho(t, \phi, \omega)$, which is 2π-periodic in ϕ, as a Fourier series

$$\rho(t, \phi, \omega) = g(\omega) \underbrace{\frac{1}{2\pi} \sum_{n \in \mathbb{Z}} \rho_n(t, \omega) \mathrm{e}^{\mathrm{i}n\phi}}_{\rho(t, \phi | \omega)}. \tag{1.32}$$

If the Fourier coefficients $\rho_n(t, \omega)$ obey the form

$$\rho_n(t, \omega) = \begin{cases} \varrho(t, \omega)^n & n \geq 0 \\ (\varrho(t, \omega)^*)^n & n \leq -1 \end{cases} \tag{1.33}$$

with $|\varrho| \leq 1$, and (1.32) is inserted into (1.31), then (1.31) reduces to the ϕ-independent system

$$0 = \frac{\partial \varrho}{\partial t} + \mathrm{i}\omega\varrho + \frac{H\varrho^2 - H^*}{2} \tag{1.34a}$$

$$z(t) = \int_{\mathbb{R}} \varrho(t,\omega) g(\omega) \mathrm{d}\omega. \tag{1.34b}$$

For certain choices of the frequency distribution $g(\omega)$, the integral (1.34b) can be resolved and $z(t)$ can be equated with $\varrho(t,\omega)$ evaluated at a certain fixed (complex) value of ω, translating the PDE (1.34a) into an ODE in z. We shall now exemplify the Ott-Antonsen reduction for the well-known Kuramoto model and the Theta neuron model used in Sec 2.1.

OA-reduction of the Kuramoto model

For the classical Kuramoto model (1.2), $H = Cz$ (for details see Appendix A, eqs. (A.1)-(A.7)). Thus, (1.34) becomes [8]

$$0 = \frac{\partial \varrho}{\partial t} + \mathrm{i}\omega\varrho + C\frac{z\varrho^2 - z^*}{2} \tag{1.35a}$$

$$z(t) = \int_{\mathbb{R}} \varrho(\omega,t) g(\omega) \mathrm{d}\omega. \tag{1.35b}$$

If we take g to be the Lorentzian/Cauchy density $g(\omega) = [\pi(\omega^2+1)]^{-1}$, we see that $g(0) = 1/\pi$, so $C^\natural = 2$ by (1.28). With this choice of g, (1.35) can be closed by an ODE in the order parameter [8]

$$\frac{\mathrm{d}r}{\mathrm{d}t} = \left(\frac{C}{C^\natural} - 1\right) r - \frac{C}{C^\natural} r^3 \tag{1.36}$$

$$\frac{\mathrm{d}\psi}{\mathrm{d}t} = 0 \tag{1.37}$$

which has the stable equilibrium

$$r = \begin{cases} 0 & C < C^\natural \\ \sqrt{1 - C^\natural/C} & C \geq C^\natural \end{cases} \tag{1.38}$$

in agreement with Kuramoto's original analysis, Sec. 1.6.2.

OA-reduction of the coupled Theta neuron model

We here seek to OA-reduce the model given by (1.9)-(1.13), inspired by [63]. Since the model deals with two populations of oscillators, it is convenient to

define an order parameter for both populations individually. Assuming that N is even, each population consists of $M := N/2$ oscillators. We relabel the oscillator's phases as $\phi_{\ell p}$, the phase of the ℓth neuron inside the pth population. The order parameters are then

$$z_p := \frac{1}{M} \sum_{\ell \in [M]} \mathrm{e}^{\mathrm{i}\phi_{\ell p}} \tag{1.39}$$

and we intend to OA-reduce the dynamics of both populations individually as $M \to \infty$. Consider the model defined by (1.9)-(1.13). Using the definition (1.39) and realizing that the real part of the order parameter is simply the sum of cosines of the phases, we can write (1.9) as

$$\frac{\mathrm{d}\phi_{\ell p}}{\mathrm{d}t} = 1 - \cos\phi_{\ell p} + (1 + \cos\phi_{\ell p})[\eta_{\ell p} + \kappa(1 - \mathrm{Re}z_p) + a\kappa(1 - \mathrm{Re}z_q)] \tag{1.40}$$

where $q := 2$ if $p = 1$ and $q := 1$ if $p = 2$. The excitability $\eta_{\ell p}$ of the ℓth neuron in the pth population is drawn from the Lorentzian/Cauchy distribution

$$g_p(\eta) = \frac{\Delta_{\eta p}}{\pi[(\eta - \hat{\eta}_p)^2 + \Delta_{\eta p}^2]} \tag{1.41}$$

where $\hat{\eta}_p$ and $\Delta_{\eta p}$ are the mode and the spread of the excitabilities in the pth population.

Interestingly, the terms $\kappa(1 - \mathrm{Re}z_p)$, $a\kappa(1 - \mathrm{Re}z_q)$ persist as we take the limit $M \to \infty$ (see Appendix of [63]), allowing us to easily write the characteristic field for each population:

$$v_p(t, \phi, \eta) = 1 - \cos\phi + (1 + \cos\phi)[\eta + \kappa(1 - \mathrm{Re}z_p) + a\kappa(1 - \mathrm{Re}z_q)]. \tag{1.42}$$

As can easily be checked, (1.42) has the form (1.30) required for the OA reduction, with

$$\omega_p = 1 + \eta + \kappa(1 - \mathrm{Re}z_p) + a\kappa(1 - \mathrm{Re}z_q) \tag{1.43}$$

$$H_p = \mathrm{i}[\eta + \kappa(1 - \mathrm{Re}z_p) + a\kappa(1 - \mathrm{Re}z_q) - 1]. \tag{1.44}$$

We can thus define the joint probability density $\rho_p(t, \phi, \eta)$ – for a neuron of the pth population having the excitability η and assuming the phase ϕ at time t – via a Fourier series:

$$\rho_p(t, \phi, \eta) = g_p(\eta) \underbrace{\frac{1}{2\pi} \sum_{n \in \mathbb{Z}} \rho_{pn}(t, \eta) \mathrm{e}^{\mathrm{i}n\phi}}_{\rho_p(t, \phi | \eta)} \tag{1.45}$$

where the Fourier coefficients $\rho_{pn}(t,\eta)$ obey the form

$$\rho_{pn}(t,\eta) = \begin{cases} \varrho_p(t,\eta)^n & n \geq 0 \\ (\varrho_p(t,\eta)^*)^n & n \leq -1 \end{cases} \tag{1.46}$$

and $|\varrho_p(t,\eta)| \leq 1 \ \ \forall t$, such that the continuity equation

$$0 = \frac{\partial \rho_p(t,\phi,\eta)}{\partial t} + \frac{\partial[\rho_p(t,\phi,\eta)v_p(t,\phi,\eta)]}{\partial \phi} \tag{1.47a}$$

$$z_p(t) = \int_{\mathbb{T}}\int_{\mathbb{R}} \rho_p(t,\phi,\eta)\mathrm{e}^{\mathrm{i}\phi}\mathrm{d}\omega\mathrm{d}\phi \tag{1.47b}$$

reduces to the ϕ-independent system

$$0 = \frac{\partial \varrho_p}{\partial t} + \mathrm{i}\omega_p\varrho_p + \frac{H_p\varrho_p^2 - {H_p}^*}{2} \tag{1.48a}$$

$$z_p(t) = \int_{\mathbb{R}} \varrho_p(t,\eta)g_p(\eta)\mathrm{d}\eta. \tag{1.48b}$$

Since g_p is the Lorentzian/Cauchy distribution, one can resolve the integral in (1.48) via complex analysis, equate $z_p(t)$ to $\varrho_p(t,\eta)$ evaluated at the residue $\eta = \hat{\eta}_p + \mathrm{i}\Delta_{\eta p}$ and arrive at the OA-reduced system[14]

$$\frac{\mathrm{d}z_p}{\mathrm{d}t} = -\frac{1}{2}\left[(\Delta_{\eta p} - \mathrm{i}[\hat{\eta}_p + \kappa(1-\mathrm{Re}z_p) + a\kappa(1-\mathrm{Re}z_q)])(1+z_p)^2 + \mathrm{i}(1-z_p)^2\right]. \tag{1.49}$$

1.6.4 Graph limits

By now the reader has endured numerous mathematical equations insisting that the $N \to \infty$ limit is both necessary and useful. For example, we have illustrated that in the $N \to \infty$ limit the all-to-all coupled Kuramoto model is governed by the PDE (1.18) with the characteristic field

$$v(t,\phi,\omega) = \omega + C\int_{\mathbb{T}}\int_{\mathbb{R}} \sin(\phi' - \phi)\rho(t,\phi'|\omega')g(\omega')\mathrm{d}\omega'\mathrm{d}\phi' \tag{1.50}$$

(a derivation is given in Appendix A). Even so, we have not ventured much into the graph aspect of the continuum limit, presenting only models on a complete

[14] There are three deviations between the equations used in [63] and this thesis, which do not alter the validity of the mathematical steps nor the result. Firstly, [63] uses only a model of one population, however, the exact same steps can be performed for two populations individually. Secondly, instead of our H, [63] uses f, such that $f_{\text{[63] notation}} = -\frac{1}{2}\mathrm{i}H_{\text{our notation}}$ and $\omega_{\text{our notation}} = h_{\text{[63] notation}}$ and then $v = h + 2\mathrm{Re}(f\mathrm{e}^{\mathrm{i}\phi})$, which is equal to our $v = \omega + \mathrm{Im}(H\mathrm{e}^{\mathrm{i}\phi})$. Thirdly, $\varrho_{\text{our notation}} = (\varrho_{\text{[63] notation}})^*$.

graph or on a combination of two complete graphs and a complete bipartite graph. In order to generalize, e.g., (1.50) to more general graphs, we have to understand how to describe a graph if the number of vertices goes to infinity. We shall here introduce two useful ways of doing so: graphons [71, 72] and graphops [73]. Note that these techniques are only available for undirected graphs, as directed graphs would introduce further mathematical complications that are to date not tractable. We shall thus assume undirected graphs for the remainder of this Section. Since graphops are linear operators on a certain vector space, a basic understanding of functional analysis is beneficial, see e.g. [74, 75].

Graphons

For graphs with $N < \infty$ vertices, the vertex set is simply $\Omega = [N]$. One could interpret the weighted adjacency matrix $\boldsymbol{\kappa}$ as a function on a discrete domain, $[N] \times [N] \to \mathbb{R}$, i.e., it maps each pair of vertices to a real-valued weight. As $N \to \infty$, the vertex set of graphs of infinite size could be identified with the countable set $\mathbb{N}$, however, we take a different approach and describe the vertex set in the $N \to \infty$ limit via the uncountable set $[0, 1]$, where the continuum of infinitesimally small vertices are lined up in a line of unit length. One can now think of a function that maps pairs of vertices to an edge weight in the following way:

Definition 25 ***Graphon.*** *Let $\Omega = [0, 1]$. A graphon is a function $K(x, y) : \Omega \times \Omega \mapsto [-1, 1]$ that is measurable*[15] *and symmetric (i.e., $K(x, y) = K(y, x)$).*

This graphon limit K thus describes the "weighted adjacency matrix as a function", but in the $N \to \infty$ setting. A sequence of graphs $\{\boldsymbol{\kappa}_N\}_{N\in\mathbb{N}}$ can thus converge to a graphon K as $N \to \infty$. Just like the lth row (or column) of the matrix $\boldsymbol{\kappa}$ is the neighbourhood of the lth vertex, $K(x, y)$ is the neighbourhood of the vertex x in the $N \to \infty$ setting. From the definition of a graphon it is evident that we have rescaled the edge weights to fit into the range $[-1, 1]$. The conditions for the convergence, and the metric in which it occurs, are not discussed here, the interested reader is referred to [71, 72, 76]. However we give the intutition behind this convergence [72]: View the matrix $\boldsymbol{\kappa}$ as a greyscale square pixel picture with side length 1 such that for each pair l, m we draw a pixel at the position $[(l-1)/N, l/N) \times [(m-1)/N, m/N)$ where the value κ_{lm} is encoded by the colour of the pixel. If we increase N, the resolution of the picture gets finer, until in the limit $N \to \infty$ the image no longer consists of pixels, but of infinitesimally small dots of colour, or "how images looked before

[15] we will not dive into measure theory in this thesis, here it will suffice to know that every piecewise continuous function is measurable [74].

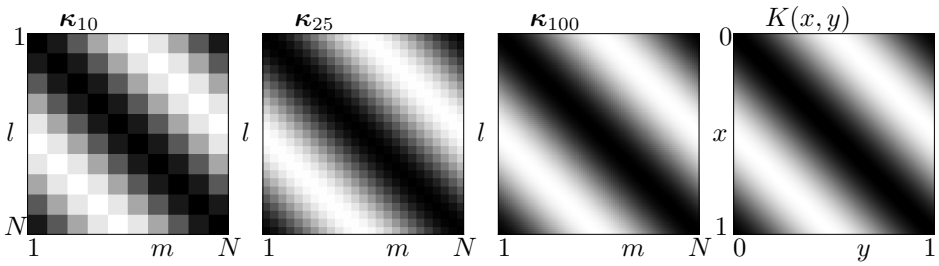

Figure 1.4: Illustration of convergence of a sequence of graphs $\{\boldsymbol{\kappa}_N\}_{N\in\mathbb{N}}$ to a graphon $K(x,y)$. Here we have chosen $(\kappa_{lm})_N = \frac{1}{2}\left(1+\cos 2\pi\frac{l-m}{N}\right)$ and $K(x,y) = \frac{1}{2}(1+\cos 2\pi(x-y))$. White encodes 0 while black encodes 1.

they became digital". This picture is described by the function $K(x,y)$, see also Fig. 1.4 (note that a similar figure is found in [72], Fig.1).

We have thus illustrated how a (coupling) graphon generalizes a coupling matrix to the $N\to\infty$ setting if the matrix is interpreted as a function (as described above). The Kuramoto model (1.5) is in the $N\to\infty$ limit governed by (1.18) with

$$v(t,\phi,x,\omega) = \omega + C\int_{y\in\Omega}\int_{\mathbb{T}}\int_{\mathbb{R}}\sin(\phi'-\phi)K(x,y)\rho(t,\phi',y|\omega')g(\omega')\mathrm{d}\omega'\mathrm{d}\phi'\mathrm{d}y, \tag{1.51}$$

and $\Omega=[0,1]$, for details see [12]. Note that we are now dealing with a family of PDEs, one for each vertex x.

Graphops

One could interpret the weighted adjacency matrix $\boldsymbol{\kappa}$ as a linear operator on the finite-dimensional vector space $\mathbb{R}^N$. The matrix is thus simply a mapping $\mathbb{R}^N\to\mathbb{R}^N$, mediated by the matrix-vector product. A graphop generalizes this notion, since a graphop can act on infinite-dimensional vector spaces such as L^2, the space of square-integrable functions. If the vertex set is taken as a more general set than, e.g., $[0,1]$ like in the graphon case, we can introduce a graphop in the following way:

Definition 26 ***Graphop.*** *Let Ω be a compact set. A graphop is a bounded, self-adjoint linear operator $A: L^2(\Omega)\mapsto L^2(\Omega)$ that is positivity-preserving, i.e., if the function $f\in L^2(\Omega)$ fulfills $f(x)\geq 0$ almost everywhere on Ω, then the function $Af\in L^2(\Omega)$ fulfills $(Af)(x)\geq 0$ almost everywhere on Ω.*

Note that, following standard operator notation, Af means "A acting on the function f" and Af is again a function. $(Af)(x)$ then means "the function Af evaluated at x". A graphop can thus be seen as a generalized graph of infinite size. The property "self-adjoint" [75] of the graphop stems from the undirectedness of the graph. Certain graphops can be defined via a graphon kernel K, this kind of graphop is called *graphon operator* in [77]. In this case again $\Omega = [0, 1]$ and we can write

$$(Af)(x) = \int_\Omega K(x, y) f(y) \mathrm{d}y. \tag{1.52}$$

Note that also the general graphop, which is not necessarily a graphon operator, can be written as an integral operator:

$$(Af)(x) = \int_{y \in \Omega} f(y) \mathrm{d}\nu_x(y). \tag{1.53}$$

Here too, the fibre measure $\nu_x(y)$ represents the neighbourhood of the vertex x.[16] We have thus illustrated how a (coupling) graphop generalizes a coupling matrix to the $N \to \infty$ setting if the matrix is interpreted as an operator (as described above). We emphasize that a graphop is not a generalization of a graphon, but of a graphon operator.[17]

With that we are ready to state the characteristic field in the graphop case. To bridge the gap between the various generalizations of the Kuramoto model studied, look again at the dynamics of the lth oscillator in (1.2). There the summation was not weighted with any graph properties since the graph was complete. Then we had (1.5), where the summation was weighted with the neighbourhood of the lth vertex. In (1.51) the outer integral was an integral over the neighbourhood of "the vertex" x. Now we let the graphop A act on $\rho(t, \phi, x, \omega)$, so we again integrate this density over the neighbourhood of x (see (1.53)). The Kuramoto model on a graphop is thus governed by (1.18) with

$$v(t, \phi, x, \omega) = \omega + C \int_{\mathbb{T}} \int_{\mathbb{R}} \sin(\phi' - \phi)(A\rho)(t, \phi', x|\omega') g(\omega') \mathrm{d}\omega' \mathrm{d}\phi'. \tag{1.54}$$

If A is a graphon operator, (1.54) is equivalent to (1.51), otherwise, writing out the integration over fibre measures implied by the graphop action in (1.53), we

[16] The mathematical details of fibre measures are not important in this thesis, as the spherical graphop used in [2] uses the uniform fibre measure, which is sufficiently easy.

[17] Also, a graphop is a generalization of a coupling matrix if the matrix is interpreted as a linear operator. Indeed, for the choice $\Omega = [N]$, $L^2(\Omega)$ can be identified with $\mathbb{R}^N$. Af is simply the matrix-vector product. Finally, $(Af)(x)$ is the xth entry of the vector Af with $x \in [N]$.

find that (1.54) is equivalent to

$$v(t,\phi,x,\omega) = \omega + C\int_{y\in\Omega}\int_{\mathbb{T}}\int_{\mathbb{R}} \sin(\phi'-\phi)\rho(t,\phi',y|\omega')g(\omega')\mathrm{d}\omega'\mathrm{d}\phi'\mathrm{d}\nu_x(y), \tag{1.55}$$

for details see [11,12]. Note that we are now dealing with a family of PDEs, one for each vertex x. We shall use (1.54) with the stochastic Kuramoto model in Sec. 2.2.

In this Introduction, we have familiarized ourselves with the coupled Theta neuron model and the Kuramoto model with various properties. We have taken both models to the $N \to \infty$ limit, which even allows for various generalizations of the all-to-all graph, compare eqns. (1.50), (1.51), (1.54), (1.55). We shall now present the results of this thesis.

Chapter 2

Results

Having established the basics of (adaptive) oscillator systems and having defined all technical terms, we shall now summarize the three articles which this thesis is based on. The notation used here is consistent with the Introduction (Chapter 1) and thus not entirely consistent with the articles themselves, which mutually differ in notation.

2.1 Results of article [1] – Birth and destruction of collective oscillations in a network of two populations of coupled type 1 neurons

The article deals with a coupled Theta neuron model introduced in [64], the derivation of which we repeated in Secs. 1.5 and 1.6.3:

$$\frac{\mathrm{d}\phi_{\ell p}}{\mathrm{d}t} = 1 - \cos\phi_{\ell p} + (1+\cos\phi_{\ell p})(\eta_{\ell p} + I_p), \quad \ell \in [M], \;\; p \in \{1,2\} \tag{2.1a}$$

$$\eta_{\ell p} \sim g(\eta) = \frac{\Delta_\eta}{\pi[(\eta-\hat{\eta})^2 + \Delta_\eta^2]} \tag{2.1b}$$

$$\frac{\mathrm{d}z_p}{\mathrm{d}t} = -\frac{1}{2}\left[(\Delta_\eta - \mathrm{i}\hat{\eta} - \mathrm{i}I_p)(1+z_p)^2 + \mathrm{i}(1-z_p)^2\right], \quad p \in \{1,2\} \tag{2.1c}$$

$$I_1 = \kappa(1 - \mathrm{Re}z_1) + a\kappa(1 - \mathrm{Re}z_2) \tag{2.1d}$$

$$I_2 = a\kappa(1 - \mathrm{Re}z_1) + \kappa(1 - \mathrm{Re}z_2) \tag{2.1e}$$

where (2.1a) is a model of $N = 2M < \infty$ Theta neurons, organized in 2 populations $p \in \{1,2\}$. Coupling occurs via the input currents I_1, I_2. They capture, via the quantities $1 - \mathrm{Re}z_p$, how close the oscillators are, on average, to the spiking threshold $\phi_{\ell p} = \pi$, i.e., they capture the macroscopic spiking activity of the populations 1 and 2. (2.1c) is the OA-reduced, $N \to \infty$ version of (2.1a). In the article, analysis is carried out on (2.1c) since its low number of ODEs allows for easy treatment of the macroscopic dynamics of (2.1a). We investigate the bifurcation structure of the OA-reduced system (2.1c), where the parameters are set to $\Delta_\eta = 1/100, \hat{\eta} = -1$, i.e., we assume relatively similar, but not identical, inhibitory neurons, these two parameters are identical for both populations.

We can define the *firing activity / firing rate / spiking activity* as the amount of flux through the point $\phi = \pi$ (where the Theta neuron spikes). The firing rate of the pth population is exactly $\pi^{-1}\mathrm{Re}[(1-z_p{}^*)/(1+z_p{}^*)]$ [78]. We find that asymmetric states, i.e. states where both populations have distinct dynamical behaviour (this always implies distinct levels of firing activity and distinct levels of coherence in this article), are possible despite the two populations having identical properties. To see this we first consider two special cases. Clearly, the choice $a = 1$ causes both populations to "melt" into one big population of size $2M$, while $a = 0$ decouples both populations. We show that a single population with negative $\hat{\eta}$ and positive κ can have two coexisting stable states, one *quiescent* (low firing activity) and one *spiking* (high firing activity).[1] It thus comes as no surprise that the two-population system with $a = 0$ exhibits asymmetric states: since the populations decouple, one population can assume

[1] the transition between quiescent and spiking is smooth, there is no strict threshold in the firing rate that distinguishes the two. They define each other by contrast.

the stable quiescent state and the other population can assume the stable spiking state. Moreover, there are two symmetric states where both populations assume the same state. Interestingly, as a is increased above zero, pitchfork bifurcations emerge that keep the asymmetric states alive and stable, coexisting with the stable symmetric states. While for positive a, stable asymmetric states only persist in a comparably small parameter region, this region is vast for negative a. Stable asymmetric states can be either equilibria or limit cycles (created in Hopf bifurcations when a is increased further above zero). Stable symmetric states are also observed, but they can only be equilibria. All observed stable states, whether they are symmetric or asymmetric, oscillatory or steady states, underlie a tradeoff between firing activity and coherence: each of the two populations can either have high firing activity and low coherence[2] or vice-versa. This also implies that the asymmetric states always have both a quiescent (and quite coherent) and a spiking (and poorly coherent) population.

The bifurcation scenarios of the asymmetric states can become quite involved. We report three different creation-destruction-patterns of stable asymmetric limit cycles. The bifurcation landscape in κ, a parameter space is quite complex, consisting, amongst others, of the following "landmarks" (see Fig. 6 in [1]):

1. A cusp bifurcation (CP) that limits the existence of stable asymmetric states in the direction of positive a.
2. A Generalized Hopf (GH) bifurcation [79] that separates a Hopf bifurcation curve into a subcritical and a supercritical segment.
3. A Saddle-node-of-limit-cycles (SNLC) curve that emanates from the GH point.
4. A cusp of SNLC curves (CPC), where said SNLC curve meets with another branch of SNLC curves.
5. A point we call SLH, where the other branch of SNLC curves collides with a homoclinic (HC) curve.

The general picture is the following: if κ is sufficiently low (high), then both poulations have identical low (high) spiking activity. If κ is intermediate and a is in a certain intermediate range between 0 and 1, then stable asymmetric stationary states coexist with the symmetric states. Oscillatory stable asymmetric states exist too, they get created in Hopf bifurcations and exist in a much smaller κ, a parameter range. For $a < 0$ however, i.e., repelling coupling between both populations, asymmetric states exist in a vast range of $\kappa > 0$.

[2] this is true if κ is not too high, in fact, in the limit $\kappa \to \infty$, the neurons are phase-synchronized and have infinite spiking activity.

2.2 Results of article [2] – Graphop Mean-Field Limits and Synchronization for the Stochastic Kuramoto Model

In this article, we deal with the system of SDEs

$$\mathrm{d}\phi_l = \mathrm{d}t\frac{C}{N}\sum_{m=1}^{N}\kappa_{lm}D(\phi_m-\phi_l)+\sigma_B\mathrm{d}B_l,\quad l\in[N] \tag{2.2}$$

modeling the evolution of $N<\infty$ identical Kuramoto oscillators with an additive N-element white noise vector $\sigma_B\mathrm{d}\boldsymbol{B}=\sigma_B\mathrm{d}(B_1,\dots,B_N)^\top$ with zero mean and variance σ_B^2. Here, D is an even 2π-periodic function. The result of the article is analytically obtained for the $N\to\infty$ limit of the system (2.2), where the density $\rho(t,\phi,x)$ describes the oscillator mass at the position x in the vertex set with phase ϕ at time t. The temporal evolution of $\rho(t,\phi,x)$ obeys the Fokker-Planck equation (2.3a):[3]

$$0=\frac{\partial\rho(t,\phi,x)}{\partial t}+\frac{\partial[\rho(t,\phi,x)v(t,\phi,x)]}{\partial\phi}+\frac{\sigma_B^2}{2}\cdot\frac{\partial^2\rho(t,\phi,x)}{\partial\phi^2} \tag{2.3a}$$

$$v(t,\phi,x)=C\int_{\mathbb{T}}D(\phi'-\phi)(A\rho)(t,\phi',x)\mathrm{d}\phi'. \tag{2.3b}$$

In (2.3b), coupling is mediated by a graphop A acting on the density $\rho(t,\phi,x)$. If A has a graphon kernel, then the coupling can be thought of as the usual coupling via an undirected graph but in the $N\to\infty$ limit; if A cannot be described by a graphon kernel, the coupling, while still undirected, is more abstract. We Fourier-transform (2.3a) and obtain for each $j\in\mathbb{N}$ an ODE in the jth Fourier coefficient of the solution $\rho(t,\phi,x)$ to (2.3a). Linearizing this ODE around the incoherent state $\rho=1/(2\pi)$, we obtain for each j an ODE that is decoupled, i.e., the dynamics of the jth Fourier coefficient is only influenced by the jth Fourier coefficient. We find a condition for the linear stability of the incoherent state (in all Fourier coefficients), this condition is fulfilled if $C<C^\natural$ for

$$C^\natural=\inf_{\lambda,j}\frac{j^2\sigma_B^2}{2\mathrm{i}\lambda D_j}\bigg|_{\mathrm{i}D_j\lambda\geq 0} \tag{2.4}$$

where D_j is the jth Fourier coefficient of D and λ is a spectral value of A.[4] The incoherent state is thus linearly, i.e., locally, stable for $C<C^\natural$ and unstable for

[3] note that (2.3b) resembles (1.54) but for identical oscillators.

[4] The spectrum is explained in [2, 75](7.2-1). Note also the simplifications of the spectrum due to the fact that we are dealing with a bounded self-adjoint linear operator that maps from a Hilbert space to itself: firstly, the spectrum is real and bounded, secondly, the residual spectrum is empty [75](9.2-4).

$C > C^\natural$. If the incoherent state is unstable, we may expect the system to run into partially coherent attractors. For the remainder of the article we make the simplification $D = \sin$ and get

$$C^\natural = \frac{\sigma_B^2}{\Lambda(A)} \tag{2.5}$$

where $\Lambda(A)$ is the supremum of the magnitudes of the spectral values of A. To complement this theoretical analysis, we numerically tested the result (2.5) for certain graphops. Numerical testing is restricted to an $N < \infty$ version of the governing model (2.3), namely (2.2), and thus we need to approximate each graphop by a graph matrix. Nevertheless, we compare our numerical results to the value (2.5) found via the respective graphop spectrum. However, for graphops whose spectra lack an analytical expession, we need to adjust (2.5) to the finite-dimensional case:

$$C^\natural = \frac{\sigma_B^2}{\Lambda(\boldsymbol{\kappa})}. \tag{2.6}$$

Here, $\Lambda(\boldsymbol{\kappa})$ is simply the largest magnitude of an eigenvalue of $N^{-1}\boldsymbol{\kappa}$, where $\boldsymbol{\kappa}$ is a graph approximation to A. Our numerical tests were conducted via numerical integration of (2.2) for $N = 1000$, various values of C, various realizations of the Brownian motion vector $\boldsymbol{B}$, and various (random realizations of) graphs $\boldsymbol{\kappa}$. The tests revealed that especially regular, dense graphs (i.e., graphs with relatively many edges) show the behaviour that (2.6) predicts: the level of coherence rises, and the order parameter r asymptotically approaches 1, as C is increased above $C^\natural$. However, the regular ring lattice graph with a small number of edges, which (at least for $\sigma_B = 0$) has a stable incoherent solution coexisting with the partially coherent state [26], can fail to exhibit this clear coherence transition. Also, sparse irregular graphs walk a much longer path to a given level of coherence. As an example, the "Lorentzian" graph is somewhat "bipartite" in the following sense: there are two very small populations in the graph between which a few edges with very strong weights exist. All other coupling weights are very small (the graph is connected). The matrix $\boldsymbol{\kappa}$ of the graph is given by

$$\kappa_{lm} = \frac{\mu/\pi}{\left(\frac{l}{N} - x_0\right)^2 + \left(\frac{m}{N} - y_0\right)^2 + \mu^2} + \frac{\mu/\pi}{\left(\frac{l}{N} - y_0\right)^2 + \left(\frac{m}{N} - x_0\right)^2 + \mu^2} \tag{2.7}$$

where we used the values $x_0 = 0.25, y_0 = 0.75, \mu = 0.01,\ 0.001$, see also Fig. 2.1. The Lorentzian graph has a very "slow" coherence transition even when compared to its own $C^\natural$, i.e., it requires a much higher $C/C^\natural$ to reach the same level of coherence compared to dense regular graphs. The Lorentzian graph is thus an example of a graph where the analytical statement (2.4) is less predictive. Other graphs used in the numerical analysis were the complete graph, the sinusoidal graph (see Fig. 1.4), the regular ring lattice graph, the small-world graph and the ER graph. Finally, we propose a matrix approximation to the spherical graphop and use this "spherical graph" in our numerical simulations.

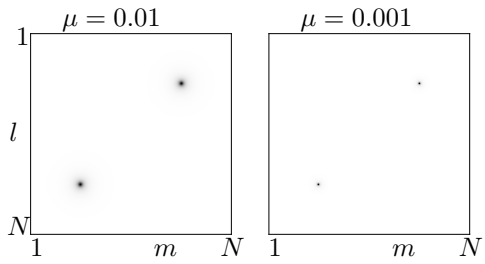

Figure 2.1: Matrix $\boldsymbol{\kappa}$ of "Lorentzian" graph. White encodes $\kappa = 0$ while black encodes $\kappa \geq 31.8374$ (which is the maximum value of κ_{lm} for $\mu = 0.01$). The colour range of the image of $\boldsymbol{\kappa}$ for $\mu = 0.001$ was also truncated at $\kappa \geq 31.8374$ for better visibility. The maximum κ_{lm} for $\mu = 0.001$ is 318.3105.

2.3 Results of article [3] – Complex dynamics in adaptive phase oscillator networks

In this article we deal with the adaptive Kuramoto-Sakaguchi model

$$\frac{\mathrm{d}\phi_l}{\mathrm{d}t} = \omega_l + \frac{1}{N}\sum_{m\in[N]} \kappa_{lm}\sin(\phi_m - \phi_l + \alpha) \tag{2.8a}$$

$$\frac{\mathrm{d}\kappa_{lm}}{\mathrm{d}t} = \varepsilon(1 + a\cos(\phi_l - \phi_m + \beta) - \kappa_{lm}) \tag{2.8b}$$

which is inspired by [52] but employs non-identical oscillators and includes a constant offset 1 in the adaptation (2.8b). We mainly study this model for $N = 2$, the model becomes three-dimensional after making use of (1.3) and setting $\phi := \phi_1 - \phi_2$ and $\omega := \omega_1 - \omega_2$:

$$\frac{\mathrm{d}\phi}{\mathrm{d}t} = \omega + \frac{1}{2}\kappa_{12}\sin(\alpha - \phi) - \frac{1}{2}\kappa_{21}\sin(\alpha + \phi), \tag{2.9a}$$

$$\frac{\mathrm{d}\kappa_{12}}{\mathrm{d}t} = \varepsilon(1 + a\cos(\beta + \phi) - \kappa_{12}), \tag{2.9b}$$

$$\frac{\mathrm{d}\kappa_{21}}{\mathrm{d}t} = \varepsilon(1 + a\cos(\beta - \phi) - \kappa_{21}). \tag{2.9c}$$

ε is fixed at 0.2, and β, the adaptation shift, determines whether the graph is directed ($\beta = 0, \pi$) or undirected ($\beta \neq 0, \pi$). We study dynamics and bifurcations of (2.9). The stable states seen in this model are either equilibria or oscillatory states (limit cycles or chaos). Each observed stable oscillatory state is either a drift or a libration.

The classical, non-adaptive, all-to-all coupled Kuramoto model is recovered for the choice $a = 0$. This model exhibits a simple SNIC bifurcation at $\omega = 1$ which

divides the ω parameter space into 2 simple regions: for $|\omega| > 1$, the only stable state is a drift, for $|\omega| < 1$ the only stable state is a frequency-synchronized equilibrium. This basic pattern reappears in the general $a \neq 0$ model: for all parameter choices, the model always exhibits a stable drift state when $|\omega|$ is sufficiently large. When $|\omega|$ is sufficiently small, 1 or 2 stable frequency-snychronized equilibria or oscillatory states can (co)exist.

Importantly, if the adaptivity parameter a is in some neighbourhood of 0, the dynamics is qualitatively identical to the non-adaptive, all-to-all coupled Kuramoto model. a has to be sufficiently different from 0 in order to admit "truly adaptive" dynamics, i.e., dynamics that is only possible if coupling strengths can change dynamically in a wide enough range. This "truly adaptive" dynamics is brought about by bifurcations such as cusp or Bogdanov-Takens. Indeed, for $\beta = 0 < a < 1, |\omega|$ sufficiently small, the system runs into the stable, frequency-synchronized state with high $\kappa_{12} = \kappa_{21}$. This state is qualitatively identical to the frequency-synchronized state in the classical all-to-all Kuramoto model (1.2) with $N < \infty$ and C sufficiently larger than $C^{\natural}$. In contrast, for $\beta = 0, a > 1, |\omega|$ sufficiently small, the system – now past a cusp point – offers a bistability (between two frequency-synchronized equilibria) that the classical Kuramoto model does not.

If the adaptation shift $\beta \neq 0$, the system (2.9) is 3-dimensional, which allows for a much more intriguing bifurcation landscape. For example, a complex chain of bifurcations gives rise to drift states that are a mixture of librations and rotations, we call these states mixed oscillations. We observed such mixed oscillations – which are alternatingly either periodic limit cycles or chaotic attractors as ω is varied in an intermediate range – for $\alpha = -\pi/10, \beta = \pi/4$. Moreover, the interplay of bifurcations GH, SNLC, CPC, HC, SLH reported in [1] reappears for this parameter choice.

To give an outlook towards larger systems, we also conducted some simulations of system (2.8) for $N = 50$, $\alpha = \beta = 0$ and various a. It turns out that the basic pattern of the $N = 2$ system carries over to larger system sizes. Indeed, if the intrinsic frequencies ω_l follow a normal distribution with sufficiently small standard deviation σ_ω, the system runs into stable stationary frequency-synchronized states. If σ_ω is sufficiently large, the oscillators drift, and the couplings κ_{lm} oscillate accordingly. For intermediate σ_ω, there is partial coherence, where some oscillators drift and some are weakly or almost frequency-snychronized (such a constellation of oscillator groups requires at least $N = 3$). For a sufficiently positive, "antipodal" states are possible (see also Sec. 3.3).

Chapter 3

Discussion

In the previous Chapter we have summarized the three articles [1–3]. We shall now discuss and compare the results. To this end, we focus on one aspect at a time, namely graphs (Sec. 3.1), synchronization and coherence (Sec. 3.2), populations (Sec. 3.3), bifurcations (Sec. 3.4), oscillations (Sec. 3.5), and symmetry (Sec. 3.6). We then suggest directions for future work in Sec. 3.7. Finally, we conclude this thesis with a brief remark in Sec. 3.8.

3.1 Graphs

In all three articles we set out to learn about dynamics on graphs: we were interested in the behaviour of phase oscillators as they dynamically influence each other when coupled via a graph. In [3] we additionally ask about dynamics of graphs. We always ask how the dynamical behaviour of the oscillators depends on the graph and to this end we always perturb away from the complete graph. In [1] we do so by gradually weakening the inter-population coupling weight compared to the intra-population coupling weight. In [2] we start with the complete graph and then investigate more complicated graphs. In [3] we perturb from the all-to-all coupled, non-adaptive Kuramoto model by gradually increasing the adaptivity parameter, allowing for an increasingly adaptive

and increasingly complicated graph. In all three cases, the complexity of the dynamics increases with the complexity of the graph.

3.2 Synchronization and coherence

In all three articles, the respective model exhibits synchronization and/or different levels of coherence. In [1], the smallest level of coherence, with the order parameter almost zero, is seen for a certain large coupling. The firing rate is high in this state, yet referring to this state as "drift" would not be entirely correct, as the model is formulated in a macroscopic way and dynamics of the individual phases is unknown. Drift is seen for sufficiently weak coupling $C < C^\natural$ [2], and sufficiently large difference in intrinsic frequencies, ω, or σ_ω [3], respectively. In the limits $\kappa \to -\infty$ or $\kappa \to \infty$ [1], $C \to \infty$ [2], and $\omega, \sigma_\omega \to 0$ [3], the models exhibit phase-synchronization. The intermediate regime between the extremes drift and phase-synchronization is more layered. In [1], the macroscopic formulation of the model does not give us insights into specific types of synchronization (as of Definitions 1 to 4), this would require a view of the individual oscillators, see Sec. 3.7.1. We observe that coherence is high (low) if coupling is low (high), with multistability between low and high coherence for intermediate coupling. In the finite-N reprentation of the stochastic model in [2], even for $C > C^\natural$, frequency-synchronization is ruled out due to the stochasticity of the model. Strictly speaking, the synchronization is not even weak, since the oscillators' phases can always through random motion escape any subset of the unit circle. Still, for $C > C^\natural$, most of the oscillators stay within a certain distance of each other most of the time, and this distance shrinks as C is increased, thus increasing the coherence. In [3], the intermediate regime between drift and phase-synchronization hosts weak or frequency-synchronization. As mentioned in Sec. 2.1, the Theta neuron model in [1] features a tradeoff between spiking and coherence. This tradeoff is illustrated for equilibria of the OA-reduced Theta neuron system (2.1c) in Fig. 3.1. In the Kuramoto model, this tradeoff occurs rather trivially. Terms like spiking or firing are not commonly used in the Kuramoto model, since this is neuroscience jargon, but here we can say that Kuramoto oscillators with nonzero dynamic frequency are "firing". But zero frequency is equivalent to frequency-synchronization due to the frequency-shift invariance (1.3b). States of high coherence in the Kuramoto model are usually caused by frequency-synchronized oscillators, hence the trivial either-or-relation between coherence and spiking.

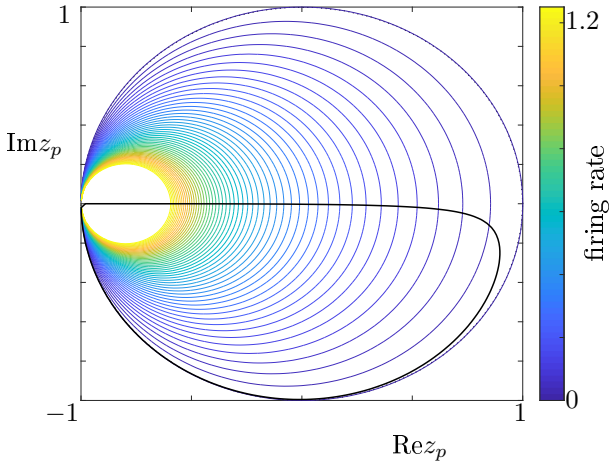

Figure 3.1: The coloured lines are the level curves of the firing rate $\pi^{-1}\mathrm{Re}[(1-{z_p}^*)/(1+{z_p}^*)]$ versus the order parameter z_p. Since the firing rate goes to infinity as $z \to -1$, we in this illustration cut off the level curves at the arbitrary value 1.2. The firing rate is zero for $r = 1$ except at $z = -1$. It was found that all equilibria of the OA-reduced Theta neuron system (2.1c) have their z_p's lying on the black curve. For $\kappa \to -\infty$ ($\kappa \to \infty$), the black curve is travelled in (counter)clockwise direction. For the κ, a parameter range shown in [1], Fig. 6, the equilibria have their z_p's lying on the lower right quadrant of black curve. Relatively high coherence is found close to the rim of the unit circle, where the firing rate is close to zero. High firing rate is found close to $z_p = 0$, where coherence is low. The Figure is taken from [80], Fig. 4.2.

3.3 Populations

The notion of populations plays a role in at least [1, 3]. In [1], oscillators are grouped into populations a priori. In [3], for $N = 2$, each oscillator is trivially a population of its own, for $N = 50$ and a sufficiently positive, we saw two populations of sizes 48 and 2 that repel each other while internally having a very high level of coherence.[1] In the intermediate regime (between frequency-synchronization of all oscillators and drifting of all oscillators) for $N = 50$, one might view the weakly synchronized oscillators as one population and the drifting oscillators as another. In [2], at least for the complete graph, the $N = 1000$ oscillators do not form populations: even for $C > C^\natural$, the partially coherent regime, all oscillators fluctuate randomly, however, since they are identical, they do not divide into drifters and non-drifters. Yet, if we wanted to enforce populations, we could separate the oscillators into populations based on how far they are from the mean phase, then oscillators would randomly switch between populations, with all oscillators being equiprobable to be in the "mean" population. The situation might be different if the underlying graph suggests populations a priori, see Sec. 3.7.2. At least the models in [1, 3] allow for asymmetric states where both populations differ in their behaviour, e.g., their amount of internal coherence [1], their size [3] or their coupling weight(s) to the respective other population [3]. In [2], it is conceivable that the Lorentzian graph provides asymmetric states, see Sec. 3.7.1. In [1, 3] there are also symmetric states where both populations show identical behaviour. In [3], symmetric states are so far only seen in systems of two oscillators on an undirected graph. "Antipodal" symmetric states on undirected graphs for $N = 50$ with *identical* sizes of both populations do not appear to be stable in the numerical experiments.

3.4 Bifurcations

Bifurcations are vital to all three articles and determine the dependence of the respective model on parameters. In [2], one bifurcation is studied: the change of stability of the incoherent state in the macroscopic formulation of the model. This is the fundamental bifurcation in the Kuramoto model and its variants and plays a role in how the coherence transition unfolds. In [3], the coherence transition – here organized around a saddle-node bifurcation in the microscopic model

[1] This state is very close to what [52] calls an antipodal state. Berner et al.'s definition of an antipodal state requires two populations which are internally phase-synchronized while the populations are anti-phase synchronized to each other. Here, the populations are internally only frequency-synchronized with the pairwise differences between phases of the same population (distinct populations) being close to zero (π).

– reappears for all parameter choices: if the difference between the intrinsic frequencies is small enough, there is weak synchronization in the form of libration cycles, or even frequency-synchronization in the form of equilibria. If oscillators are identical, there is phase-synchronization. If the difference between the intrinsic frequencies is large enough, the oscillators drift. In the Theta neuron model in [1], the same general pattern is seen, albeit in the opposite direction. Here, (unlike in [2, 3],) there is a fixed non-zero amount of heterogeneity Δ_η in the distinguishing property of the oscillators, namely their inclination towards spking. In contrast to [2], a stronger, more positive (weaker, more negative) coupling decreases (increases) the order parameter r_p and increases (decreases) the firing rate. The most complicated dynamical behaviour of the model in [1] occurs when the coupling strength is at a medium value. The Theta neuron is inherently more complex than the Kuramoto oscillator and thus naturally exhibits more complex synchronization behaviour [81], therefore models employing different oscillator types are not easily compared. In this regard it is interesting to note that the models in [1, 3] show similar bifurcation patterns. More interesting still, the model in [3] requires adaptivity as well as broken parameter symmetries to achieve the same level of complexity in its bifurcations as the model in [1] with a constant coupling graph and purely symmetric parameters. Yet, as far as the analyses conducted in this work are concerned, the dynamics of [3] offers more complicated behaviour than those of [1]: for certain parameter choices, [3] allows for period-doubling bifurcations which pave the way to chaos. Chaotic dynamics may yet occur in the model of [1] if parameter symmetries are sufficiently broken. In [3], bifurcation scenarios and dynamical behaviours generally complicate if the adaptivity parameter is chosen strongly negative, and choosing non-zero adaptation shift and Sakaguchi phase lag and an intermediate intrinsic frequency difference can further complicate the behaviour.

3.5 Oscillations

Oscillations can either be microscopic or macroscopic. To state the obvious, in all three models, the individual oscillators oscillate, like the models are designed to. Macroscopic quantities can also oscillate, a typical example is the fluctuation in the order parameter of the Kuramoto model due to finite-size effects. This is also encountered in [2] and in [3] for $N = 50$, in [2] these fluctuations are also due to the stochasticity of the model. In [1], a stable limit cycle oscillation in the macroscopic model implies that the macroscopic behaviours of the populations periodically swing back and forth between *higher spiking activity with lower coherence* and *lower spiking activity with higher coherence*. In [3], oscillations for $N = 2$ have a microscopic meaning: the phase difference between the two oscillators, as well as the coupling weights between the two, oscillate, either

article	[1] "Birth and destruction..."	[2] "Graphop Mean-Field..."	[3] "Complex dynamics..."
oscillators	Theta neuron	Kuramoto	Kuramoto
identical oscillators	no	yes	for $\omega = 0$
N	∞ (OA)	$\infty, 1000$	$2, 50$
# dynam. variables	4	$\infty, \mathcal{O}(10^5)$	$1, 2, 3, \mathcal{O}(10^3)$
adaptive graph	no	no	no, yes
directed graph	no	no	no, yes
graph type(s)	κ·complete+ $a\kappa$·complete bipartite	complete, spherical, sinusoidal, Lorentzian, reg.ring lat., small-world, Erdös-Rényi	complete, antipodal, undefined
populations	yes	no	for $N = 50$, $a \gg 1 \gg \sigma_\omega$
bifurcation(s)	complex	at $C^\natural$	complex
synchronization (see Defs. 1 to 4)	n.a.	weak	weak, freq., (anti-)phase
coherence	partial	incoh., partial	incoh., partial, perfect ($\omega = 0$)
symmetric states	equilibria	—	equilibria, drift
asymmetric states	equilibria, limit cycles	—	equilibria, drift, librations
oscillations	limit cycles (macroscopic)	fluctuations in r	librations, drift, fluctuations in r, (periodic/chaotic)
drift (Def. 6)	n.a.	stochastic	rotations (+librations)
symm. parameters	$\kappa, a, \hat{\eta}, \Delta_\eta$	κ_{lm}	for $\beta = 0$
asymm. parameters	—	—	for $\beta \neq 0$

Table 3.1: comparison of the models used in articles [1], [2], and [3] and the dynamical behaviours observed.

periodically or chaotically. This oscillation may or may not involve the two oscillators drifting apart. Also for $N = 50$, the drifting phases cause the coupling weights to oscillate accordingly.

3.6 Symmetry

All three models contain symmetry. [2] features exclusively symmetric coupling, this symmetry cannot be broken with the mathematical tools available to date. [1,3] contain much symmetry too, but it can be broken. In [1], the parameter choices made are purely symmetric between the two populations, but the model naturally allows for asymmetric parameter choices too. The model exhibits symmetric dynamical behaviour, but also (despite the symmetric choice of parameters) a lot of interesting asymmetric behaviour, provided that the (positive or negative) coupling between the populations is weak enough. In [3] the model comes with many parameter symmetries and parameter-state-variable symmetries. The coupling graph can be forced directed or undirected via the adaptation shift β, i.e., the choice $\beta = 0$ brings even more symmetry to the model and quenches much of the complicated dynamics seen for $\beta \neq 0$.

A summary of the above comparisons between the articles is found in Table 3.1.

3.7 Directions for future work

Having compared the results of our articles [1–3], we can now offer ideas for future research. Possible research questions can be distinguished into two types: firstly, one could analyze the models of [1–3] from new angles (Sec. 3.7.1), secondly, one might study (parameter) variations or even generalizations of the models in [1–3] (Sec. 3.7.2).

3.7.1 New viewpoints on the models used

In [1], the comprehensive analysis that we performed on the system from a macroscopic viewpoint was enabled by the groundbreaking work of E. Ott and T. Antonsen [8, 9]. A detailed comparison of the analysis in [1] (or extensions thereof) with simulations of a finite-size representation of the model in question is worthwhile as it allows to look at types of synchronization and not just the level of coherence as in the OA-reduced system. In such an analysis of the

finite system, not only macroscopic, but also mesoscopic or even microscopic viewpoints can be adopted. In the OA-reduced system, we "only" knew the level of coherence and the firing rate of a population. In the finite reprentation, we may ask whether weak synchronization, frequency-synchronization or drift are exhibited by the populations or even subpopulations thereof. Note carefully that each of these three types can a priori produce very different firing rates and levels of coherence. Drifting oscillators can produce states of high coherence if the oscillators slow down in a certain area of the unit circle so that at any given time, the oscillators are more crowded in this area compared to the rest of the unit circle. Frequency-synchronized oscillators can contribute any (constant) value of the order parameter $r \in [0, 1]$. Also, frequency-synchronized oscillators can have a zero, low or high dynamical frequency[2], contributing differently to the firing rate. This is similarly true of weak synchronization. The phase dynamics of the Theta neuron model (2.1a) puts certain constraints on how the different types of synchronization may unfold, and thus it would be interesting how groups of drifting or weakly/frequency- synchronized oscillators manifest in the populations, and how this depends on whether the populations are quiescent or spiking. Finally, one could try to reproduce the macroscopic oscillations seen in the $N \to \infty$ system with large but finite systems.

In [2], a potent mathematical statement was made regarding the classical macroscopic problem in the Kuramoto model, namely the coherence transition, for a stochastic version of the Kuramoto model with abstract (i.e., generalized) coupling. However, certain graphs fail to make this clear transition at the critical coupling strength that we offer an exact formula for. Here it would be interesting to know in what exact form this transition actually does occur, i.e., how the first oscillators clump together and what different graph-theoretical properties the "early"-synchronizing vertices vs. the "late"-synchronizing vertices have, "early/late" both time-wise and coupling strength-wise.

In [3], the work was for the most part limited to microscopic questions. Even though the last section in this article offers a mesoscopic viewpoint with $N = 50$, we have barely touched the surface. Oscillators drift as soon as they are sufficiently nonidentical, and the coupling weights oscillate accordingly, but what is the exact nature of these oscillations, are they periodic, quasiperiodic, chaotic? Our numerical simulations have shown that the order parameter can exhibit different higher-order periodic waveforms or aperiodic oscillations (not shown in the article). As a first step, one could determine a parameter boundary between periodic and non-periodic motion, similar to what was done for $N = 2$ oscillators for some fixed values of the adaptivity parameter, the Sakaguchi phase lag and the adaptation shift. Certainly, macroscopic questions are difficult

[2] keep in mind that the Theta neuron model, unlike the Kuramoto model, does not have a rotational invariance like (1.3), so one cannot wlog. set the frequency of a group of frequency-synchronized oscillators to zero.

and computationally expensive to answer if the adaptive model continues to be formulated at the individual oscillator level. A reduction technique would be desirable to treat oscillator dynamics with adaptive coupling with macroscopic systems of few differential equations. Thus, one might hope that the works of [11, 12] can be extended towards adaptive graphop models.

3.7.2 Variations of the models used

For the Theta neuron system, one could in future studies break the symmetry in the intra- and inter-population coupling and/or increase the number of populations and study how the dynamical behaviour complicates. One might expect even richer dynamics than exhibited already by the highly symmetric system. An important, difficult question would be how the number of observable spiking/quiescence (or, equivalently, low/high coherence) configurations depends on the number of populations.

For the stochastic Kuramoto model, one could extend our numerical experiments to graphs with two (or more) populations and measure the (local) order parameter(s) versus the inter-population coupling or the sizes of the populations. In [2], we alluded to a boundary between graphs that folllow our theoretical value of $C^\natural$ well and graphs for which this prediction breaks down. Such a boundary is hard to determine exactly, but where might this boundary lie roughly in the landscape of multi-population graphs, where population-specific order parameters might behave differently from the global order parameter? As our theoretical result in [2] pertains to general even 2π-periodic coupling functions (linear combinations of sines with frequencies $\in 2\pi\mathbb{N}$), one should study those as well, as they can add realism to the model [11]. The Kuramoto-Sakaguchi coupling function (a shifted sine) is however not covered by our result. An extension of our theoretical analysis to such coupling functions would be necessary to observe chimera states [82, 83]. One would then of course need to study a more complicated bifurcation scenario than the coherence transition we regarded. Finally, we regarded identical oscillators in [2], but extending our work to nonidentical oscillators would be beneficial, as it would provide comparability with [7, 49, 84]. Moreover, the interplay of the two random effects of random intrinsic frequencies and Brownian motion causes effects worth studying [85].

In the adaptive Kuramoto model, one could investigate how many different combinations of population sizes exist (in stationary states) for a given N. Moreover, one could ask whether states with more than two populations are possible. [52, 53], using a similar model as we do in [3], report states with more than two populations with "hierarchical" combinations of population sizes, where each population rotates with a different frequency. However, they exclusively

use identical oscillators while we use nonidentical oscillators, we offset our coupling weights and vary their amount of adaptivity. Do the differences in the intrinsic frequencies prevent states with more than two populations? Can additional populations be created by choosing non-zero Sakaguchi phase lags and/or adaptation shifts or do we need to individualize these parameters to pairs of (predefined) populations? And what types of synchronization are found within the populations?

E. Ott and T. Antonsen hypothesized [8] that macroscopic chaos would be seen in a system of two populations of Kuramoto oscillators, this was confirmed in [86]. In the same article it was demonstrated that chaos can occur in the Kuramoto-Sakaguchi model with two populations of identical oscillators for N ranging from 4 (two oscillators per population) to medium to large sizes. They posed the question whether chaos would be seen for finitely many nonidentical oscillators too – we saw chaos in [3] for two nonidentical adaptively coupled Kuramoto-Sakaguchi oscillators. Future research could further specify the conditions for chaos in systems of nonidentical oscillators, also investigating how the levels of coherence of populations depend on parameters.

Finally, adaptive graphs in [3] have so far been restricted to either the directed or the undirected regime. Future studies might investigate adaptive models where the graph can dynamically change between directed and undirected.

3.8 Concluding remark

In this thesis, we have given a brief overview of the exciting field of (adaptively) coupled oscillators, as well as a summary, comparison and discussion of our own studies on this topic [1–3]. The goal of this research was to shed light on the synchronization of oscillators coupled via graphs with various properties, i.e. sparse and dense, regular and irregular, constant and adaptive, directed and undirected. We managed to uncover some interesting bifurcation scenarios that provide nontrivial dynamics along a model's path from incoherence to phase-synchronization. In our work, the most complex dynamical behaviour occurred when the graph was directed and adaptive. It can be hypothesized that these two properties of a graph are crucial to explaining complex dynamical phenomena in various contexts.

Appendix A

Characteristic field v of the classical Kuramoto model

$$\frac{\mathrm{d}\phi_l}{\mathrm{d}t} = \omega_l + \frac{C}{N}\sum_{m=1}^{N}\sin(\phi_m - \phi_l) \tag{A.1}$$

$$= \omega_l + \frac{C}{N}\sum_{m=1}^{N}\mathrm{Im}\exp\left(\mathrm{i}(\phi_m - \phi_l)\right) \tag{A.2}$$

$$= \omega_l + \frac{C}{N}\mathrm{Im}\sum_{m=1}^{N}\exp\left(\mathrm{i}(\phi_m - \phi_l)\right) \tag{A.3}$$

$$= \omega_l + \frac{C}{N}\mathrm{Im}\sum_{m=1}^{N}\mathrm{e}^{\mathrm{i}\phi_m}\mathrm{e}^{-\mathrm{i}\phi_l} \tag{A.4}$$

$$= \omega_l + \mathrm{Im}\left(C\mathrm{e}^{-\mathrm{i}\phi_l}\frac{1}{N}\sum_{m=1}^{N}\mathrm{e}^{\mathrm{i}\phi_m}\right) \tag{A.5}$$

$$= \omega_l + \mathrm{Im}\left(C\mathrm{e}^{-\mathrm{i}\phi_l}z\right). \tag{A.6}$$

This carries over to the $N \to \infty$ limit:

$$v(t,\phi,\omega) = \omega + \mathrm{Im}\left(C\mathrm{e}^{-\mathrm{i}\phi}z(t)\right). \tag{A.7}$$

Applying (1.3a), we can set $\psi = 0$ in the Kuramoto model, so $z = r$. Thus, (A.6) becomes

$$\begin{aligned}\frac{\mathrm{d}\phi_l}{\mathrm{d}t} &= \omega_l + \mathrm{Im}\left(Cr\mathrm{e}^{-\mathrm{i}\phi_l}\right) \\ &= \omega_l - Cr\sin\phi_l \end{aligned} \tag{A.8}$$

This carries over to the $N \to \infty$ limit too:

$$v(t,\phi,\omega) = \omega - Cr(t)\sin\phi \tag{A.9}$$

To eliminate $z(t)$ from (A.7), we assume the law of large numbers which allows us to write z in the limit $N \to \infty$:

$$z(t) \equiv r(t)\mathrm{e}^{\mathrm{i}\psi(t)} = \int_{\mathbb{T}}\int_{\mathbb{R}} \mathrm{e}^{\mathrm{i}\phi'}\rho(t,\phi',\omega)\mathrm{d}\omega\mathrm{d}\phi'. \tag{A.10}$$

We now multiply both sides by $\mathrm{e}^{-\mathrm{i}\phi}$

$$r(t)\mathrm{e}^{\mathrm{i}\psi(t)-\mathrm{i}\phi} = \int_{\mathbb{T}}\int_{\mathbb{R}} \mathrm{e}^{\mathrm{i}(\phi'-\phi)}\rho(t,\phi',\omega)\mathrm{d}\omega\mathrm{d}\phi' \tag{A.11}$$

and take the imaginary part on both sides:

$$\begin{aligned}&\mathrm{Im}\left[\underbrace{r(t)\mathrm{e}^{\mathrm{i}\psi(t)-\mathrm{i}\phi}}_{\mathrm{e}^{-\mathrm{i}\phi}z(t)}\right] = \mathrm{Im}\left[\int_{\mathbb{T}}\int_{\mathbb{R}} \mathrm{e}^{\mathrm{i}(\phi'-\phi)}\rho(t,\phi',\omega)\mathrm{d}\omega\mathrm{d}\phi'\right] \\ &= r(t)\sin(\psi(t)-\phi) = \int_{\mathbb{T}}\int_{\mathbb{R}} \sin(\phi'-\phi)\rho(t,\phi',\omega)\mathrm{d}\omega\mathrm{d}\phi'. \end{aligned} \tag{A.12}$$

Now inserting (A.12) into (A.7), we get the characteristic field v in the $N \to \infty$ limit:

$$v(t,\phi,\omega) = \omega + C\int_{\mathbb{T}}\int_{\mathbb{R}} \sin(\phi'-\phi)\rho(t,\phi',\omega')\mathrm{d}\omega'\mathrm{d}\phi'. \tag{A.13}$$

Note that this resembles (A.1), except that the density ρ must be taken into account as well. Recalling that we can set $\psi = 0$ in the Kuramoto model, (A.12) helps to reassure ourselves that the rhs. of (A.9) and (A.13) are actually equal. Moreover, rememberig that $\rho(t,\phi,\omega) \equiv g(\omega)\rho(t,\phi|\omega)$, we can write (A.13) as

$$v(t,\phi,\omega) = \omega + C\int_{\mathbb{T}}\int_{\mathbb{R}} \sin(\phi'-\phi)\rho(t,\phi'|\omega')g(\omega')\mathrm{d}\omega'\mathrm{d}\phi'. \tag{A.14}$$

Bibliography

[1] Benjamin Jüttner, Christian Henriksen, and Erik A Martens. Birth and destruction of collective oscillations in a network of two populations of coupled type 1 neurons. *Chaos: An Interdisciplinary Journal of Nonlinear Science*, 31(2):023141, 2021.

[2] Marios Antonios Gkogkas, Benjamin Jüttner, Christian Kuehn, and Erik Andreas Martens. Graphop Mean-Field Limits and Synchronization for the Stochastic Kuramoto Model. *arXiv preprint arXiv:2203.16839*, 2022.

[3] Benjamin Jüttner and Erik A Martens. Complex dynamics in adaptive phase oscillator networks. *unsubmitted manuscript*, 2022.

[4] M. Nijhoff. Œuvres complètes de Christiaan Huygens: L'horloge à pendule de 1651 à 1666. Travaux divers de physique, de mécanique et de technique de 1650 à 1666. Traité des couronnes et des parhélies (1662 ou 1663). *Swets & Zeitlinger Publishers, Amsterdam*, 17, 1967.

[5] Norbert Wiener. *Nonlinear problems in random theory.* 1966.

[6] Arthur T Winfree. Biological rhythms and the behavior of populations of coupled oscillators. *Journal of theoretical biology*, 16(1):15–42, 1967.

[7] Georg A Gottwald. Finite-size effects in a stochastic Kuramoto model. *Chaos: An Interdisciplinary Journal of Nonlinear Science*, 27(10):101103, 2017.

[8] Edward Ott and Thomas M Antonsen. Low dimensional behavior of large systems of globally coupled oscillators. *Chaos: An Interdisciplinary Journal of Nonlinear Science*, 18(3):037113, 2008.

[9] Edward Ott and Thomas M Antonsen. Long time evolution of phase oscillator systems. *Chaos: An interdisciplinary journal of nonlinear science*, 19(2):023117, 2009.

[10] S. Watanabe and S. H. Strogatz. Constants of motion for superconducting Josephson arrays. *Physica D*, 74(3-4):197–253, 1994.

[11] Christian Kuehn. Network dynamics on graphops. *New Journal of Physics*, 22(5):053030, 2020.

[12] Marios Antonios Gkogkas and Christian Kuehn. Graphop mean-field limits for Kuramoto-type models. *SIAM Journal on Applied Dynamical Systems*, 21(1):248–283, 2022.

[13] Erik A Martens. Chimeras in a network of three oscillator populations with varying network topology. *Chaos: An Interdisciplinary Journal of Nonlinear Science*, 20(4):043122, 2010.

[14] E. A. Martens, C. Bick, and M. J. Panaggio. Chimera states in two populations with heterogeneous phase-lag. *Chaos*, 26(9):094819, 2016.

[15] Erik Andreas Martens, Shashi Thutupalli, Antoine Fourriere, and Oskar Hallatschek. Chimera states in mechanical oscillator networks. *Proceedings of the National Academy of Sciences*, 110(26):10563–10567, 2013.

[16] Francisco A Rodrigues, Thomas K DM Peron, Peng Ji, and Jürgen Kurths. The Kuramoto model in complex networks. *Physics Reports*, 610:1–98, 2016.

[17] John Adrian Bondy, Uppaluri Siva Ramachandra Murty, et al. *Graph theory with applications*, volume 290. Macmillan London, 1976.

[18] Steven H Strogatz. *Nonlinear dynamics and chaos: with applications to physics, biology, chemistry, and engineering*. CRC press, 2018.

[19] Lawrence Perko. *Differential equations and dynamical systems*, volume 7. Springer Science & Business Media, 2013.

[20] Yuri A Kuznetsov, Iu A Kuznetsov, and Y Kuznetsov. *Elements of applied bifurcation theory*, volume 112. Springer, 1998.

[21] Yoshiki Kuramoto. Self-entrainment of a population of coupled non-linear oscillators. In *International symposium on mathematical problems in theoretical physics*, pages 420–422. Springer, 1975.

[22] Hidetsugu Sakaguchi and Yoshiki Kuramoto. A soluble active rotater model showing phase transitions via mutual entertainment. *Progress of Theoretical Physics*, 76(3):576–581, 1986.

[23] E Omel'Chenko and Matthias Wolfrum. Nonuniversal transitions to synchrony in the Sakaguchi-Kuramoto model. *Physical review letters*, 109(16):164101, 2012.

[24] E Omel'chenko and Matthias Wolfrum. Bifurcations in the Sakaguchi–Kuramoto model. *Physica D: Nonlinear Phenomena*, 263:74–85, 2013.

[25] Duncan J Watts and Steven H Strogatz. Collective dynamics of 'small-world' networks. *nature*, 393(6684):440–442, 1998.

[26] Daniel A Wiley, Steven H Strogatz, and Michelle Girvan. The size of the sync basin. *Chaos: An Interdisciplinary Journal of Nonlinear Science*, 16(1):015103, 2006.

[27] Hyunsuk Hong, Moo-Young Choi, and Beom Jun Kim. Synchronization on small-world networks. *Physical Review E*, 65(2):026139, 2002.

[28] Cesar A Hidalgo and Albert-Laszlo Barabasi. Scale-free networks. *Scholarpedia*, 3(1):1716, 2008.

[29] Yamir Moreno and Amalio F Pacheco. Synchronization of Kuramoto oscillators in scale-free networks. *EPL (Europhysics Letters)*, 68(4):603, 2004.

[30] S Yoon, M Sorbaro Sindaci, AV Goltsev, and JFF Mendes. Critical behavior of the relaxation rate, the susceptibility, and a pair correlation function in the Kuramoto model on scale-free networks. *Physical Review E*, 91(3):032814, 2015.

[31] Thomas Peron, Bruno Messias F de Resende, Angélica S Mata, Francisco A Rodrigues, and Yamir Moreno. Onset of synchronization of Kuramoto oscillators in scale-free networks. *Physical Review E*, 100(4):042302, 2019.

[32] Mark Verwoerd and Oliver Mason. On computing the critical coupling coefficient for the Kuramoto model on a complete bipartite graph. *SIAM Journal on Applied Dynamical Systems*, 8(1):417–453, 2009.

[33] Patrick N McGraw and Michael Menzinger. Clustering and the synchronization of oscillator networks. *Physical Review E*, 72(1):015101, 2005.

[34] Patrick N McGraw and Michael Menzinger. Analysis of nonlinear synchronization dynamics of oscillator networks by Laplacian spectral methods. *Physical Review E*, 75(2):027104, 2007.

[35] Patrick N McGraw and Michael Menzinger. Laplacian spectra as a diagnostic tool for network structure and dynamics. *Physical Review E*, 77(3):031102, 2008.

[36] Mark EJ Newman. Random graphs with clustering. *Physical review letters*, 103(5):058701, 2009.

[37] Joel C Miller. Percolation and epidemics in random clustered networks. *Physical Review E*, 80(2):020901, 2009.

[38] Brian Karrer and Mark EJ Newman. Random graphs containing arbitrary distributions of subgraphs. *Physical Review E*, 82(6):066118, 2010.

[39] Juan A Acebrón, Luis L Bonilla, Conrad J Pérez Vicente, Félix Ritort, and Renato Spigler. The Kuramoto model: A simple paradigm for synchronization phenomena. *Reviews of modern physics*, 77(1):137, 2005.

[40] Ernest Montbrió, Jürgen Kurths, and Bernd Blasius. Synchronization of two interacting populations of oscillators. *Physical Review E*, 70(5):056125, 2004.

[41] Arkady Pikovsky and Michael Rosenblum. Partially integrable dynamics of hierarchical populations of coupled oscillators. *Physical review letters*, 101(26):264103, 2008.

[42] Ernest Barreto, Brian Hunt, Edward Ott, and Paul So. Synchronization in networks of networks: The onset of coherent collective behavior in systems of interacting populations of heterogeneous oscillators. *Physical Review E*, 77(3):036107, 2008.

[43] Carlo R Laing. Chimera states in heterogeneous networks. *Chaos: An Interdisciplinary Journal of Nonlinear Science*, 19(1):013113, 2009.

[44] Per Sebastian Skardal and Juan G Restrepo. Hierarchical synchrony of phase oscillators in modular networks. *Physical Review E*, 85(1):016208, 2012.

[45] Tommaso Menara, Giacomo Baggio, Danielle S Bassett, and Fabio Pasqualetti. Stability conditions for cluster synchronization in networks of heterogeneous Kuramoto oscillators. *IEEE Transactions on Control of Network Systems*, 7(1):302–314, 2019.

[46] Uffe Høgsbro Thygesen. Lecture Notes on Diffusion and Stochastic Differential Equations. 2016.

[47] Hiroshi Kunita. *Stochastic flows and stochastic differential equations*, volume 24. Cambridge university press, 1997.

[48] Hidetsugu Sakaguchi. Cooperative phenomena in coupled oscillator systems under external fields. *Progress of theoretical physics*, 79(1):39–46, 1988.

[49] Bidhan Chandra Bag, KG Petrosyan, and Chin-Kun Hu. Influence of noise on the synchronization of the stochastic Kuramoto model. *Physical Review E*, 76(5):056210, 2007.

[50] Bernard Sonnenschein and Lutz Schimansky-Geier. Approximate solution to the stochastic Kuramoto model. *Physical Review E*, 88(5):052111, 2013.

[51] Philip Seliger, Stephen C Young, and Lev S Tsimring. Plasticity and learning in a network of coupled phase oscillators. *Physical Review E*, 65(4):041906, 2002.

[52] Rico Berner, Eckehard Scholl, and Serhiy Yanchuk. Multiclusters in networks of adaptively coupled phase oscillators. *SIAM Journal on Applied Dynamical Systems*, 18(4):2227–2266, 2019.

[53] Rico Berner, Jan Fialkowski, Dmitry Kasatkin, Vladimir Nekorkin, Serhiy Yanchuk, and Eckehard Schöll. Hierarchical frequency clusters in adaptive networks of phase oscillators. *Chaos: An Interdisciplinary Journal of Nonlinear Science*, 29(10):103134, 2019.

[54] Rico Berner, Alicja Polanska, Eckehard Schöll, and Serhiy Yanchuk. Solitary states in adaptive nonlocal oscillator networks. *The European Physical Journal Special Topics*, 229(12):2183–2203, 2020.

[55] Rico Berner, Jakub Sawicki, and Eckehard Schöll. Birth and stabilization of phase clusters by multiplexing of adaptive networks. *Physical review letters*, 124(8):088301, 2020.

[56] Rico Berner, Simon Vock, Eckehard Schöll, and Serhiy Yanchuk. Desynchronization transitions in adaptive networks. *Physical Review Letters*, 126(2):028301, 2021.

[57] Thilo Gross and Bernd Blasius. Adaptive coevolutionary networks: a review. *Journal of the Royal Society Interface*, 5(20):259–271, 2008.

[58] Hiroki Sayama, Irene Pestov, Jeffrey Schmidt, Benjamin James Bush, Chun Wong, Junichi Yamanoi, and Thilo Gross. Modeling complex systems with adaptive networks. *Computers & Mathematics with Applications*, 65(10):1645–1664, 2013.

[59] Pablo M Gleiser and Damián H Zanette. Synchronization and structure in an adaptive oscillator network. *The European Physical Journal B-Condensed Matter and Complex Systems*, 53(2):233–238, 2006.

[60] G. B. Ermentrout and N. Kopell. Parabolic Bursting in an excitable system coupled with a slow oscillation. *SIAM Journal on Applied Mathematics*, 46(2):233–253, 1986.

[61] Wulfram Gerstner, Werner M Kistler, Richard Naud, and Liam Paninski. *Neuronal dynamics: From single neurons to networks and models of cognition*. Cambridge University Press, 2014.

[62] Tanushree B Luke, Ernest Barreto, and Paul So. Complete classification of the macroscopic behavior of a heterogeneous network of theta neurons. *Neural computation*, 25(12):3207–3234, 2013.

[63] Paul So, Tanushree B Luke, and Ernest Barreto. Networks of theta neurons with time-varying excitability: Macroscopic chaos, multistability, and final-state uncertainty. *Physica D: Nonlinear Phenomena*, 267:16–26, 2014.

[64] Tanushree B Luke, Ernest Barreto, and Paul So. Macroscopic complexity from an autonomous network of networks of theta neurons. *Frontiers in computational neuroscience*, 8:145, 2014.

[65] Steven H Strogatz. From Kuramoto to Crawford: exploring the onset of synchronization in populations of coupled oscillators. *Physica D: Nonlinear Phenomena*, 143(1-4):1–20, 2000.

[66] Carlo Lancellotti. On the Vlasov limit for systems of nonlinearly coupled oscillators without noise. *Transport theory and statistical physics*, 34(7):523–535, 2005.

[67] András Vasy. *Partial differential equations*, volume 169. American Mathematical Soc., 2015.

[68] Hayato Chiba and Georgi S Medvedev. The mean field analysis for the Kuramoto model on graphs I. The mean field equation and transition point formulas. *arXiv preprint arXiv:1612.06493*, 2016.

[69] Steven H Strogatz and Renato E Mirollo. Stability of incoherence in a population of coupled oscillators. *Journal of Statistical Physics*, 63(3):613–635, 1991.

[70] C. Bick, C. Laing, M. Goodfellow, and E.A. Martens. Understanding the dynamics of biological and neural oscillator networks through exact mean-field reductions: a review. *Journal of Mathematical Neuroscience*, 9(10), 2020.

[71] Christian Borgs, Jennifer Chayes, László Lovász, Vera T Sós, Balázs Szegedy, and Katalin Vesztergombi. Graph limits and parameter testing. In *Proceedings of the thirty-eighth annual ACM symposium on Theory of computing*, pages 261–270, 2006.

[72] Georgi S Medvedev. The nonlinear heat equation on dense graphs and graph limits. *SIAM Journal on Mathematical Analysis*, 46(4):2743–2766, 2014.

[73] Ágnes Backhausz and Balázs Szegedy. Action convergence of operators and graphs. *Canadian Journal of Mathematics*, 74(1):72–121, 2022.

[74] Ole Christensen. *Functions, spaces, and expansions: mathematical tools in physics and engineering*. Springer, 2010.

[75] Erwin Kreyszig. *Introductory functional analysis with applications*, volume 17. John Wiley & Sons, 1991.

[76] Georgi S Medvedev. Small-world networks of Kuramoto oscillators. *Physica D: Nonlinear Phenomena*, 266:13–22, 2014.

[77] Shuang Gao and Peter E Caines. Spectral representations of graphons in very large network systems control. In *2019 IEEE 58th conference on decision and Control (CDC)*, pages 5068–5075. IEEE, 2019.

[78] Ernest Montbrió, Diego Pazó, and Alex Roxin. Macroscopic description for networks of spiking neurons. *Physical Review X*, 5(2):021028, 2015.

[79] J. Guckenheimer and Y. Kuznetsov. Bautin bifurcation. *Scholarpedia*, 2007.

[80] Benjamin Jüttner. Collective behaviour in two populations of coupled Theta neurons. *M.Sc. thesis at the Technical University of Denmark*, 2019.

[81] Dumitru Călugăru, Jan Frederik Totz, Erik A Martens, and Harald Engel. First-order synchronization transition in a large population of strongly coupled relaxation oscillators. *Science advances*, 6(39):eabb2637, 2020.

[82] M. J. Panaggio and D. M. Abrams. Chimera states: coexistence of coherence and incoherence in networks of coupled oscillators. *Nonlinearity*, 28(3):R67, 2015.

[83] Oleksandr Burylko, Erik Andreas Martens, and Christian Bick. Symmetry breaking yields chimeras in two small populations of Kuramoto-type oscillators. *arXiv preprint arXiv:2202.10807*, 2022.

[84] Bernard Sonnenschein and Lutz Schimansky-Geier. Onset of synchronization in complex networks of noisy oscillators. *Physical Review E*, 85(5):051116, 2012.

[85] Eric Luçon and Christophe Poquet. Long time dynamics and disorder-induced traveling waves in the stochastic Kuramoto model. In *Annales de l'Institut Henri Poincaré, Probabilités et Statistiques*, volume 53, pages 1196–1240. Institut Henri Poincaré, 2017.

[86] C. Bick, M. J. Panaggio, and E. A. Martens. Chaos in Kuramoto Oscillator Networks. *Chaos*, 28:071102, 2018.

Article [1] – Birth and destruction of collective oscillations in a network of two populations of coupled type 1 neurons

---

Reproduced from Chaos 31, 023141 (2021); https://doi.org/10.1063/5.0031630, with the permission of AIP Publishing.

Article [1], entitled *Birth and destruction of collective oscillations in a network of two populations of coupled type 1 neurons*, was written as a product of the Special Course "Network Dynamics and Synchronization Theory" led by Erik A. Martens and undertaken in the first year of the PhD studies. The manuscript was submitted to the journal *Chaos* (AIP publishing) the 2^{nd} of October 2020, accepted the 12^{th} of January 2021 and published the 24^{th} of February 2021. The published article is here attached with permission of *Chaos* (AIP publishing).

The authors of this article are: Benjamin Jüttner, Christian Henriksen, and Erik A. Martens.

Chaos ARTICLE scitation.org/journal/cha

Birth and destruction of collective oscillations in a network of two populations of coupled type 1 neurons

Cite as: Chaos **31**, 023141 (2021); doi: 10.1063/5.0031630
Submitted: 2 October 2020 · Accepted: 12 January 2021 ·
Published Online: 24 February 2021

Benjamin Jüttner,[1] Christian Henriksen,[1] and Erik A. Martens[1,2,3,a)]

AFFILIATIONS

[1]Department of Applied Mathematics and Computer Science, Technical University of Denmark, 2800 Kgs. Lyngby, Denmark
[2]Department of Biomedical Sciences, University of Copenhagen, Blegdamsvej 3, 2200 Copenhagen, Denmark
[3]Center for Translational Neurosciences, University of Copenhagen, Blegdamsvej 3, 2200 Copenhagen, Denmark

[a)]**Author to whom correspondence should be addressed:** eama@dtu.dk

ABSTRACT

We study the macroscopic dynamics of large networks of excitable type 1 neurons composed of two populations interacting with disparate but symmetric intra- and inter-population coupling strengths. This nonuniform coupling scheme facilitates symmetric equilibria, where both populations display identical firing activity, characterized by either quiescent or spiking behavior, or asymmetric equilibria, where the firing activity of one population exhibits quiescent but the other exhibits spiking behavior. Oscillations in the firing rate are possible if neurons emit pulses with non-zero width but are otherwise quenched. Here, we explore how collective oscillations emerge for two statistically identical neuron populations in the limit of an infinite number of neurons. A detailed analysis reveals how collective oscillations are born and destroyed in various bifurcation scenarios and how they are organized around higher codimension bifurcation points. Since both symmetric and asymmetric equilibria display bistable behavior, a large configuration space with steady and oscillatory behavior is available. Switching between configurations of neural activity is relevant in functional processes such as working memory and the onset of collective oscillations in motor control.

The theta neuron model[1] is the normal form for the saddle-node-on-invariant cycle bifurcation; i.e., it represents the dynamic behavior near the excitation threshold of type 1 neurons, and it is equivalent to the quadratic integrate-and-fire neuron.[2–4] These neuron models have attracted much interest based on recently developed dimensional reduction techniques,[5,6] allowing for an exact description of neuron ensembles in terms of macroscopic collective variables;[6,7] for reviews, see also Refs. 8 and 9. Such neuron populations mimic densely connected neural masses in the brain. Collective oscillations arising in the brain are important for generating rhythms in the brain, e.g., for motor control[10] and breathing.[11] The combination of excitatory and inhibitory neurons is a known prerequisite for the generation of collective rhythms such as gamma rhythms.[12] In this study, we pursue the mathematical question of how collective rhythms may arise in an even simpler model composed of two populations of (statistically) identical excitatory neurons with nonuniform coupling and what their bifurcations are.

I. INTRODUCTION

The brain is a complex network of networks with a hierarchical structure,[13,14] thus organizing neurons into neural masses, communities with high connectivity, structures that may interact with one another[14,15] to solve cognitive functions[16] by displaying different individual collective dynamic behaviors. A prominent collective behavior observed in the brain occurs when a group of neurons synchronizes and oscillates in unison.[17,18] Synchrony has been associated with solving functional tasks including memory,[19] computational functions,[20] cognition,[21] attention,[20,22] processing and routing of information,[23–26] control of gait and motion,[10] or breathing.[11]

Neural masses with densely connected neurons are interconnected and form networks of a modular structure. An important functional aspect in such networks is situations under which each population may assume different collective dynamic behaviors, such as low or high synchrony or low and high firing activity. Thus, a network of oscillator populations may exhibit a large configuration space with different synchronization patterns, as is

also exemplified by chimera states in Kuramoto oscillator networks, where one or several populations are synchronized and the other desynchronized.[26–34] The dynamics of such networks with a multi-population structure and their configurations has been explored in the context of neuroscience,[7,35,36] including memory recall,[37] information processing via self-induced stochastic resonance,[38] and deep brain stimulation.[39]

Many studies concern the modeling of neuronal processes at the microscopic scale of individual neurons. However, the number of neurons in the brain is enormous, and, consequently, mathematical models of the brain are very high dimensional so that analyzing the collective dynamic behavior of large neuronal assemblies poses a prohibitive challenge; a coarse-grained description of the dynamics at the macroscopic level is desirable. Recently developed mathematical methods based on the Ott–Antonsen[3] and Watanabe–Strogatz reductions[40,41] allow for an exact dimensional reduction, which applies to phase oscillator networks with sinusoidal coupling, including variants of the Kuramoto model, the theta neuron model, and the equivalent quadratic integrate-and-fire neuron model. Unlike heuristic models,[42,43] the resulting model equations exactly describe the collective dynamics for each population and—connecting the microscopic to the macroscopic description—accurately capture microscopic properties of the underlying system.[8,9,44]

Collective oscillations in neural activity occurs over a broad range of frequencies and across many brain regions.[45] Prominent are gamma frequency oscillations relevant in connection with cognitive tasks,[46] neuronal diseases,[18] motor control,[10] and breathing.[11] Such collective oscillations are known to occur in neuron networks with excitatory and inhibitory coupling.[44,47–49] Network models with (statistically) identical neurons emitting infinitely "sharp" signal pulses as represented by Dirac distributions do not permit collective oscillations;[50] conversely, collective oscillatory behavior is possible when the pulse width is non-zero.[7,51]

We study a network composed of two populations of inhibitory type 1 neurons with non-uniform (but symmetric) coupling, interacting through pulses with non-zero width. We consider the dynamics in the continuum limit of infinitely many neurons, allowing us to use aforementioned dimensional reduction methods.[3,8] Rather than aiming at a high level of biophysical realism, we wish to elucidate how collective oscillations may get born and destroyed in a simple setup and to explore their related bifurcation scenarios. Even though the coupling is symmetric and neurons are statistically identical, the resulting dynamic behavior is surprisingly complicated. The neuronal activity in each population may assume distinct levels, thus resulting in multistable configurations, in similarity to synchronization patterns as those observed in chimera states[27,34] or (non-oscillatory) neural states reported for models of working memory.[37] In particular, one observes a rich structure of bifurcations producing collective limit cycle oscillations for which we provide a detailed bifurcation analysis.

This article is structured as follows. In Sec. II, we introduce our model of two populations of theta neurons and its equivalent form of quadratic integrate-and-fire neurons. We outline how an exact description of the macroscopic dynamics for populations of infinitely many neurons is obtained via the Ott–Antonsen method, and how firing rate equations for the equivalent QIF neurons are derived via a conformal mapping.[6] In Sec. III, we summarize the known dynamical behavior for a single population, which represents a limiting case for two populations with vanishing inter-population coupling or uniform coupling. In Sec. IV, we perform a detailed analysis by using numerical continuation methods via MatCont[52] and explain the various bifurcation scenarios that are possible. Finally, we sum our findings up and conclude with a discussion in Sec. V.

II. MODEL

A. Network of theta neurons

We consider a model of $M = 2$ populations of N interacting theta neurons, where the phase $\theta_{\sigma,k} \in \mathbb{T} := \mathbb{R}/2\pi\mathbb{Z}$ of the kth neuron belonging to population $\sigma = 1, 2$ evolves according to

$$\dot{\theta}_{\sigma,k} := \frac{\mathrm{d}\theta_{\sigma,k}}{\mathrm{d}t} = 1 - \cos\theta_{\sigma,k} + (1 + \cos\theta_{\sigma,k})(\eta_{\sigma,k} + I_\sigma), \quad (1)$$

with excitability $\eta_{\sigma,k}$ of oscillator k in population σ sampled from a Lorentzian distribution $g_\sigma(\eta)$ with mode $\hat{\eta}_\sigma$ and width Δ_σ. The theta neuron (1) is the normal form of the saddle-node-on-invariant-circle (SNIC) (or saddle-node-infinite period) bifurcation[53] and is a canonical type 1 neuron.[1] The dynamics are as follows. For $\eta_{\sigma,k} + I_\sigma < 0$, a stable and unstable fixed point occurs on the phase circle $\mathbb{T}$; for $\eta_{\sigma,k} + I_\sigma = 0$, these fixed points coalesce in a saddle-node bifurcation; for $\eta_{\sigma,k} + I_\sigma > 0$, the flow on the circle results in a cyclic/periodic motion. If $\eta_{\sigma,k} + I_\sigma < 0$, the theta neuron is said to be *excitable*: in the absence of perturbations, the phase relaxes to the stable fixed point on the phase circle $\mathbb{T}$; however, a perturbation may lead to a single spike (at $\theta_{\sigma,k} = \pi$) before returning to the stable fixed point. This could happen in at least two ways: a perturbation of the phase across the unstable fixed point (constituting a threshold) is possible if one considers that the theta model derives from a higher dimensional model[1] so that the circle is embedded in a higher dimensional space; alternatively, a very short-lived (time scale of a single cycle) increase in I_σ momentarily pushes the system across the bifurcation threshold $\eta_{\sigma,k} + I_\sigma = 0$. If $\eta_{\sigma,k} + I_\sigma > 0$, the neuron is *firing* (or excited); i.e., it spikes periodically.

The input current may result from a variety of interactions; for an overview, see Refs. 8 and 50. Here, we assume that the input current is given by

$$I_\sigma = \sum_{\tau=1}^{M} \frac{\kappa_{\sigma\tau}}{N} \sum_{l=1}^{N} P_s(\theta_{\tau,l}), \quad (2)$$

where adjacent neurons interact via pulses, which we choose to be

$$P_s(\theta) = a_s(1 - \cos\theta)^s, \quad (3)$$

originally adopted by Ariaratnam and Strogatz,[54] with shape parameter $s \in \mathbb{N}$, see also Fig. 1, and coupling strengths $\kappa_{\sigma\tau}$ between populations σ and τ. The normalization constant $a_s = 2^s(s!)^2/(2s)!$ is defined so that $\int_0^{2\pi} P_s(\theta)\, d\theta = 2\pi$.

The case of $M = 2$ populations results in eight parameters (excluding the pulse shape parameter s). To reduce the problem to a manageable number of parameters, we make the following assumptions: (i) the oscillator properties in populations $\sigma = 1, 2$ are statistically identical so that $\hat{\eta}_1 = \hat{\eta}_2 =: \hat{\eta}$ and $\Delta_1 = \Delta_2 =: \Delta$ and

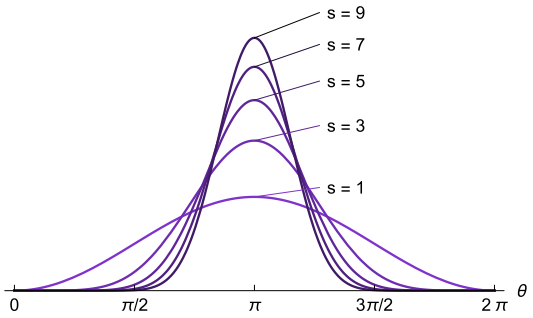

FIG. 1. Pulse shape for varying pulse shape parameter s. The pulse converges to Dirac delta as $s \to \infty$.

(ii) the coupling is symmetric with respect to identical intra- and inter-coupling strengths, i.e., $\kappa_{11} = \kappa_{22} =: \kappa$. and $\kappa_{12} = \kappa_{21} =: a\kappa$. Unless stated otherwise, we keep $(\hat{\eta}, \Delta, s)$ fixed and consider (κ, a) the main bifurcation parameters.

B. Network of quadratic integrate-and-fire neurons

An equivalent description of the theta neuron is the quadratic integrate-and-fire (QIF) neuron via the transformation into the membrane potential $V(\theta) = \tan(\theta/2) \in (-\infty, \infty)$. The model equations then become[8]

$$\frac{\mathrm{d}}{\mathrm{d}t} V_{\sigma,k} := \dot{V}_{\sigma,k} = V_{\sigma,k}^2 + \eta_{\sigma,k} + I_\sigma, \tag{4}$$

where $V_{\sigma,k} := V(\theta_{\sigma,k})$. In this formulation, the neuron fires (emits a spike) when the voltage reaches $V_k(t^-) = \infty$ (in finite time). It is then reset to $V_k(t^+) = -\infty$. QIF neurons have been widely used in neuroscientific modeling; see Refs. 4 and 55 for a general introduction and Refs. 3 and 56 for a few examples of applications of QIF neurons.

C. Exact macroscopic description for the limit of infinitely many neurons

We consider (1) in the limit $N \to \infty$, which allows us to express the ensemble dynamics in terms of a continuous neuron density $\rho_\sigma(\theta, \eta, t)$ governed by the continuity equation

$$\frac{\partial}{\partial t}\rho_\sigma + \frac{\partial}{\partial \theta}(f_\sigma \rho_\sigma) = 0, \tag{5}$$

where

$$f_\sigma = 1 - \cos\theta + (1 + \cos\theta) \times \left(\eta + \sum_{\tau=1}^{M} \kappa_{\sigma\tau} \int_{-\infty}^{\infty}\int_0^{2\pi} P_s(\theta')\rho_\tau(\eta', \theta', t)\,\mathrm{d}\theta'\,\mathrm{d}\eta'\right) \tag{6}$$

The Ott–Antonsen method[5,7] facilitates an exact reduction of the microscopic dynamics in (1) to a low-dimensional description of the macroscopic dynamics in terms of the complex order parameter of each population,

$$Z_\sigma(t) = R_\sigma(t)\, e^{-i\Phi_\sigma(t)} = \int_0^{2\pi}\int_{-\infty}^{\infty} e^{i\theta}\rho_\sigma(\theta, \eta, t)\,\mathrm{d}\eta\,\mathrm{d}\theta. \tag{7}$$

The absolute value of the order parameter informs us of the level of phase synchronization of the neuron population: when $|Z_\sigma| \approx 0$, phases are spread over the circle $\mathbb{T}$, whereas $|Z_\sigma| \approx 1$ implies phase synchronization; i.e., phases are closely spread around the phase of the order parameter given by $\Phi_\sigma = -\arg(Z_\sigma)$. The collective dynamics of population $\sigma = 1, 2$ is then given by[7,8]

$$\dot{Z}_\sigma = -\frac{1}{2}\left[(\Delta_\sigma - i\hat{\eta}_\sigma - iI_\sigma^{(s)})(1 + Z_\sigma)^2 + i(1 - Z_\sigma)^2\right]. \tag{8}$$

These equations are closed by the input current[7,8]

$$I_\sigma^{(s)} = \sum_{\tau=1}^{M} \kappa_{\sigma\tau} P_\sigma^{(s)}, \tag{9}$$

with the average output from all other neurons in the network,

$$P_\sigma^{(s)} = a_s\left(C_0 + \sum_{q=1}^{s} C_q(Z_\sigma^q + \bar{Z}_\sigma^q)\right), \tag{10}$$

$$C_q = \sum_{k=0}^{s}\sum_{m=0}^{k} \frac{s!(-1)^k \delta_{k-2m,q}}{2^k m!(s-k)!(k-m)!}. \tag{11}$$

For details on this reduction method and theory in general including applications in neuroscience, see Ref. 8.

Two cases are of particular interest to us: pulse shape parameter $s = 1$ and $s = \infty$ (impulsive coupling) for which we have

$$P_\sigma^{(1)} = 1 - \frac{1}{2}(Z_\sigma + \bar{Z}_\sigma) \tag{12}$$

and

$$P_\sigma^{(\infty)} = \frac{1 - |Z_\sigma|^2}{(1 + Z_\sigma)(1 + \bar{Z}_\sigma)}, \tag{13}$$

respectively.

D. Firing rate equations

The model (8) has an equivalent formulation in terms of average firing rate r_σ and average membrane potential v_σ called the Firing Rate Equations (FREs).[6] Indeed, changing variables via the (anti)conformal mapping

$$Z = (1 - \bar{W})/(1 + \bar{W}) \quad \text{or } W = (1 - \bar{Z})/(1 + \bar{Z}), \tag{14}$$

gives

$$\dot{W}_\sigma = \Delta_\sigma + i\hat{\eta}_\sigma - iW_\sigma^2 + iI_\sigma^{(s)} \tag{15}$$

and

$$P_\sigma^{(1)} = 1 - \frac{1 - |W_\sigma|^2}{(1 + W_\sigma)(1 + \bar{W}_\sigma)}, \tag{16}$$

$$P_\sigma^{(\infty)} = \frac{1}{2}(W_\sigma + \bar{W}_\sigma). \tag{17}$$

Writing $W_\sigma = \pi r_\sigma + i v_\sigma$, (16) and (17) take the form

$$P_\sigma^{(1)} = 2\frac{\pi^2 r_\sigma^2 + \pi r_\sigma + v_\sigma^2}{(\pi r_\sigma + 1)^2 + v_\sigma^2}, \quad P_\sigma^{(\infty)} = \pi r_\sigma, \tag{18}$$

for $s = 1$ and $s = \infty$, respectively. Taking the real and imaginary part of (15) yields the firing rate equations

$$\dot{r}_\sigma = \frac{\Delta_\sigma}{\pi} + 2 r_\sigma v_\sigma, \tag{19}$$

$$\dot{v}_\sigma = v_\sigma^2 - \pi^2 r_\sigma^2 + \hat{\eta}_\sigma + I_\sigma^{(s)}, \tag{20}$$

where

$$I_\sigma^{(s)} = \begin{cases} 2\sum_{\tau=1}^{M} \kappa_{\sigma\tau} \dfrac{\pi r_\tau^2 + \pi r_\tau + v_\tau^2}{(\pi r_\tau + 1)^2 + v_\tau^2}, & s = 1, \\ \pi \sum_{\tau=1}^{M} \kappa_{\sigma\tau} r_\tau, & s = \infty. \end{cases} \tag{21}$$

The microscopic and macroscopic description is related as follows. A single theta neuron fires when its phase crosses $\theta = \pi$; accordingly, the average firing rate $r_\sigma(t)$ of the network at time t is defined as the flux through $\theta = \pi$ (or equivalently, the flux at $v_\sigma = \infty$), see, for instance, Ref. 8.

III. DYNAMIC BEHAVIOR OF ONE POPULATION

The dynamic behavior for the case of $M = 1$ population has already been studied previously.[7,51] We briefly review the dynamics observed for this case as it is instructive for understanding the dynamic and oscillatory behavior exhibited by $M = 2$ populations. For two-parameter choices, the model equation (1) for $M = 2$ effectively reduce to the dynamics of a single population, $M = 1$. Recall that the intra- and inter-coupling strengths among the two populations are given via $\kappa_{11} = \kappa_{22} = \kappa$ and $\kappa_{12} = \kappa_{21} = \kappa a$. Thus, when $a = 1$, all neurons experience identical coupling strength so that the two populations act like a single population consisting of twice the number of neurons; on the other hand, when $a = 0$, the two populations are decoupled so that each of the two populations in separation effectively corresponds to a $M = 1$ system. For brevity, we drop σ in (1) and all related equations.

The bifurcation diagrams in Fig. 2 report minima and maxima for the firing rate r while varying coupling strength κ with parameter values $s = 1$, $\Delta = 0.01$ fixed, and $\hat{\eta} = -0.5$ or $\hat{\eta} = 0.5$ in panels (a) and (b), respectively. Solution branches sometimes appear very close to each other for the firing rate r; therefore, it is instructive to also report the magnitude of the order parameter, $|Z|$, which is related to the firing rate r via the (anti)conformal mapping (14). Equilibria and local bifurcations (saddle-node, Hopf) can be computed analytically from (19) and (20); limit cycles and other bifurcations were computed and continued numerically using Matlab and MatCont software;[52] see also Appendix B.

We first consider the case of excitable neurons ($\hat{\eta} < 0$) in Fig. 2(a). For the parameters considered and $\kappa \lessapprox 0$, we observe a set of stable equilibria (stable nodes) with $|Z| \approx 1$; the related microscopic states are non-oscillatory; i.e., most of the neurons are *quiescent* (Q), and therefore, their spiking activity is negligible, $r \approx 0$. This branch of equilibria may undergo two saddle-node bifurcations (SN_1 and SN_2) that are connected by a branch of saddles.

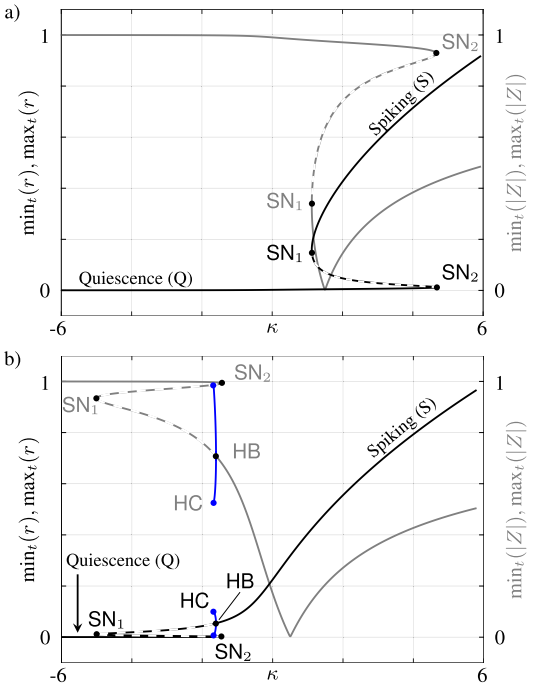

FIG. 2. Bifurcation diagrams in κ for $M = 1$ population of theta neurons. We display solution branches by reporting maxima and minima in the firing rate r (black) and synchrony level $|Z|$ (gray), respectively. Stable and unstable branches of equilibria have coinciding minima/maxima and are shown solid and dashed, respectively; minima/maxima corresponding to limit cycle behavior are highlighted in blue. Bifurcations that may occur are saddle node (SN_1, SN_2), Hopf (HB), and homoclinic (HC). Fixed parameters are $\Delta = 0.01$ and pulse shape parameter $s = 1$, while $\hat{\eta} = -0.5$ and $\hat{\eta} = 0.5$ in panels (a) and (b), respectively.

Equilibria to the right of SN_1 (larger κ) are stable spirals and correspond to *spiking* neurons (S) with larger firing rate $r > 0$. As the coupling strength κ increases, higher levels of synchrony, eventually getting close to $|Z| = 1$, may be achieved.

For the case of spiking (firing) neurons ($\hat{\eta} > 0$), the bifurcation diagram in Fig. 2(b) reveals a similar bifurcation structure with two saddle-node bifurcations. However, for certain values of $\hat{\eta}$, an even more complicated bifurcation scenario is possible along the branch to the right of SN_1: a supercritical Hopf bifurcation (HB) gives birth to limit cycles, which ultimately are destroyed in a homoclinic bifurcation (HC). In between the values of $\hat{\eta} = -0.5$ and $\hat{\eta} = 0.5$ shown in Fig. 2, two distinct bifurcations of codimension 2 occur: (i) SN_1 and SN_2 merge in a cusp point and (ii) the bifurcation curves SN_1, HB, and HC meet in a Bogdanov–Takens point. The scenario in which limit cycles occur is characteristic for spiking neurons ($\hat{\eta} > 0$)

with inhibitory coupling ($\kappa < 0$), as can be shown by further bifurcation analysis. For further details on these bifurcation structures, see Refs. 7 and 51.

Importantly, we note that collective oscillations emerging in the Hopf bifurcation HB cease to exist in the limit of pulses defined by (3) with zero width obtained in the limit of $s \to \infty$. While this was already noted in recent studies,[50,57] we briefly outline a derivation of this fact in Appendix A. Further investigations of ours show that Hopf bifurcations continue to exist for a large range of values of the pulse shape parameter, s. Our observations suggest that the Hopf bifurcations giving birth to oscillations only vanish in the limit of $s \to \infty$, prompting a degeneracy for this limit. The case of infinitely narrow pulses, $s = \infty$, provides the advantage that the fixed point conditions resulting from the corresponding FRE can be solved in a closed form, enabling a simple mathematical analysis. However, since this case produces a degenerate bifurcation behavior where limit cycles are absent, we chose to fix $s = 1$.

Between the pair of fold bifurcations (SN_1 and SN_2), a parameter region of bistability arises, thus facilitating hysteretic behavior. This happens for excitable neurons, $\hat{\eta} < 0$, with *excitatory coupling*, $\kappa > 0$, as well as for parameters corresponding to firing neurons, $\hat{\eta} > 0$, with inhibitory coupling, $\kappa < 0$. This bistable character of solutions observed for $M = 1$ population translates to the case of $M = 2$ populations, where each population may attain distinct stable configurations.

In the following, we consider non-zero pulse width ($s = 1$) and fix parameter values to $\hat{\eta} = -1$ (excitable neurons) and $\Delta = 0.01$,

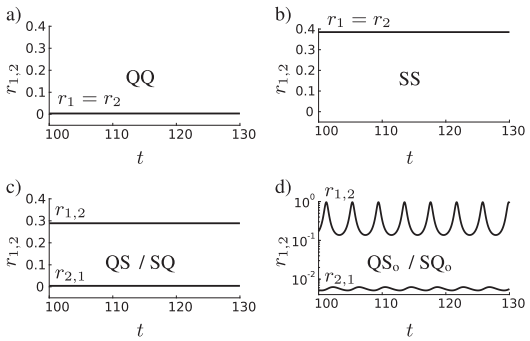

FIG. 3. Asymptotic dynamic behaviors for the two population model after transients. Low and high levels of the firing rate $r(t)$ indicate quiescent (Q) or spiking (S) behavior. (a) Symmetric (stable) equilibrium where both populations are quiescent (QQ). (b) Symmetric (stable) equilibrium where both populations are spiking (SS). (Transients leading up to the equilibrium are oscillatory.) (c) Asymmetric (stable) equilibrium where one population is quiescent and the other spiking (QS or SQ). (Transients leading up to the equilibrium are oscillatory only for the spiking population.) (d) Asymmetric (stable) limit cycle (QS_o or SQ_o) where both populations oscillate with the same period (but with different amplitudes). The coupling parameter is $\kappa = 1.8$ for panels (a)–(c) and $\kappa = 2.2$ for panel (d); parameters $a = 0.25$, $\hat{\eta} = -1$, $\Delta = 0.01$, $s = 1$ are fixed throughout.

while varying the intra-coupling strength, κ, and the inter-coupling strength, a.

IV. ANALYSIS FOR TWO POPULATIONS

A. Symmetric and asymmetric equilibria

It is instructive to begin the analysis by surveying the possible asymptotic dynamic behavior for the firing rates r_1 and r_2 (or equivalently, Z_1 and Z_2) in the FRE (19) and (20) for $M = 2$ populations. We may distinguish two types of asymptotic states as $t \to \infty$, namely, (i) *symmetric states* characterized by $r_1(t) = r_2(t)$ and $v_1(t) = v_2(t)$ and (ii) *asymmetric states* characterized by $r_1(t) \neq r_2(t)$ and $v_1(t) \neq v_2(t)$. Furthermore, each neuron population may be in a state of *quiescence* (Q) or *spiking* (S) depending on whether r_σ reflects low or high firing activity, respectively. In an asymmetric limit cycle, both populations oscillate around a distinct value corresponding to quiescence or spiking, respectively. Figure 3 illustrates the possible asymptotic states that may be observed depending on parameter values and initial conditions chosen.

Solution branches reported in Fig. 2 for $M = 1$ population translate to symmetric states in the model with $M = 2$ populations. To see this, let us first consider two special parameter choices: $a = 0$ (decoupled populations) and $a = 1$ (two populations effectively act like one large population). In these cases, the system with $M = 2$ populations displays the same bifurcation behavior as $M = 1$ population, as shown in Fig. 4(a) for $a = 0$. The branch with a low firing rate (QQ) corresponds to quiescent neurons with coherent stationary phases, whereas the branch with a high firing rate (SS) corresponds to spiking populations whose synchronization level and firing rate grow with increasing coupling strength κ. Just as for $M = 1$ population, the system exhibits bistable regions in which both configurations, (Q)uiescence and (S)piking, are possible. However, note that in the case of $a = 1$, both populations may *only* attain identical (symmetric) configurations of quiescence or spiking, namely, SS or QQ; in contrast, the decoupled case with $a = 0$ additionally and trivially allows for the two populations to attain distinct (asymmetric) configurations, namely, SQ or QS. Importantly, symmetric states persist even when $a \neq 0$ or $a \neq 1$ since parameters are symmetric across the two populations. Specifically, if r is an equilibrium of the $M = 1$ population system, then so is (r, r) an equilibrium of the $M = 2$ population system but now with κ replaced by $\kappa/(1 + a)$. For this reason, the solution branches of symmetric equilibria seen for $M = 1$ translate to the $M = 2$ system, including the saddle-node bifurcations SN_1 and SN_2 seen in Fig. 2, in between which, for $a \geq 0$, two stable symmetric states SS and QQ co-exist. However, for $a < 0$, the region of bistability for symmetric states is bounded by the pitchfork bifurcations PF_1 and PF_2 rather than SN_1 and SN_2 since both branches emanating from the bifurcation point SN_1 (SN_2) are unstable, one of them gaining stability at PF_1 (PF_2); see Figs. 4(c) and 6(a). PF_1 and PF_2 also give rise to asymmetric states, as we explain in the following.

Asymmetric states, corresponding to QS or SQ configurations with $r_1 \neq r_2$, are trivially possible when the two populations are decoupled ($a = 0$); however, their range of existence and stability off the degenerate cases $a \neq 0$ and $a \neq 1$ deserves further exploration, and we consider small perturbations for $a \neq 0$. Considering

the case of $a = 0.18$ in Fig. 4(b), we observe that unstable asymmetric states (light red) branch off the unstable symmetric state (gray) in pitchfork bifurcations PF_1 and PF_2 (see also the inset). The set of asymmetric equilibria forms a loop in the (κ, r)-space with two folds; i.e., the equilibria undergo saddle-node bifurcations in SN_3 and SN_4 between which asymmetric states are stable. As a result, the QS and SQ (red) emerge as bistable asymmetric configurations. These stable asymmetric branches may co-exist with the bistable symmetric solution branches QQ and SS (black). Note that for $a > 0$, PF_1 and PF_2 lie outside SN_3 and SN_4, while for $a < 0$, PF_1 and PF_2 lie inside SN_3 and SN_4; as a consequence, the existence of asymmetric states is bounded by PF_1 and PF_2 for $a > 0$ and SN_3 and SN_4 for $a < 0$; see Figs. 4(b) and 4(c). Moreover, for $a > 0$, asymmetric states exist only in a relatively narrow range of intermediate coupling strength κ; by contrast, for $a \leq 0$, the κ-range of existence of asymmetric equilibria rapidly expands as the value of a decreases [see Fig. 6(a)].

Note that considering the case of decoupled populations with $a = 0$, symmetric and asymmetric branches may appear like they coincide when inspecting Fig. 4; however, the two types of solution branches are not identical: While the projections $Z_1 \in \mathbb{C}$ and $Z_2 \in \mathbb{C}$ indeed share identical values for symmetric and asymmetric equilibria, this cannot hold true in the full phase space for $(Z_1, Z_2) \in \mathbb{C}^2$, where the definitions for symmetric ($r_1 = r_2, \nu_1 = \nu_2$) and asymmetric states ($r_1 \neq r_2, \nu_1 \neq \nu_2$) are obeyed.

B. Birth and destruction of limit cycle oscillations

For larger values of the inter-coupling strength, a, asymmetric equilibria QS (SQ) may undergo Hopf bifurcations giving rise to limit cycle oscillations (QS_o, SQ_o), indicated by their minima/maxima (blue) in Figs. 5(a)–5(d). Since these limit cycles branch off asymmetric equilibria (red), they correspond to asymmetric configurations characterized by firing rates $r_1(t) \neq r_2(t)$. These limit cycles are created and destroyed in various bifurcations, as outlined in the following.

1. Birth of stable limit cycles (HB_-)

Stable limit cycles (blue minima/maxima) are born in the supercritical Hopf bifurcation denoted by HB_-, as shown in Fig. 5(a) for $a = 0.204$. As κ increases, the amplitude waxes and wanes, as the bifurcation HB_- is intersected twice in the direction of varying κ; see also Fig. 6.

2. Birth of stable/unstable limit cycles and annihilation in saddle-node-of-limit-cycle bifurcation (HB_-, HB_{+-}, $SNLC_1$)

Stable limit cycles (blue) are still born in a supercritical Hopf bifurcation at HB_-, but now an unstable limit cycle (light blue) of a smaller amplitude emerges for greater κ in the supercritical Hopf (with repelling center manifold) at HB_{+-}. The continuum of cycles folds over in a *saddle-node of limit cycle* bifurcation at $SNLC_1$, where the stable and unstable limit cycles coalesce and disappear; see Fig. 5(b) for $a = 0.25$.

3. Stabilization of an unstable limit cycle in secondary saddle-node-of-limit-cycle bifurcation ($SNLC_2$)

Stable and unstable limit cycles are created in HB_- and HB_{+-}. While the stable limit cycle is destroyed in the homoclinic bifurcation HC_-, the unstable limit cycle is subject to a more complicated

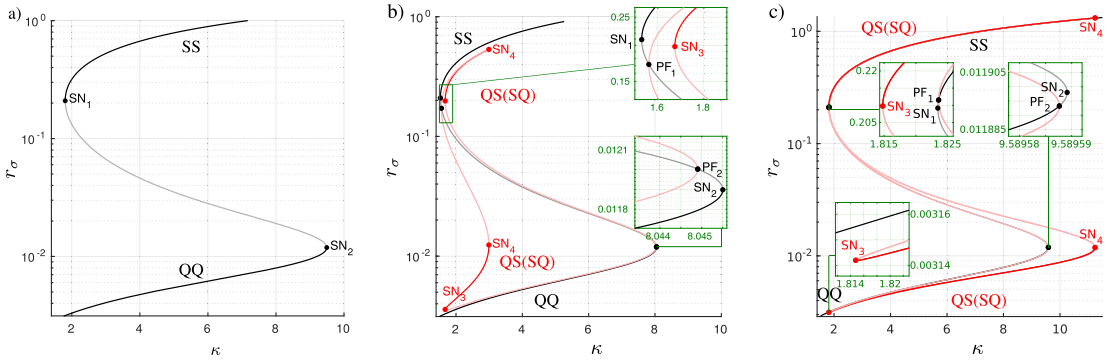

FIG. 4. Bifurcation diagrams for $M = 2$ populations in κ for the firing rate r_σ reveal symmetric equilibria, $r_1 = r_2$ (black, gray) and asymmetric equilibria, $r_1 \neq r_2$, (red, light red), emerging in bifurcations as follows. (a) $a = 0$: Both populations are decoupled. Symmetric equilibria are folded in two saddle-node bifurcations (SN_1, SN_2) where the lower and upper branches (black) corresponding to (Q)uiescence and (S)piking, respectively, are stable; the middle branch (gray) is unstable. Thus, four states are possible, (SS, QQ, QS and SQ), facilitating multistability and hysteretic behavior. (b) $a = 0.18$: Symmetric equilibria with $r_1 = r_2$ seen for $a = 0$ are still present (black, gray). However, the unstable branch (gray) undergoes a pitchfork bifurcation in PF_1 and PF_2, giving rise to unstable asymmetric equilibria QS/SQ with $r_1 \neq r_2$ (light red). These equilibria are connected in a loop, folded twice in two saddle-node bifurcations (SN_3 and SN_4), giving rise to the co-existence of two stable asymmetric states (red) where one population is quiescent while the other is spiking (SQ or QS). (c) $a = -0.01$: For $a < 0$, the order of SN_3, SN_4 and SN_1, SN_2, PF_1, PF_2 is reversed along the κ direction when compared to $a > 0$. Parameters are $\Delta = 0.01$, $\hat{\eta} = -1$, $s = 1$ everywhere. Chosen values for a are indicated as dashed horizontal lines in Fig. 6.

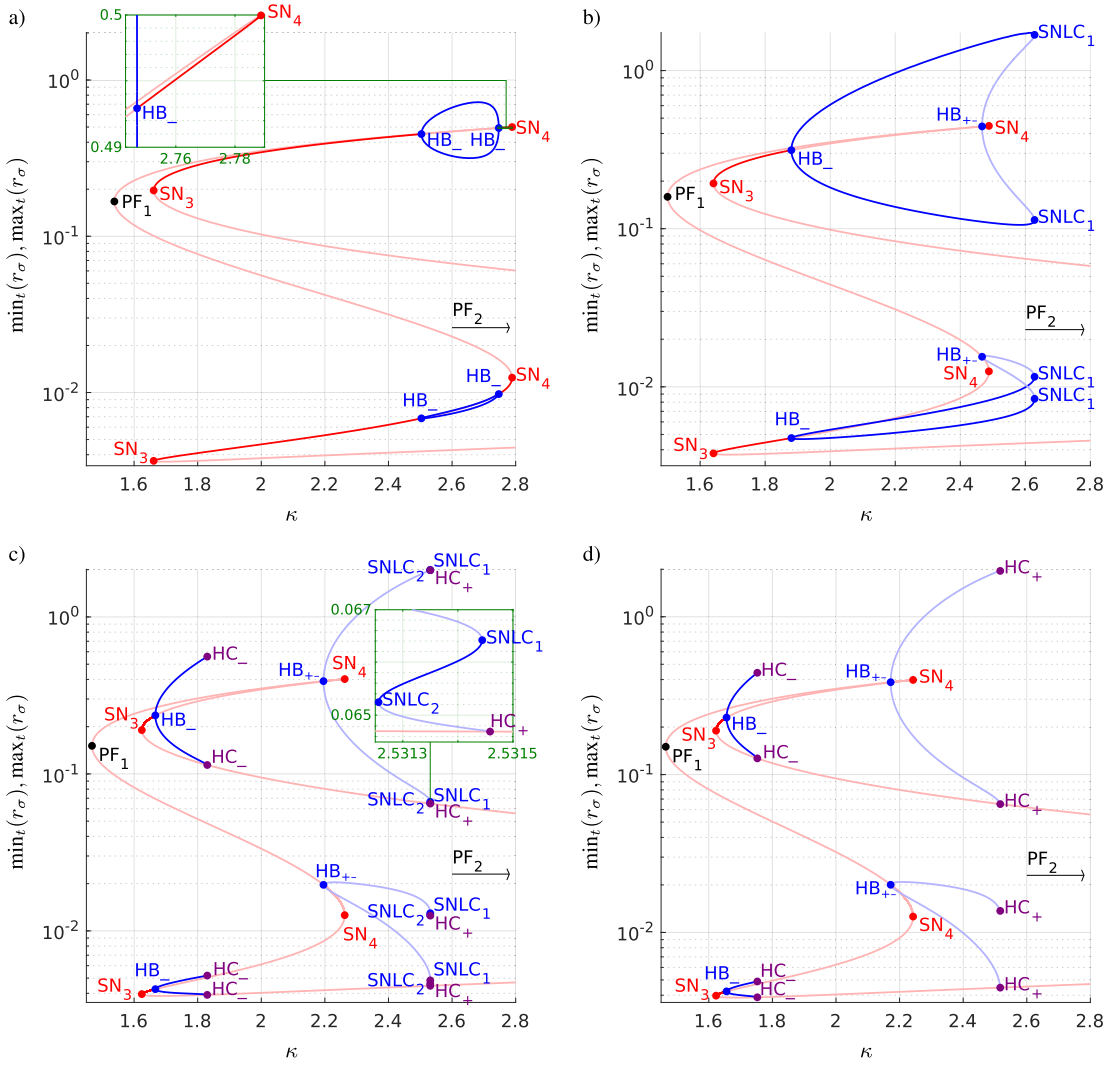

FIG. 5. Birth and destruction of asymmetric limit cycle oscillations (blue) in the firing rate for $M = 2$ populations while varying κ. Possible bifurcation scenarios are illustrated for various values of a (also indicated as dashed lines in Fig. 6). (a) $a = 0.204$: stable limit cycles are born in the supercritical Hopf bifurcation HB_- (the bifurcation curve is intersected twice; see Fig. 6). (b) $a = 0.25$: stable and unstable limit cycles are born in HB_- and HB_{+-}, respectively, and annihilate in a saddle-node of limit cycles bifurcation ($SNLC_1$). (c) $a = 0.297$: stable and unstable limit cycles are destroyed in a homoclinic bifurcation HC_- and HC_+, respectively. Moreover, the unstable cycle is subject to two saddle-node-of-limit-cycle bifurcations at $SNLC_1$ and $SNLC_2$, in between which it gains stability (see the inset); the unstable limit cycle branch emerging from $SNLC_2$ gets destroyed in HC_+. (d) $a = 0.302$: the unstable limit cycle born in HB_{+-} is destroyed in the homoclinic HC_+ saddle-node-of-limit-cycle bifurcations are now absent. Symmetric equilibria connecting to PF_1 and PF_2 are omitted for simplicity. Stable and unstable solution branches are shown as dark and light colored shades, respectively. Parameters are $\Delta = 0.01$, $\hat{\eta} = -1$, $s = 1$ everywhere.

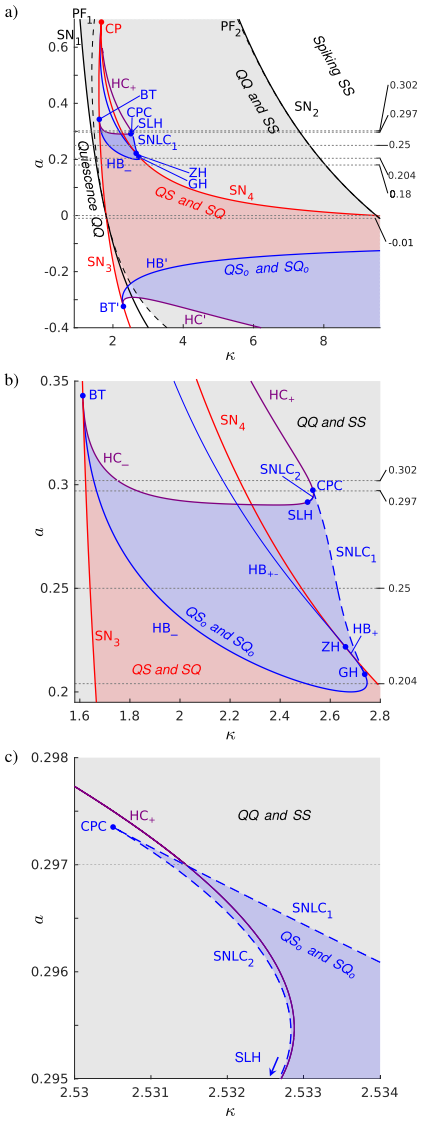

FIG. 6. Stability diagram for $M = 2$ populations in the (κ, a)-parameter plane with $\Delta = 0.01$, $\hat{\eta} = -1$, $s = 1$ fixed. Gray shading indicates a bistable region of the two stable symmetric equilibria, QQ and SS. Red shading indicates the bistable region of stable asymmetric equilibria, that is, QS or, equivalently, SQ. Blue shading indicates the bistable region of stable asymmetric limit cycles (QS_o and SQ_o). Dashed black lines delineate the choices of parameter a for the bifurcation diagrams in Figs. 4 and 5.

series of bifurcations: It undergoes not only one, but two saddle-node of cycle bifurcations, $SNLC_2$ and $SNLC_1$. The unstable limit cycle emerging from $SNLC_2$ collides with the saddle equilibrium of the asymmetric branch in the *homoclinic* bifurcation HC_+ and is destroyed, as shown in Fig. 5(c) for $a = 0.297$.

4. Simple birth and destruction of stable/unstable limit cycles (HB_-, HC_-, HB_{+-}, HC_+)

The stable and unstable limit cycles are born in the Hopf bifurcations HB_- and HB_{+-} and are destroyed in the homoclinic bifurcations HC_- and HC_+, respectively. The complicated scenario including two saddle-node-of-limit-cycle bifurcations from Sec. IV B 3 is entirely absent. This simple scenario is shown in Fig. 5(d) for $a = 0.302$.

C. Stability diagram

We now explain how the various bifurcation scenarios are related; i.e., how stability boundaries are connected in the (κ, a)-parameter plane and how bifurcation curves are structured around bifurcation points of a higher co-dimension.

Let us first consider the overall bifurcation structure for a larger parameter range (κ, a) as displayed in Fig. 6(a), mainly focusing on symmetric (QQ, SS) and asymmetric equilibria QS (or SQ). On the branches of *symmetric* equilibria (QQ, SS), two saddle-node bifurcations occur, SN_1 and SN_2 (black), which coalesce in a codimension 2 cusp point for large a (not shown). The gray shaded region of bistability between QQ and SS is bounded by SN_1 and SN_2 for $a \geq 0$ and by PF_1 and PF_2 [dashed black curves in Fig. 6(a)] for $a < 0$, respectively. Note that the curve PF_2 lies very close to SN_2 in the shown parameter range, $-0.4 \leq a \leq 0.7$.

Unstable saddle branches of the symmetric equilibria between (or outside) SN_1 and SN_2 undergo pitchfork bifurcations PF_1 and PF_2, which give rise to unstable asymmetric branches [see light red curves in Figs. 4(b) and 4(c) and Figs. 5(a)–5(d)]. These unstable asymmetric branches gain stability on the saddle-node bifurcation curves SN_3 and SN_4 [red curves in Fig. 6(a)], which meet in the codimension 2 cusp point CP. The resulting asymmetric stable configurations (QS or SQ) reside inside the red shaded region bounded by the saddle-node bifurcation curves SN_3 and SN_4 and the supercritical Hopf bifurcation curves HB_- and HB′.

In HB_- and HB′, stable asymmetric equilibria QS and SQ lose stability, resulting in stable asymmetric limit cycles QS_o (or SQ_o) within the blue shaded regions; these limit cycles may get destroyed in the homoclinic bifurcations denoted by HC_- and HC′ (violet). Hopf (HB_- and HB′) and homoclinic bifurcation curves associated with the emergence and destruction of these limit cycles (HC_- and HC′) meet with the (asymmetric) saddle-node bifurcation curve SN_3 in two other bifurcation points of codimension 2, namely, the Bogdanov–Takens points BT and BT′, respectively, characterized by double zero eigenvalues.[58]

The bifurcations pertaining to the asymmetric limit cycles are structured around further, more complicated bifurcation curves and bifurcation points of a higher co-dimension; see Figs. 6(b) and 6(c). Following the Hopf bifurcation curve HB_- in panel (b), we arrive at a Generalized Hopf bifurcation point (GH) of codimension 2.[58,59]

Such a point not only has a pair of purely imaginary eigenvalues, but also the first Lyapunov coefficient for the Hopf bifurcation changes sign at this point so that subcritical (HB_+) and supercritical (HB_-) Hopf bifurcations are separated in GH; in addition, a branch of saddle-node of limit cycle bifurcations, $SNLC_1$, emerges from GH where the stable and unstable limit cycles born in HB_- and HB_+ are annihilated.

Following the bifurcation curve HB_+, the associated subcritical Hopf bifurcation tangentially intersects the saddle-node bifurcation SN_4 in the Zero-Hopf bifurcation ZH (or saddle-node Hopf bifurcation),[58,60] characterized by a zero eigenvalue and a pair of purely imaginary eigenvalues. At ZH, the first Lyapunov coefficient vanishes once more and changes sign. Hopf bifurcations HB_{+-} above the ZH point are supercritical (i.e., having a negative first Lyapunov coefficient) but continue to produce unstable limit cycles as the center manifold (of the Hopf bifurcation) is repelling.

Following the saddle-node bifurcation of limit cycle curve $SNLC_1$, we observe that it terminates in another bifurcation point of codimension 2, Cusp of Cycles (CPC), where it collides with a second saddle-node bifurcation of limit cycles curve $SNLC_2$. This latter bifurcation curve merges with the homoclinic bifurcation curve HC_+ in a codimension ≥ 2 point SLH; see Fig. 6(c). The point SLH separates two branches of the homoclinic curves, HC_- and HC_+, and tangentially intersects with $SNLC_2$. Homoclinic bifurcations on HC_- (HC_+) destroy stable (unstable) limit cycles as κ approaches the homoclinic bifurcation point from above (below).

We come to the following conclusion. In similarity with the case of $M = 1$ population, the cases of very small and very strong coupling κ result in regimes with quiescent and spiking activity, respectively; both are characterized by high levels of synchrony. In the intermediate regime, the dynamic behavior is more complicated. We thus find the following five stability regions: (i) for small coupling strength κ, both populations are quiescent, corresponding to the symmetric configuration QQ (white region); (ii) for large coupling strength κ, both populations are spiking, corresponding to the symmetric configuration SS (white region); (iii) for intermediate coupling strengths, we find a region of bistability between the configurations QQ and SS; this region of bistability co-exists with asymmetric configurations of either (iv) stationary firing rate, SQ or QS (red region), or (v) oscillatory firing rates, SQ_o or QS_o (blue region). In addition, there are regions for intermediate coupling strengths where only QQ co-exists stably with SQ and QS or only SS with SQ and QS [see Fig. 6(a)].

V. DISCUSSION

Collective oscillations in neural ensembles are responsible for the rhythm generation required for solving functionally relevant tasks in the brain.[10,18,45] Collective oscillations may be facilitated by a variety of network setups, including heterogeneous networks with excitatory and inhibitory coupling leading to gamma rhythms.[48,49] Here, we investigated the emergence of collective oscillations in a simple model consisting of a homogeneous network composed of two (statistically) identical populations of type 1 neurons with non-uniform but symmetric coupling; i.e., neurons are coupled with strength κ and $a\kappa$ (with $a \neq 1$) within and between the two populations, respectively.

In this model, each population may assume states corresponding to quiescent (Q) or spiking (S) firing activity. Thus, we may distinguish symmetric configurations, where both populations are either quiescent or spiking (QQ, SS), and asymmetric configurations, where one population is quiescent but the other is spiking (SQ, QS). We found that stable symmetric configurations may co-exist for certain parameter choices [see Fig. 4(a)]. We did not find that symmetric configurations are oscillatory except for uniform coupling ($a = 1$) or for absent inter-coupling ($a = 0$). As we deviate from uniform coupling, $a \neq 1$, *unstable* asymmetric equilibria emerge from symmetric configurations in symmetry-breaking pitchfork bifurcations. Along these solution branches, asymmetric equilibria may further undergo saddle-node bifurcations and thus gain stability [see Fig. 4(b)]. Asymmetric oscillatory configurations (QS_o, SQ_o) emerge in Hopf bifurcations (Fig. 5) that are organized around higher codimension bifurcation points. Depending on parameters, symmetric and asymmetric configurations may be stable and co-exist, resulting in multistability between either stationary configurations only (QQ, SS, QS, SQ) or between stationary and oscillatory configurations (QQ, SS, QS_o, SQ_o). For these regions of stability, we have determined valid parameter regions and stability boundaries (Fig. 6).

Oscillator networks with such a modular network structure are known to exhibit a high degree of multistability; i.e., depending on initial conditions, a variety of dynamic configurations for the collective states may be assumed in each population. A prominent example is synchronization patterns known as chimera states in Kuramoto oscillator networks,[27,29,34] which may be employed to store memory or perform computations[61] or direct the flow of information between populations.[8,26] However, compared to Kuramoto networks with rigidly rotating oscillators, the excitable nature of neurons intrinsically leads to more complicated dynamics and synchronization behavior.[62] While complicated dynamics may arise in networks composed of identical Kuramoto oscillators arranged with at least two populations (as well as for broken parameter symmetries),[28,63] excitable type 1 neurons produce rich bifurcation behavior and bistability already for a single population, as illustrated in Fig. 4 and discussed in Refs. 7 and 8. Such multistability is of great interest in applications, e.g., in neuroscience. A recent study modeled networks of type 1 neurons and demonstrated how the bistability between low and high firing activity—resulting in a large configuration space that scales with the number of populations—may be employed to solve cognitive tasks such as memory storage and recall.[37]

Several studies considered networks of type 1 neurons in terms of their macroscopic behavior. The collective dynamics of a single population was studied in terms of non-identical theta neurons with non-zero pulse width,[7,51] of the response to an external (rigid) forcing,[36] of quadratic integrate-and-fire neurons,[6] and of different coupling functions, oscillations, and aging transitions,[37] and of the role of distributed delay in the coupling function.[64] Luke *et al.*[36] studied a two population model similar to ours; however, they considered unidirectional coupling. This driver-response system exhibits some of the bifurcation structures and collective macroscopic behaviors that we reported here; i.e., the response population exhibits multistable equilibrium states and limit cycles. In addition, their system exhibits chaotic behavior, which was also reported by

Ceni *et al.*[65] who considered a similar setup but with exponentially decaying synapses leading to three dimensional dynamics for the macroscopic firing rate equations. Unlike their study, we did not observe quasiperiodic and chaotic dynamics. While we restricted our study to symmetric parameter configurations between the two populations, future research might address the question if breaking parameter symmetries between the populations (such as the coupling strength) may induce bifurcations, leading to chaos. For such cases, one may envision torus bifurcations emerging from the zero-Hopf bifurcations,[58] offering a route to chaos via bifurcations of Shil'nikov homoclinic orbits to saddle foci. Ratas and Pyragas[66] studied a network of quadratic integrate-and-fire neurons with two populations. While their system is similar to ours, it differs in some important aspects. First, neurons are considered to be strongly heterogeneous with an excitability spread around $\hat{\eta} = 0$, thus resulting in a network including both excitable and spiking neurons; here, the majority of neurons are excitable. Second, for the coupling function, they use a threshold modulation coupling function corresponding to a Heaviside function. This system exhibits steady and oscillatory states with symmetric and asymmetric character but unlike our system, also chaotic behavior and states characterized by anti-phase configurations.

To study collective oscillations of firing activity in our model, it is necessary to deviate from the case of instantaneous pulse coupling ($s \to \infty$) where collective oscillations are absent (see Appendix A and Refs. 50 and 57). The pulse width given by Eq. (3) with $s = 1$ was large; other pulse shape models[4,6] may be more realistic and consider that incident pulses arrive instantaneously in order to decay exponentially fast upon arrival over a characteristic time scale τ. It is then frequently assumed that $\tau \to 0$, resulting in time-symmetric and instantaneous pulses. This strategy certainly simplifies analysis; yet, it appears that this limit biophysically is no more realistic especially since it results in the same macroscopic equations as given by (19) and (20) for the limit of $s \to \infty$; this again rules out the potential to produce any macroscopic oscillations. For a future study, it might be interesting to examine how the specific choice of pulse shape in terms of width and time-asymmetry affects the unfolding of bifurcations. While many studies either studied small values of s or $s \to \infty$, it would be interesting to see how the bifurcation scenarios reported in this study translate to the case of causal synaptic potentials that decay exponentially in time.[67]

Many questions remain. For instance, breaking parameter symmetry may result in richer dynamics[30] including chaos;[63] is chaotic motion feasible if excitability parameters ($\hat{\eta}_\sigma$ and Δ_σ) are nonidentical or if a small delay is introduced in the coupling? Are bifurcation scenarios for spiking neurons ($\hat{\eta} > 0$) equally complicated as the ones we observed here for excitable neurons ($\hat{\eta} < 0$)? In terms of switching between configurations and devising a control method to do this, it may be useful to determine basins of attraction for the various configurations or responses to directed perturbations.[28,37] Furthermore, networks with larger population number $M > 2$ provide a larger set of dynamic configurations;[37,68,69] but how large is the set of configurations as a function of the population number and which of the configurations are stable and which ones are oscillatory? Future studies may address such and further questions.

ACKNOWLEDGMENTS

The authors would like to thank C. Bick and B. Pietras for helpful discussions, and A. Torcini and P. So for helpful correspondence. Research conducted by B.J. was partially supported by funding from the EU-COST Technical University of Denmark.

APPENDIX A: COLLECTIVE OSCILLATIONS FOR NON-ZERO PULSE WIDTH ($s < \infty$)

We briefly discuss the existence of Hopf bifurcations and resulting limit cycle oscillations in the firing rate $r(t)$ for varying pulse shape parameter s for the simple case of $M = 1$ population. To determine the presence of Hopf instabilities, we examine eigenvalues of the Jacobian of (19),

$$J = \begin{pmatrix} 2v & 2r \\ -2\pi^2 r + \frac{\partial}{\partial r} I & 2v + \frac{\partial}{\partial v} I \end{pmatrix}. \tag{A1}$$

Steady state of (19) implies $v^* = -\frac{\Delta}{2\pi}\frac{1}{r^*}$ so that

$$\mathrm{tr}(J) = -\frac{2\Delta}{\pi}\frac{1}{r^*} + \frac{\partial}{\partial v} I|_{(r,v)=(r^*,v^*)}. \tag{A2}$$

A necessary condition for a Hopf bifurcation is that $\mathrm{tr}(J) = 0$. For the case of infinitely narrow pulses, $s = \infty$, Hopf bifurcations are impossible: we have $\frac{\partial}{\partial v} I = \kappa \frac{\partial}{\partial v} P^{(\infty)} = 0$ thus and $\mathrm{tr}(J) = -2\Delta/\pi/r^* < 0$ for all $r^* > 0$. Hence, Hopf bifurcations and resulting limit cycles regardless of the choice of parameters can be ruled out for this case.

Conversely, we know that Hopf bifurcations are possible for $s = 1$ (see Fig. 2) and $s = 2$ (see Luke *et al.*[7]). Indeed, the trace for $1 < s < \infty$ involves more complicated terms, and Hopf bifurcation cannot easily be ruled out. While an analytical proof remains elusive, using a numerical analysis based on solving the zero trace condition, one finds that limit cycle oscillations are feasible for a large range of pulse shape parameters, including at least $1 \leq s \leq 20$.

APPENDIX B: METHODOLOGY

The data for the bifurcation diagrams in Figs. 4 and 5 were obtained via numerical continuation of equilibria and limit cycles (using MatCont software) in the parameter κ; thus, we encountered codimension-1 bifurcation points SN_1, SN_2, SN_3, SN_4, HB_-, HB_+, HB_{+-}, HB′, HC_-, HC_+, HC′, $SNLC_1$, $SNLC_2$, PF_1, PF_2. With the exception of PF_1 and PF_2 we continued all these degenerate states as bifurcation curves in the parameters κ and a using MatCont (Fig. 6); therefore, we detected the codimension ≥ 2 bifurcation points reported in Sec. IV C. The direct two-parameter continuation of the bifurcation curves PF_1, PF_2 posed technical problems when using MatCont; alternatively, we, therefore, determined the loci of PF_1 and PF_2 by computing bifurcation diagrams in a single parameter, κ, for set values of a, resulting in the parameter list (κ, a) in Table I. The curves shown in Fig. 6 (dashed black curves) are splines interpolating these data points.

TABLE I. Bifurcation points numerically detected for PF_1 and PF_2.

a	κ (PF_1)	κ (PF_2)
0.7	1.476	5.546
0.65	1.438	5.728
0.6	1.414	5.915
0.5	1.400	6.320
0.4	1.419	6.777
0.35	1.439	7.029
0.25	1.500	7.594
0.204	1.538	7.884
0.18	1.561	8.045
0.1	1.652	8.630
−0.01	1.824	9.590
−0.05	1.904	9.993
−0.1	2.020	10.548
−0.15	2.160	11.169
−0.2	2.329	11.867
−0.27	2.632	13.004
−0.35	3.117	14.604
−0.4	3.538	15.821

DATA AVAILABILITY

Data sharing is not applicable to this article as no new data were created or analyzed in this study.

REFERENCES

[1]G. B. Ermentrout and N. Kopell, "Parabolic bursting in an excitable system coupled with a slow oscillation," SIAM J. Appl. Math. **46**(2), 233–253 (1986).
[2]P. E. Latham, B. J. Richmond, P. G. Nelson, and S. Nirenberg, "Intrinsic dynamics in neuronal networks. I. Theory," J. Neurophysiol. **83**(2), 808–827 (2000).
[3]D. Hansel and G. Mato, "Existence and stability of persistent states in large neuronal networks," Phys. Rev. Lett. **86**(18), 4175–4178 (2001).
[4]W. Gerstner, W. M. Kistler, R. Naud, and L. Paninski, *Neuronal Dynamics: From Single Neurons to Networks and Models of Cognition* (Cambridge University Press, 2014).
[5]E. Ott and T. M. Antonsen, "Low dimensional behavior of large systems of globally coupled oscillators," Chaos **18**(3), 037113 (2008).
[6]E. Montbrió, D. Pazó, and A. Roxin, "Macroscopic description for networks of spiking neurons," Phys. Rev. X **5**(2), 021028 (2015).
[7]T. B. Luke, E. Barreto, and P. So, "Complete classification of the macroscopic behavior of a heterogeneous network of theta neurons," Neural Comput. **25**, 3207–3234 (2013).
[8]C. Bick, C. Laing, M. Goodfellow, and E. A. Martens, "Understanding the dynamics of biological and neural oscillator networks through exact mean-field reductions: A review," J. Math. Neurosci. **10**, 9 (2020).
[9]Á. Byrne, D. Avitabile, and S. Coombes, "Next-generation neural field model: The evolution of synchrony within patterns and waves," Phys. Rev. E **99**, 012313 (2019).
[10]E. Marder and D. Bucher, "Central pattern generators and the control of rythmic movements," Curr. Biol. **11**, R986–R996 (2001).
[11]J. C. Smith, H. H. Ellenberger, K. Ballanyi, D. W. Richter, and J. L. Feldman, "Pre-Bötzinger complex: A brainstem region that may generate respiratory rhythm in mammals," Science **254**(5032), 726–729 (1991).
[12]G. Buzsáki and X.-J. Wang, "Mechanisms of gamma oscillations," Annu. Rev. Neurosci. **35**(1), 203–225 (2012).
[13]E. T. Bullmore and O. Sporns, "Complex brain networks: Graph theoretical analysis of structural and functional systems," Nat. Rev. Neurosci. **10**(3), 186–198 (2009).
[14]D. Meunier, R. Lambiotte, and E. T. Bullmore, "Modular and hierarchically modular organization of brain networks," Front. Neurosci. **4**, 200 (2010).
[15]K. D. Harris, "Neural signatures of cell assembly organization," Nat. Rev. Neurosci. **6**(5), 399–407 (2005).
[16]C. W. Lynn and D. S. Bassett, "The physics of brain network structure, function and control," Nat. Rev. Phys. **1**, 318–332 (2019).
[17]L. Glass, "Synchronization and rhythmic processes in physiology," Nature **410**, 277–284 (2001).
[18]P. J. Uhlhaas and W. Singer, "Neural synchrony in brain disorders: Relevance for cognitive dysfunctions and pathophysiology," Neuron **52**(1), 155–168 (2006).
[19]J. Fell and N. Axmacher, "The role of phase synchronization in memory processes," Nat. Rev. Neurosci. **12**(2), 105–118 (2011).
[20]P. Fries, "Neuronal gamma-band synchronization as a fundamental process in cortical computation," Annu. Rev. Neurosci. **32**, 209–224 (2009).
[21]X. J. Wang, "Neurophysiological and computational principles of cortical rhythms in cognition," Physiol. Rev. **90**(3), 1195–1268 (2010).
[22]W. Singer and C. M. Gray, "Visual feature integration and the temporal correlation hypothesis," Annu. Rev. Neurosci. **18**, 555–586 (1995).
[23]P. Fries, "A mechanism for cognitive dynamics: Neuronal communication through neuronal coherence," Trends Cogn. Sci. **9**(10), 474–480 (2005).
[24]M. I. Rabinovich, V. S. Afraimovich, C. Bick, and P. Varona, "Information flow dynamics in the brain," Phys. Life Rev. **9**(1), 51–73 (2012).
[25]C. Kirst, M. Timme, and D. Battaglia, "Dynamic information routing in complex networks," Nat. Commun. **7**, 11061 (2016).
[26]N. Deschle, A. Daffertshofer, D. Battaglia, and E. A. Martens, "Directed flow of information in chimera states," Front. Appl. Math. Stat. **5**(28), R102 (2019).
[27]D. M. Abrams, R. Mirollo, S. H. Strogatz, and D. A. Wiley, "Solvable model for chimera states of coupled oscillators," Phys. Rev. Lett. **101**, 084103 (2008).
[28]E. A. Martens, M. J. Panaggio, and D. M. Abrams, "Basins of attraction for chimera states," New J. Phys. **18**, 022002 (2016).
[29]E. A. Martens, "Bistable chimera attractors on a triangular network of oscillator populations," Phys. Rev. E **82**(1), 016216 (2010).
[30]E. A. Martens, C. Bick, and M. J. Panaggio, "Chimera states in two populations with heterogeneous phase-lag," Chaos **26**(9), 094819 (2016).
[31]C. R. Laing, "The dynamics of chimera states in heterogeneous Kuramoto networks," Physica D **238**(16), 1569–1588 (2009).
[32]C. R. Laing, K. Rajendran, and I. G. Kevrekidis, "Chimeras in random non-complete networks of phase oscillators," Chaos **22**(1), 013132 (2012).
[33]E. Schöll, "Synchronization patterns and chimera states in complex networks: Interplay of topology and dynamics," Eur. Phys. J. Spec. Top. **225**(6-7), 891–919 (2016).
[34]M. J. Panaggio and D. M. Abrams, "Chimera states: Coexistence of coherence and incoherence in networks of coupled oscillators," Nonlinearity **28**(3), R67 (2015).
[35]C. R. Laing, "Phase oscillator network models of brain dynamics," in *Computational Models of Brain and Behavior*, edited by A. A. Moustafa (Wiley-Blackwell, 2017), Chap. 37, pp. 505–518.
[36]T. B. Luke, E. Barreto, and P. So, "Macroscopic complexity from an autonomous network of networks of theta neurons," Front. Comput. Neurosci. **8**, 145 (2014).
[37]H. Schmidt, D. Avitabile, E. Montbrió, and A. Roxin, "Network mechanisms underlying the role of oscillations in cognitive tasks," PLoS Comput. Biol. **14**(9), e1006430 (2018).
[38]M. Yamakou, P. G. Hjorth, and E. A. Martens, "Optimal self-induced stochastic resonance in multiplex neural networks: Electrical versus chemical synapses," Front. Comp. Neuroscience **14**, 62 (2002).
[39]G. Weerasinghe, B. Duchet, H. Cagnan, P. R. Brown, C. Bick, and R. Bogacz, "Predicting the effects of deep brain stimulation using a reduced coupled oscillator model," PLoS Comp. Biology **15**(8) (2019).
[40]S. Watanabe and S. H. Strogatz, "Constants of motion for superconducting Josephson arrays," Physica D **74**(3-4), 197–253 (1994).
[41]C. R. Laing, "The dynamics of networks of identical theta neurons," J. Math. Neurosci. **8**, 4 (2018).
[42]H. R. Wilson and J. D. Cowan, "Excitatory and inhibitory interactions in localized populations of model neurons," Biophys. J. **12**(1), 1–24 (1972).
[43]S. Amari, "Dynamics of pattern formation in lateral-inhibition type neural fields," Biol. Cybern. **27**(2), 77–87 (1977).

[44]L. Lin, E. Barreto, and P. So, "Synaptic diversity suppresses complex collective behavior in networks of theta neurons," Front. Comput. Neurosci. **14**, 44 (2020).
[45]G. Buzsáki and B. O. Watson, "Brain rhythms and neural syntax: Implications for efficient coding of cognitive content and neuropsychiatric disease," Dialogues Clin. Neurosci. **14**, 345–367 (2012).
[46]P. Fries, D. Nikolić, and W. Singer, "The gamma cycle," Trends Neurosci. **30**(7), 309–316 (2007).
[47]S. Keeley, A. Fenton, and J. Rinzel, "Modeling fast and slow gamma oscillations with interneurons of different subtype," J. Neurophysiol. **117**(3), 950–965 (2017).
[48]S. Keeley, A. Byrne, A. Fenton, and J. Rinzel, "Firing rate models for gamma oscillations," J. Neurophysiol. **121**(6), 2181–2190 (2019).
[49]M. Segneri, H. Bi, S. Olmi, and A. Torcini, "Theta-nested gamma oscillations in next generation neural mass models," Front. Comput. Neurosci. **14**, 7373 (2020).
[50]F. Devalle, A. Roxin, and E. Montbrió, "Firing rate equations require a spike synchrony mechanism to correctly describe fast oscillations in inhibitory networks," PLoS Comput. Biol. **13**(12), e1005881 (2017).
[51]P. So, T. B. Luke, and E. Barreto, "Networks of theta neurons with time-varying excitability: Macroscopic chaos, multistability, and final-state uncertainty," Physica D **267**, 16–26 (2013).
[52]A. Dhooge, W. Govaerts, Yu. A. Kuznetsov, H. G. E. Meijer, and B. Sautois, "New features of the software MatCont for bifurcation analysis of dynamical systems," Math. Comput. Model. Dyn. Syst. **14**, 147–175 (2008).
[53]B. Ermentrout, "Ermentrout-Kopell canonical model," Scholarpedia **3**(3), 1398 (2008).
[54]J. T. Ariaratnam and S. H. Strogatz, "Phase diagram for the Winfree model of coupled nonlinear oscillators," Phys. Rev. Lett. **86**(19), 4281 (2001).
[55]G. B. Ermentrout and D. H. Terman, *Mathematical Foundations of Neuroscience*, Interdisciplinary Applied Mathematics Vol. 35 (Springer, New York, 2010).
[56]N. Brunel and P. E. Latham, "Firing rate of the noisy quadratic integrate-and-fire neuron," Neural Comput. **15**(10), 2281–2306 (2003).
[57]I. Ratas and K. Pyragas, "Macroscopic self-oscillations and aging transition in a network of synaptically coupled quadratic integrate-and-fire neurons," Phys. Rev. E **94**(3), 032215 (2016).
[58]Y. A. Kuznetsov, *Elements of Applied Bifurcation Theory* (Springer-Verlag, New York, 1998).
[59]J. Guckenheimer and Y. Kuznetsov, "Bautin bifurcation," Scholarpedia **2**(5), 1853 (2007).
[60]J. Guckenheimer and Y. Kuznetsov, "Fold-Hopf bifurcation," Scholarpedia **2**(10), 1855 (2007).
[61]C. Bick and E. A. Martens, "Controlling chimeras," New J. Phys. **17**, 033030 (2015).
[62]D. Călugăru, J. F. Totz, E. A. Martens, and H. Engel, "First-order synchronization transition in a large population of strongly coupled relaxation oscillators," Sci. Adv. **6**, eabb2637 (2020).
[63]C. Bick, M. J. Panaggio, and E. A. Martens, "Chaos in Kuramoto oscillator networks," Chaos **28**, 071102 (2018).
[64]I. Ratas and K. Pyragas, "Macroscopic oscillations of a quadratic integrate-and-fire neuron network with global distributed-delay coupling," Phys. Rev. E **98**(5), 052224 (2018).
[65]A. Ceni, S. Olmi, A. Torcini, and D. Angulo-Garcia, "Cross frequency coupling in next generation inhibitory neural mass models," Chaos **30**(5), 053121 (2020).
[66]I. Ratas and K. Pyragas, "Symmetry breaking in two interacting populations of quadratic integrate-and-fire neurons," Phys. Rev. E **96**(4), 042212 (2017).
[67]S. Coombes and Á. Byrne, "Next generation neural mass models," in *Nonlinear Dynamics in Computational Neuroscience* (Springer, 2019), pp. 1–16.
[68]M. Shanahan, "Metastable chimera states in community-structured oscillator networks," Chaos **20**(1), 013108 (2010).
[69]M. Wildie and M. Shanahan, "Metastability and chimera states in modular delay and pulse-coupled oscillator networks," Chaos **22**(4), 043131 (2012).

Article [2] – Graphop Mean-Field Limits and Synchronization for the Stochastic Kuramoto Model

Article [2], entitled *Graphop Mean-Field Limits and Synchronization for the Stochastic Kuramoto Model*, was written in collaboration with Erik A. Martens' partners at the Technical University of Munich, Christian Kuehn and his PhD student Marios A. Gkogkas, whom Benjamin Jüttner visited as an external stay in the final year of his PhD studies. The manuscript was submitted to the journal *Chaos* (AIP publishing) the 31^{st} of March 2022, accepted the 22^{nd} of August 2022 and is scheduled for publication soon. The article also found on arXiv:2203.16839 but the version given in this thesis is more up to date. The article is here attached with permission of *Chaos* (AIP publishing).

The authors of this article are: Marios A. Gkogkas, Benjamin Jüttner, Christian Kuehn, and Erik A. Martens.

Graphop Mean-Field Limits and Synchronization for the Stochastic Kuramoto Model

Marios Antonios Gkogkas,[1] Benjamin Jüttner,[2] Christian Kuehn,[1,3] and Erik Andreas Martens[4,a)]
[1)]*Department of Mathematics, Technical University of Munich, 85748 Garching b. München, Germany*
[2)]*Department of Applied Mathematics and Computer Science, Technical University of Denmark, 2800 Kgs. Lyngby, Denmark*
[3)]*Complexity Science Hub Vienna, 1070 Vienna, Austria*
[4)]*Centre for Mathematical Sciences, Lund University, Sölvegatan 18, 221 00 Lund, Sweden*

(Dated: 7 September 2022)

Models of coupled oscillator networks play an important role in describing collective synchronization dynamics in biological and technological systems. The Kuramoto model describes oscillator's phase evolution and explains the transition from incoherent to coherent oscillations under simplifying assumptions including all-to-all coupling with uniform strength. Real world networks, however, often display heterogeneous connectivity and coupling weights that influence the critical threshold for this transition. We formulate a general mean field theory (Vlasov-Focker Planck equation) for stochastic Kuramoto-type phase oscillator models, valid for coupling graphs/networks with heterogeneous connectivity and coupling strengths, by using graphop theory in the mean field limit. Considering symmetric odd valued coupling functions, we mathematically prove an exact formula for the critical threshold for the incoherence-coherence transition. We numerically test the predicted threshold using large finite-size representations of the network model. For a large class of graph models we find that the numerical tests agree very well with the predicted threshold obtained from mean field theory. However, the prediction is more difficult in practice for graph structures that are sufficiently sparse. Our findings open future research avenues towards a deeper understanding of mean-field theories for heterogeneous systems.

Keywords: Kuramoto model, phase oscillators, synchronization, heterogeneous graph, mean-field limit, graphop.

Networks of coupled oscillators appear in an impressive range of systems in nature and technology where they display collective dynamics such as synchronization [1–3]. The Kuramoto model describes the phase evolution of oscillators[4,5] and explains the transition from incoherent to coherent synchronized oscillations for a critical threshold of the coupling strength under simplifying assumptions such as all-to-all coupling with uniform strength[6,7]; however, real world networks often display strong heterogeneity in connectivity and coupling strength which affect the critical threshold[8]. We derive a mean field theory for stochastic Kuramoto-type models and extend it to a large class of heterogeneous graph/network structures via graphop descriptions valid for the mean-field limit. We prove a mathematically exact formula for the critical threshold, which we test numerically for large finite-size representations of the network model.

I. INTRODUCTION

The discovery of synchronization dates back to 1665 with Christiaan Huygens' observations of two synchronizing pendulum clocks[9], and its mathematical modeling likely began with Norbert Wiener who was inspired by neuronal oscillations in the brain[10]. Wiener's formulation of the problem, however, was too general to allow for any analytical progress; simplifying assumptions were necessary to render the problem mathematically tractable[11], culminating in Yoshiki Kuramoto's paradigmatic model[4,5]. Kuramoto's original model describes the time evolution of the oscillator phases $\theta_k = \theta_k(t)$,

$$\frac{\mathrm{d}}{\mathrm{d}t}\theta_k =: \dot{\theta}_k = \omega_k + \frac{C}{N}\sum_{j=1}^{N}\sin(\theta_j - \theta_k),$$

where $k \in \{1,\dots N\} =: [N]$, the coupling interaction between oscillators is first order, the coupling is all-to-all with uniform strength C, and the intrinsic frequencies ω_k are drawn unimodally from a distribution g centered in the origin. The level of synchronization in this transition is aptly captured using the order parameter, $r(t) = \frac{1}{N}\left|\sum_{j=1}^{N}\exp\left(\mathrm{i}\theta_j(t)\right)\right|$, which tends to 0 when oscillator phases are incoherent (disordered) for weak coupling; or to 1 when oscillators lock their frequencies and phases clump together (we say the phases are coherent / the oscillators synchronize). When frequencies are identical, $\omega_k = \omega_j$ for all $k, j \in [N]$, the so-called synchronization manifold defined by $\theta_k(t) = \theta_j(t)$ for all $k, j \in [N]$ exists and is attractive for $C > 0$; vice versa, when frequencies are non-identical (or symmetry is broken due to some other mechanism, see below), the loss or gain of coherence plays out in a competition between the strength of the heterogeneity and coupling strength C. Thus, for a set distribution width of the intrinsic frequencies, Kuramoto's model exhibits a transition from incoherent to coherent oscillations as the coupling strength C surpasses a certain threshold value $C^{\natural}$.

[a)]Corresponding author: erik.martens@math.lth.se

Kuramoto's initial heuristic analysis was based on a self-consistency equation for the order parameter[12], allowing to predict the critical coupling strength associated with the incoherence-coherence transition. A more formal mathematical treatment, facilitating deeper insights would however require a mean field theory valid in the limit, $N \to \infty$. Such a theory[13] describes the dynamics in terms of a density function in the oscillator phases, $\rho = \rho(\phi,t)$, that evolves according to a transport equation (formally, a Vlasov-Fokker-Planck equation, see Eq. (8)). Such a description was used by Strogatz and Mirollo[14] to investigate the stability of the incoherent branch for $C < C^\natural$ where $\rho = 1/(2\pi)$ by studying the associated eigenvalue spectrum, and to (re-)derive the critical coupling $C^\natural = 2/(\pi g(0))$, where $g(0)$ denotes the maximum value of a unimodal frequency distribution g; this approach was further developed and applied to variants of the Kuramoto model[15]. Other studies focused on the stability analysis for the partially synchronized branch ($C > C^\natural$)[16]. An exact low dimensional description in terms of the macroscopic dynamics (order parameter) allowing to express the evolution of the order parameter in terms of an ordinary differential equation became available later [17–19].

While Kuramoto's simplifying assumptions allowed for making significant progress in the mathematical understanding of the synchronization phenomenon, to understand real world oscillator dynamics, it is desirable to break these assumptions towards increasing complexity. There is a number of ways of doing this; here, we are concerned with how the incoherence-coherence transition is affected by the presence of (thermal) noise and in particular, network heterogeneities, which play a major role in real systems[20–27]. Indeed, the ability of coupled oscillators to synchronize has been investigated under the influence of noise[12,28], heterogeneous connectivity[29,30] or heterogeneous coupling, such as non-local[31,32], k-nearest-neighbor[33], or random coupling strengths[34,35]); and also on experiments[36–39] where oscillators are subject to real world influences.

Mean-field descriptions for $N \to \infty$ are well established for various theoretical frameworks including coupled oscillator networks[13]. Our focus thus lies on mean-field limits valid for complex networks[8], i.e., to generalize the Vlasov-Fokker-Planck (VFPE) equation (see Eq. (8)) so that it is capable of accurately describing the dynamics in complex networks characterized by heterogeneities in the connectivity or coupling strength. In particular, this includes cases where the adjacency matrix defining interactions between finitely many vertices is neither a full graph or a highly symmetric structure such as a lattice. In order to incorporate such structures, it is necessary to extend the description of (weighted) graph structures to the mean-field limit. This is possible via so-called graphons, which rely on concepts of the theory of limits of graph sequences[40,41], or even more generally utilizing the theory of graphops[42]. Intuitively, graph limit theory provides a way to arrange limits of discrete graphs as continuous objects. Graphons achieve this, mostly within the context of dense graphs, using a coupling kernel function that describes the connectivity in the limit. Graphops generalize graphons, also incorporating many intermediate and sparse density graph limits in addition. Graphops can be represented as operators or via an associated measure-theoretic representation, i.e., they are generalizing purely kernel-based operators to more general operators. Recent studies have used graph limit theories to pursue the goal of heterogeneous mean-field limits. Several mathematical approaches have been successful in providing rigorous proofs for VFPEs, where nonlocal integral terms appear to take into account the heterogeneous coupling structure[43,44]. Recently, a general theoretical framework based on graphops has been put forward (by some of the authors of this paper) that allows us to generalize easily from particular cases (nonlocal coupling or standard all-to-all) mean-field limit VFPEs, to describe modern complex network structures[45–48].

In the present paper, we extend previous work[45–47] to the stochastic case and formally derive a mean-field for what we below denote the *classical Kuramoto model*, i.e., the Kuramoto model with identical oscillators under the influence of (thermal) noise, based on graphop theory. We then derive rigorous results for the critical threshold for the incoherence-coherence transition ($C^\natural$) by deriving a stability formula for the incoherent solution branch. A difficulty arises as it is unclear what demarcates the boundary of validity for mean-field PDEs valid for complex heterogeneous graphs, i.e., at some level of graph heterogeneity it may be too difficult to accurately capture details of very sparse graph structures. As we cannot be sure under what circumstances our results correspond to the dynamics obtained for finite graphs (rigorous convergence results are still needed), we carry out detailed numerical simulations to test our results for various finite graph structures.

The article is structured as follows. In the next section, we introduce a formal derivation of the mean-field equations for $N \to \infty$. In Sec. III, we derive the critical coupling strength $C^\natural$ for the continuum limit, based on the graphop mean-field limit equation. In Sec. IV, we carry out numerical simulations to investigate how the incoherence-coherence transition point predicted by the mean-field theory carries over to finite graphs for a range of graph structures, including dense and sparse topologies. Finally, we discuss our results in Sec. V.

II. FORMAL DERIVATION OF THE MEAN-FIELD EQUATIONS

As discussed above, we are interested in mean-field models for stochastic Kuramoto(-type) models on networks[49]. The individual dynamics for the coupled identical oscillators is given by

$$\frac{\mathrm{d}\theta_k^N}{\mathrm{d}t} =: \dot{\theta}_k^N = \frac{C}{N}\sum_{j=1}^{N} A_{kj}^N D(\theta_j^N - \theta_k^N) + \sqrt{2\beta^{-1}}\dot{W}_k, \qquad (1)$$

where $k \in [N] := \{1,...,N\}$ and $\theta_k = \theta_k(t) \in \mathbb{T} := \mathbb{R}/(2\pi\mathbb{Z})$ denotes the phase of the k-th oscillator, $(A_{k,j}^N)_{k,j\in[N]}$ denotes a weighted and non-negative adjacency matrix of the network (i.e., a graph G with adjacency matrix A_{kj}^N), $D : \mathbb{T} \to \mathbb{R}$ is a sufficiently regular coupling function (e.g., classically $D = \sin$),

$C > 0$ is the coupling strength, $\beta > 0$ a diffusion constant controlling the noise level, and $W(t) = (W_1(t), \dots, W_N(t))^\top$ is vector of N independent Brownian motions so that $\dot{W}_k = \dot{W}_k(t)$ is just a white noise forcing for each oscillator. The following derivation extends[45] to the stochastic case. To understand the formal derivation, let us recall the classical Kuramoto all-to-all coupled case, i.e., for $A^N_{k,j} = 1$ for all $k, j \in [N]$ and $D = \sin$. In other words, (1) now reads as

$$\dot{\theta}^N_k = \frac{C}{N} \sum_{j=1}^{N} \sin(\theta^N_j - \theta^N_k) + \sqrt{2\beta^{-1}}\dot{W}_k, \quad k \in [N]. \tag{2}$$

Let us introduce the complex order parameter

$$r\mathrm{e}^{\mathrm{i}\psi} := \frac{1}{N} \sum_{j=1}^{N} \mathrm{e}^{\mathrm{i}\theta_j}. \tag{3}$$

Multiplying this equation by $\mathrm{e}^{-\mathrm{i}\theta_k}$ and equating imaginary parts we have

$$r \sin(\psi - \theta_k) = \frac{1}{N} \sum_{j=1}^{N} \sin(\theta^N_j - \theta^N_k) \tag{4}$$

which implies that

$$\dot{\theta}^N_k = Cr \sin(\psi - \theta_k) + \sqrt{2\beta^{-1}}\dot{W}_k, \quad k \in [N]. \tag{5}$$

From (5) the mean-field character of the problem is visible as the k-th oscillator just feels the averaged input from all other oscillators so one can think of a single typical oscillator and aim to analyze its dynamics. Let $\rho(t,\theta)\,\mathrm{d}\theta$ denote the fraction of oscillators with phase between θ and $\theta + \mathrm{d}\theta$ at time t, i.e., ρ is a probability density. Assuming a law of large numbers in the limit $N \to \infty$ we formally get

$$r\mathrm{e}^{\mathrm{i}\psi} = \frac{1}{N} \sum_{j=1}^{N} \mathrm{e}^{\mathrm{i}\theta_j} \to \int_0^{2\pi} \mathrm{e}^{\mathrm{i}\phi} \rho(t,\phi)\,\mathrm{d}\phi \tag{6}$$

Now, using the same trick as above (i.e., multiplying both sides of last equation by $\mathrm{e}^{-\mathrm{i}u}$ and taking imaginary parts), equation (5) becomes in the limit $N \to \infty$

$$\dot{u} = C \int_0^{2\pi} \sin(\phi - u)\rho(t,\phi)\,\mathrm{d}\phi + \sqrt{2\beta^{-1}}\dot{W}. \tag{7}$$

Finally, the continuity equation, also called Vlasov-Fokker-Planck equation (VFPE), for the probability density ρ, respectively for the law of the limiting process u, reads as

$$\begin{aligned} \partial_t \rho &= -\partial_\theta \Big(\rho V(\rho) \Big) + \frac{1}{\beta} \partial^2_\theta \rho, \\ V(\rho) &:= C \int_0^{2\pi} \sin(\phi - \theta) \rho(t,\phi)\,\mathrm{d}\phi. \end{aligned} \tag{8}$$

In summary, (8) is a partial differential equation with a first-order transport/advection-type term with a nonlocal convolution term involving the sine-nonlinearity mediating the coupling and with a second-order spatial diffusion term arising directly from the white noise forcing.

Now, let us come back to equation (1). In this case the next natural generalization step is to assume that the network (i.e., a graph G with adjacency matrix A^N_{kj}) is sufficiently connected and does not have components, which are more connected than others; see also[49]. Moreover, we assume that there exists a local order parameter $r_k \mathrm{e}^{\mathrm{i}\psi_k}$, which is locally proportional to a single global order parameter $r\mathrm{e}^{\mathrm{i}\psi}$ weighted by the degree κ_k for each node, i.e., we have

$$\kappa_k r\mathrm{e}^{\mathrm{i}\psi} = r_k \mathrm{e}^{\mathrm{i}\psi_k} := \sum_{j=1}^{N} A_{kj} \mathrm{e}^{\mathrm{i}\theta_j}. \tag{9}$$

By multiplying the local order parameter by $\mathrm{e}^{-\mathrm{i}\theta_k}$ and equating the imaginary parts in last equation we obtain

$$\dot{\theta}^N_k = C\, r\, \kappa_k \sin(\psi - \theta_k) + \sqrt{2\beta^{-1}}\dot{W}_k, \quad k \in [N]. \tag{10}$$

Now let $\rho(t,\theta,\kappa)\,\mathrm{d}\theta$ denote the probability which gives the fraction of oscillators with phase between θ and $\theta + \mathrm{d}\theta$ and degree κ at time t. Note carefully that we have added an additional variable κ to the density, which captures the (degree) heterogeneity of the network. If we assume that the network is uncorrelated and has degree distribution $d(\kappa)$, one is tempted to assume that in the limit $N \to \infty$ we have

$$r\mathrm{e}^{\mathrm{i}\psi} = \frac{1}{\kappa_k} \sum_{j=1}^{N} A_{kj} \mathrm{e}^{\mathrm{i}\theta_j} \to \int_0^{2\pi} \int_0^{\infty} \mathrm{e}^{\mathrm{i}\phi} \frac{\kappa d(\kappa)}{\langle \kappa \rangle} \rho(t,\phi,\kappa)\,\mathrm{d}\kappa\,\mathrm{d}\phi, \tag{11}$$

where $\langle \kappa \rangle$ is the average degree of a vertex in the graph and $\frac{\kappa d(\kappa)}{\langle \kappa \rangle} \rho(t,\phi,\kappa)$ is the probability density for an edge having its end at a vertex of phase ϕ and degree κ at time t. Now using the same trick as before, equation (10) becomes in the limit $N \to \infty$

$$\dot{u} = \frac{C}{\langle \kappa \rangle} \int_0^{2\pi} \int_0^{\infty} \sin(\phi - u)\, l\, d(l)\, \rho(t,\phi,l)\,\mathrm{d}\phi\,\mathrm{d}l + \sqrt{2\beta^{-1}}\dot{W}. \tag{12}$$

The continuity equation for the probability density ρ, respectively, the law of the limiting process u, reads as

$$\partial_t \rho = -\partial_\theta \Big(\rho V[G](\rho) \Big) + \frac{1}{\beta} \partial^2_\theta \rho, \tag{13a}$$

$$V[G](\rho) := \frac{C}{\langle \kappa \rangle} \int_0^{2\pi} \int_0^{\infty} \sin(\phi - \theta)\, l\, d(l)\, \rho(t,\phi,l)\,\mathrm{d}\phi\,\mathrm{d}l. \tag{13b}$$

Thus, in comparison to the classical all-to-all coupled VFPE (8) we had to replace

$$\rho(t,\phi) \quad \text{by} \quad \int_0^{\infty} \frac{l d(l)}{\langle l \rangle} \rho(t,\phi,l)\,\mathrm{d}l. \tag{14}$$

We can view this step as incorporating the structure of graph/network G appearing in the Vlasov equation via an operator, which acts in the density ρ. In fact, one can even hope to completely remove averaging over the variable κ that we used to capture the heterogeneity and just keep κ as a new variable in the density, which then yields a whole hierarchy of

mean-field VFPEs, one for each degree. This set of ideas can then be thought even further and one can directly replace the adjacency matrix by a coupling kernel and there are numerous papers in this direction[43,44,46,47]. Yet, it seems best to think of generalizing VFPEs more abstractly[45] by viewing the underlying network influence as given by some linear operator A acting on the density so that a more abstract form of VFPEs would be given by

$$\partial_t \rho = -\partial_\theta \Big(\rho V[A](\rho) \Big) + \frac{1}{\beta} \partial_\theta^2 \rho, \tag{15a}$$

$$V[A](\rho) = C \int_0^{2\pi} D(\phi - \theta)(A\rho)(t,\phi,x)\, \mathrm{d}\phi, \tag{15b}$$

where x is a suitable variable that tracks the heterogeneity of the network so that one effectively obtains a family of VFPEs, and we have also replaced the sine-coupling again by a more general coupling function D. A typical choice of x found in the literature would be to take it as a variable in the unit interval $x \in [0,1] = \Omega$, where points in the interval represent node labels in the infinite network limit [43,44,46,47]. Probably the most elegant abstract way to think of A is as a graph operator, or graphop, as introduced in[42]. A graphop is a bounded, self-adjoint and positivity-preserving operator $A : L^\infty(\Omega; m) \to L^1(\Omega; m)$, where m is the reference measure on Ω, e.g., one can pick the Lebesgue measure. To a given graphop A always corresponds a family of finite measures $(\nu_x)_{x\in\Omega}$, called fiber measures, via the formula

$$(Af)(x) = \int_\Omega f(y)\, \mathrm{d}\nu_x(y) \quad x \in \Omega, \quad \text{for } f \in L^\infty(\Omega; m).$$

Intuitively we may view a graphop A just as a generalized adjacency matrix for a symmetric graph and for a given node $x \in \Omega$ the fiber measure ν_x is just the edge distribution for this node. Indeed, for the finite-dimensional case, we can just pick $\Omega = [N]$ and m as the uniform measure on Ω, so that functions $f \in L^\infty(\Omega; m)$ can be identified with vectors in $\mathbb{R}^N$ and Af is just usual matrix-vector multiplication. Yet, we stress that in the limit $N \to \infty$, we need a space such as $\Omega = [0,1]$ with the Lebesgue measure.

One may wonder, how far such an abstract construction for VFPEs involving graphops can work? It is clear that it works in simple cases, e.g., when the graph is all-to-all coupled as one can just drop the dependence on x and let $A = 1$. Also, if the graph is very dense and very regular with just two types of typical nodes, then one could take x as a binary variable, and so on. Furthermore, it is understood that it works for dense graphs, where A can be represented by an integral operator with a sufficiently regular kernel, i.e., in the framework of so-called graphons. However, one does expect that there are growing networks as $N \to \infty$ that are so sparse and/or so heterogeneous that eventually mean-field calculations may fail. Proving a precise boundary location on the space of networks to determine, when VFPEs are helpful and when they fail, seems out of reach at this point. Here we take a pragmatic approach and start from the formal VFPE (15a), carry out stability analysis of the main bifurcation/phase transition to synchronization in the Kuramoto model, and then numerically simulate the dynamics for different discretized (i.e., finite-dimensional, large N) classes of graphops A to check, when the mean-field stability calculation is accurate. This is going to provide an indirect cross-check, whether a mean-field limit can work.

III. BIFURCATION/PHASE TRANSITION

In the following, we consider (15a) and we assume for simplicity that

(H0) The coupling is non-trivial, i.e., $C > 0$.

(H1) D is an odd 2π-periodic function.

(H2) A is a graphop with bounded $2 \to 2$ norm, i.e., the following quantity exists and is finite

$$\| A \|_{2\to 2} := \sup_{v \in L^2(\Omega)} \frac{\| Av \|_2}{\| v \|_2} < \infty.$$

This implies that A can be uniquely extended to the Hilbert space $L^2(\Omega, m)$ (see[42] (Remark 2.12) for instance). For simplicity we use the same notation for this extension, i.e., we write $A : L^2(\Omega, m) \to L^2(\Omega, m)$. For the solution $\rho(t, \theta, x)$ of (15a) we define the j-th Fourier coefficient as

$$z_j = \frac{1}{2\pi} \int_0^{2\pi} \mathrm{e}^{-\mathrm{i}j\theta} \rho(t, \theta, x)\, \mathrm{d}\theta, \quad j \in \mathbb{Z} \tag{16}$$

where $\mathrm{i} := \sqrt{-1}$. Note that we have effectively defined a family of Fourier coefficients that depends upon x, i.e., $\{(z_j)_x\}_{x\in\Omega}$ but we shall always write just z_j in the calculation below and later discuss the x-dependence. Applying the Fourier transform to (15a), exchanging integrals and using integration-by-parts (in the second line) we have

$$
\begin{aligned}
\partial_t z_j &= \frac{1}{2\pi}\int_{\mathbb{T}} \mathrm{e}^{-\mathrm{i}j\theta}\Big(\partial_\theta\{\rho(t,\theta,x)V[A](\rho)(t,\theta,x)\}+\frac{1}{\beta}\partial_\theta^2\rho(t,\theta,x)\Big)\,\mathrm{d}\theta \\
&= \frac{1}{2\pi}\Big(\mathrm{i}jC\int_{\mathbb{T}}\mathrm{e}^{-\mathrm{i}j\theta}\rho(t,\theta,x)\int_{\mathbb{T}}(A\rho)(t,\phi,x)D(\phi-\theta)\,\mathrm{d}\phi\,\mathrm{d}\theta-\frac{j^2}{\beta}\underbrace{\int_{\mathbb{T}}\mathrm{e}^{-\mathrm{i}j\phi}\rho(t,\phi,x)\,\mathrm{d}\phi}_{=z_j}\Big) \\
&= \frac{1}{2\pi}\Big(\mathrm{i}jC\sum_{l\in\mathbb{Z}}\hat{D}(l)\int_{\mathbb{T}}\mathrm{e}^{\mathrm{i}(-j-l)\theta}\rho(t,\theta,x)\int_{\mathbb{T}}(A\rho)(t,\phi,x)\mathrm{e}^{\mathrm{i}l\phi}\,\mathrm{d}\phi\,\mathrm{d}\theta-\frac{j^2}{\beta}z_j\Big) \\
&= \frac{1}{2\pi}\Big(\mathrm{i}jC\sum_{l\in\mathbb{Z}\setminus\{0\}}\hat{D}(l)z_{-j-l}Az_{-l}-\frac{j^2}{\beta}z_j\Big),
\end{aligned}
\tag{17}
$$

where $\hat{D}$ denotes the Fourier transform of D and in the last line we used that $\hat{D}(0)=0$, which follows from the fact that D is an odd, periodic function. Moreover, $z_{-j}=\overline{z_j}$ holds, which follows from the fact that ρ is real-valued. We can assume without loss of generality that $j\in\mathbb{N}$ to get the following system (i.e., the amplitude equation)

$$
\partial_t z_j = \frac{1}{2\pi}\Big\{\Big(\mathrm{i}C\hat{D}(-j)A-\frac{j^2}{\beta}\Big)z_j+\mathrm{i}jC\sum_{l\in\mathbb{Z},l\neq 0,-j}\hat{D}(l)z_{-j-l}Az_{-l}\Big\},\quad j=1,2,\ldots \tag{18}
$$

The completely incoherent state $\rho_\infty\equiv 1$ of the oscillators corresponds to a uniform probability density over the circle, which translates into $z_0=1$ and $z_j=0$ for all $j\neq 0$ and the state is also assumed to be independent of x, i.e., we assume all different types of nodes are uniformly distributed across the circle for ρ_∞. Linearizing (18) around this incoherent state yields via a straightforward calculation the system

$$
\partial_t Z_j = \frac{1}{2\pi}\Big\{\Big(\mathrm{i}C\hat{D}(-j)A-\frac{j^2}{\beta}\Big)Z_j\Big\},\quad j=1,2,\ldots \tag{19a}
$$

where we use Z_j to denote the Fourier coefficients of the linearized dynamical system and we observe that the linearized system nicely decouples. The question then is: how does the stability of the j-th Fourier mode depend on the eigenvalues of graphop A? On the Hilbert space $H:=L^2(\Omega,m)$, for any $j\in\mathbb{N}$, let us define the linearized operator $T_C^j:H\to H$,

$$
T_C^j w := \frac{1}{2\pi}\Big(\mathrm{i}C\hat{D}(-j)A-\frac{j^2}{\beta}\Big)w.
$$

Recall that the resolvent set $\rho(A)$ of the operator $A:H\to H$ is defined to be the set

$$
\begin{aligned}
\rho(A) := \{\lambda\in\mathbb{C} : R_\lambda(A) &:= (A-\lambda I)^{-1}: \\
&H\to H \text{ exists and is bounded}\}
\end{aligned}
$$

where $R_\lambda(A)$ is called the resolvent operator of A and the spectrum of A is the complement $\sigma(A):=\mathbb{C}\setminus\rho(A)$. Observe that for any $\lambda\in\mathbb{C}$, setting $\tilde{\lambda}:=\frac{1}{2\pi}(\mathrm{i}C\hat{D}(-j)\lambda-\frac{j^2}{\beta})$ we have

$$
R_{\tilde{\lambda}}(T_C^j)=\frac{1}{2\pi}\mathrm{i}C\hat{D}(-j)R_\lambda(A),
$$

From this we see that for all j for which $\hat{D}(-j)\neq 0$, the condition that $R_\lambda(A)$ exists and is bounded is equivalent to the condition that $R_{\tilde{\lambda}}(T_C^j)$ exists and is bounded. From this we conclude that for all $j\in\mathbb{Z}$ for which $\hat{D}(-j)\neq 0$ we have

$$
\sigma(T_C^j)=\frac{1}{2\pi}\Big(\mathrm{i}C\hat{D}(-j)\sigma(A)-\frac{j^2}{\beta}\Big).
$$

For all other $j\in\mathbb{Z}$ (that is, for all j for which $\hat{D}(-j)=0$) we see immediately that $\sigma(T_C^j)=-\frac{j^2}{\beta 2\pi}$. Since A is bounded and self-adjoint we have that $\sigma(A)\subset\mathbb{R}$ is a bounded set. Further note that, since D is an odd function, we must have $\hat{D}(j)=\mathrm{i}\int_0^{2\pi}D(u)\sin(ju)\mathrm{d}u\in\mathrm{i}\mathbb{R}$. Finally define

$$
C^\natural := \inf\Big\{\frac{j^2}{\beta\mathrm{i}\hat{D}(j)\lambda} : \lambda\in\sigma(A),\ j\in\mathbb{Z}^*,\ \mathrm{i}\hat{D}(j)\lambda\geq 0\Big\}. \tag{20}
$$

where $\mathbb{Z}^*:=\mathbb{Z}^+\cup\{0\}$. The next theorem shows that $C^\natural$ is a uniform parameter bound on the coupling strength independent of x, which means that smaller coupling leads to stability of incoherence, while above $C^\natural$, at least some classes of nodes synchronize at least partially. More precisely we have:

Theorem III.1. ***(Incoherence-coherence transition)*** *Consider an odd, 1-periodic, continuous function $D:[0,1]\to\mathbb{R}$ and a graphop $A:L^2(\Omega,m)\to L^2(\Omega,m)$. Then, the incoherent state ρ_∞ is locally asymptotically stable for $0<C<C^\natural$ and unstable for $C>C^\natural$.*

Proof. Observe that for any $\lambda\in\sigma(A)$ and $j\in\mathbb{Z}^*$, such that $\mathrm{i}\hat{D}(-j)\lambda<0$, the corresponding element in the spectrum of

T_C^j, $\tilde{\lambda}(C,j) = \frac{1}{2\pi}(\mathrm{i}C\hat{D}(-j)\lambda - \frac{j^2}{\beta}) \in \sigma(T_C^j)$, is strictly negative for any $C > 0$, thus it never crosses the imaginary axis. Thus, a crossing, for growing C, can occur only among those $\lambda \in \sigma(A)$ and $j \in \mathbb{Z}^*$ for which $\mathrm{i}\hat{D}(-j)\lambda > 0$. Among all such λ and j, the crossing occurs always at

$$C_{j,\lambda} := \frac{j^2}{\beta \mathrm{i}\hat{D}(-j)\lambda}. \tag{21}$$

Observing that $C^\natural$ is the minimum of all these transition points, it follows immediately that $C^\natural$ is the smallest $C > 0$ for which there exists a $j \in \mathbb{N}$ such that an element in the spectrum of T_C^j crosses the imaginary axis, namely the element $\tilde{\lambda}(C^\natural, j) \in \sigma(T_{C^\natural}^j)$. □

As a first step, we want to carry out some specializations to examples and analytically consider some cases.

Example III.2. (Classical Kuramoto model)
First, we want to specialize the general formula to the classical Kuramoto model in Eq. (15a) (the continuum limit version of Eq. (1)). In this context, we have $D : [0, 2\pi] \to \mathbb{R}$ given by $D(u) := \sin(u)$. Hence,

$$\begin{aligned} \hat{D}(1) &= \frac{1}{2\pi}\int_0^{2\pi} \sin(u)\mathrm{e}^{\mathrm{i}u}\,\mathrm{d}u = \frac{\mathrm{i}}{2} \\ \hat{D}(-1) &= -\frac{\mathrm{i}}{2} \\ \hat{D}(k) &= 0, \quad k \in \mathbb{Z}\setminus\{1,-1\} \end{aligned}$$

and $\mathrm{i}\hat{D}(-1) = \frac{1}{2} > 0$. Then, by Theorem III.1, the incoherent state loses stability at

$$C^\natural = \frac{2}{\beta\Lambda(A)}, \ \Lambda(A) := \sup_{\lambda\in\sigma(A)} |\lambda|. \tag{22}$$

Example III.3. (Full graph)
In the case of the *full graph* (i.e., complete graph with uniform coupling strength) we have

$$Af(x) = \int_\Omega f(y)\,\mathrm{d}m(y), \quad x \in \Omega, f \in L^2(\Omega, m).$$

Clearly, A is a non-invertible operator and the only eigenvalue of A is 1 (The eigenvalue equation $Af = \lambda f$ implies that f must be a constant, say $f_0 \neq 0$, satisfying $f_0 = \lambda f_0$. Thus, $\lambda = 1$.) Moreover, in the case that $\lambda \in \mathbb{C}\setminus\{0,1\}$, the operator $A - \lambda I$ is invertible, since for any $g \in L^2(\Omega, m)$ the pre-image f is achieved under the unique choice

$$f := \frac{\frac{c}{1-\lambda} - g}{\lambda}, \quad c := \int_\Omega g(y)\,\mathrm{d}m(y).$$

Thus we have $\sigma(A) = \{0,1\}$. Hence, for the classical Kuramoto model on the full graph we obtain by the previous Example III.2 that

$$C^\natural = \frac{2}{\beta}. \tag{23}$$

Remark III.4. *Sakaguchi*[50] *obtained for the critical coupling of the full graph the formula (in Sakaguchi's notation)*

$$K_C(D) = 2\Big(\int_{-\infty}^{\infty} \frac{1}{\omega^2+1} g(D\omega + \omega_0)\,\mathrm{d}\omega\Big)^{-1}. \tag{24}$$

In our framework, matching the assumptions and the notation correctly, we have $\omega_0 = 0$, $D = \frac{1}{\beta}$ and $g = \delta_0$. Note that in Sakaguchi's framework the variance of the Brownian term $f_i(t)$ is $2Dt$, while in our framework the Brownian term $\sqrt{2\beta^{-1}}W_k$ has variance $\frac{2}{\beta}t$ for each k, thus we must have $D = \frac{1}{\beta}$). Thus Sakaguchi's formula simplifies to

$$\begin{aligned} K_C(D) &= 2\Big(\int_{-\infty}^{\infty} \frac{1}{\omega^2+1} g(D\omega)\,\mathrm{d}\omega\Big)^{-1} \\ &= 2\Big(\frac{1}{D}\int_{-\infty}^{\infty} \frac{1}{\left(\frac{x}{D}\right)^2+1}\,\mathrm{d}\delta_0(x)\Big)^{-1} \\ &= 2D = \frac{2}{\beta} = C^\natural, \end{aligned} \tag{25}$$

which is exactly just the special case of the far more general formula we calculated in Example III.3.

Although we have now a very nice formula for $C^\natural$, it is not immediately clear for which classes of networks this formula works as $N \to \infty$. After all, Theorem III.1 only makes claims about stability/instability based upon the assumption of the validity of the mean-field VFPE. Only if we already knew that the mean-field limit VFPE would be valid for certain classes of networks, i.e., if it does approximate — in a suitable sense — the oscillator system for finite but large N, then we could be certain applying our result for finite large networks. Proving such an approximation result in full generality is difficult although first steps exist for the deterministic Vlasov case [43,44,46,47]. For example, one issue in this context is that the mean-field only holds in a scaling limit upon renormalizing the sums appearing in the Kuramoto-model suitably via the density of the graph. However, empirically testing the formula for $C^\natural$ via various classes of large finite networks using numerical simulation is certainly possible and we shall proceed with this approach.

IV. INCOHERENCE-COHERENCE TRANSITION FOR FINITE AND INFINITE OSCILLATOR NETWORKS

We want to check the prediction for the incoherence-coherence transition given in Theorem III.1 for the mean-field limit by numerical simulations. The challenges we face in doing so stem from the fact that numerical simulations are bound to a finite-dimensional representation of Eq. (1) and to a finite simulation time. Thus, while Theorem III.1 can only hold in an approximative sense for $N < \infty$, the finite system size and simulation time also incur uncertainty in the detection of the incoherence-coherence transition. Several points need to be taken into account when detecting the transition from incoherence to coherence that we outline below.

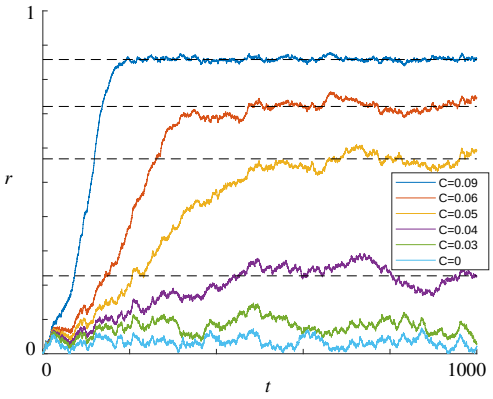

FIG. 1. Time evolution of r for numerical solutions of (2), for different values of C. Clearly, the time traces of r are subject to (random) fluctuations. Also, for higher C, the time traces of r settle, after a transient, at some quasi-stationary state (dashed lines). Other parameters are $\beta = 50$ and $N = 1000$.

To see this, it is instructive to observe the dynamics for the simple case of the classical Kuramoto model, i.e., where oscillators interact with $D(u) = \sin(u)$ on a complete graph with uniform coupling. The collective dynamics of all oscillators is described by the order parameter $r(t)$ defined in (3) and is shown in Fig. 1 for numerical solutions of (2) for varying coupling strengths C and fixed system size $N = 1000$ and noise level $\beta = 50$. Initial phases are chosen to correspond to incoherent oscillations (see Sec. IV A on numerical methods). The dynamics of the order parameter r is subject to fluctuations, which stems from two sources: i) the stochastic dynamics inherent to the system; ii) finite size effects induce pseudo-random fluctuations of order $\mathcal{O}(N^{-1/2})$ that vanish in the limit $N \to \infty$[51]. After a transient time, T_{tr}, we observe that the dynamics settle into a quasi-stationary state (on average), i.e., the order parameter fluctuates around a constant mean value and is bounded by minimal and maximal values. If the trajectory after the transient attains a minimal value arbitrarily close to 0 during the observed time interval, we say that the population oscillates incoherently; if the minimal value never approaches 0, the dynamics are said to be (partially) coherent or synchronized (perfect synchrony occurs only for $r = 1$), and we observe increasing synchrony for larger C. Accordingly, Fig. 1 allows us to distinguish incoherent oscillations for weak coupling strengths ($C = 0$ to $C = 0.03$), and partially coherent oscillations occur for stronger coupling ($C \geq 0.04$), which agrees well with the prediction of $C^\natural = 0.04$ given by (23) for the continuum limit. For further details on the incoherence-coherence transition of the Kuramoto model see also Ref. 6. The observations described above point towards an implementation of numerical methods and measurements as outlined below.

A. Numerical methods

We calculate numerical solutions of (1) with a first-order Euler-Maruyama scheme with a time step $\Delta t = 0.01$. Initial conditions/phases correspond to low synchrony compliant with incoherence, i.e., either the equidistant state $\theta_k(0) := 2\pi k/N$ (Uniform complete graph, Erdös-Rényi graph, Regular ring lattice with $r = 400$, Spherical graph) or the random state where $\theta_k(0)$ (Regular ring lattice with $r = 25$, Sinuisodal graph, Lorentzian graph) is drawn from the uniform distribution on the interval $[0, 2\pi)$ (two types of initial conditions were chosen since other attracting states were present for the Regular ring lattice with $r = 25$). To characterize the post-transient dynamics we use the order parameter $r(t) = \left| \frac{1}{N} \sum_{j=1}^{N} e^{\mathrm{i}\theta_j(t)} \right|$ in Eq. (3) and measure its temporal minimum and maximum, as well as its time average,

$$r_{\min} := \min_{t \in \mathscr{T}} (r(t)), \tag{26}$$

$$r_{\max} := \max_{t \in \mathscr{T}} (r(t)), \tag{27}$$

$$\bar{r} := |\mathscr{T}|^{-1} \int_{\mathscr{T}} r(t) \mathrm{d}t, \tag{28}$$

where $\mathscr{T} := [T_{\text{tr}}, T]$ with T_{tr} being the (estimated) transient time and T the total length of the simulation.

To average over stochastic effects such as Brownian motion and random graphs (Erdös-Rényi, Small-World), we average these measurements over several realizations of solutions of (2) (i.e., ten realizations to account for Brownian motion for eight (random) graph realizations) and denote ensemble averages with angular brackets $\langle \cdot \rangle$. To numerically test Theorem III.1, we calculate $\langle r_{\min} \rangle$, $\langle \bar{r} \rangle$, and $\langle r_{\max} \rangle$ for different values of C and compare the resulting curves with $C^\natural$. The sampling points for the coupling C are non-uniformly spaced with higher density in regions of interest (indicated as blue dots in Fig. 2).

A suitable transient time T_{tr} can be determined based on the following considerations. The actual transient is maximal for $C = C^\natural$ and decreases for $C > C^\natural$, see Fig. 1. One could estimate T_{tr} for each value of C individually to optimize for computational effort; but for simplicity, we estimated the length of T_{tr} only at $C = C^\natural$ and used this T_{tr} for all probed values of C, as this choice guarantees a sufficiently long transient time. Due to the fluctuations present in the signal of $r(t)$ (pseudo-random fluctuations and stochastic noise), the estimation of T_{tr} is heuristic, i.e., it is done by visual inspection. This estimate of T_{tr} improves with increasing N as the amplitude of (pseudo-random) fluctuations decreases. Taking these considerations into account we chose $T_{\text{tr}} = 700, T = 1000, \Delta t = 0.01, N = 1000$ for all our numerical solutions of (2).

B. Graph(on) topologies and their associated incoherence-coherence transitions

We now define different graph structures for which we carry out numerical simulations to test for the on-

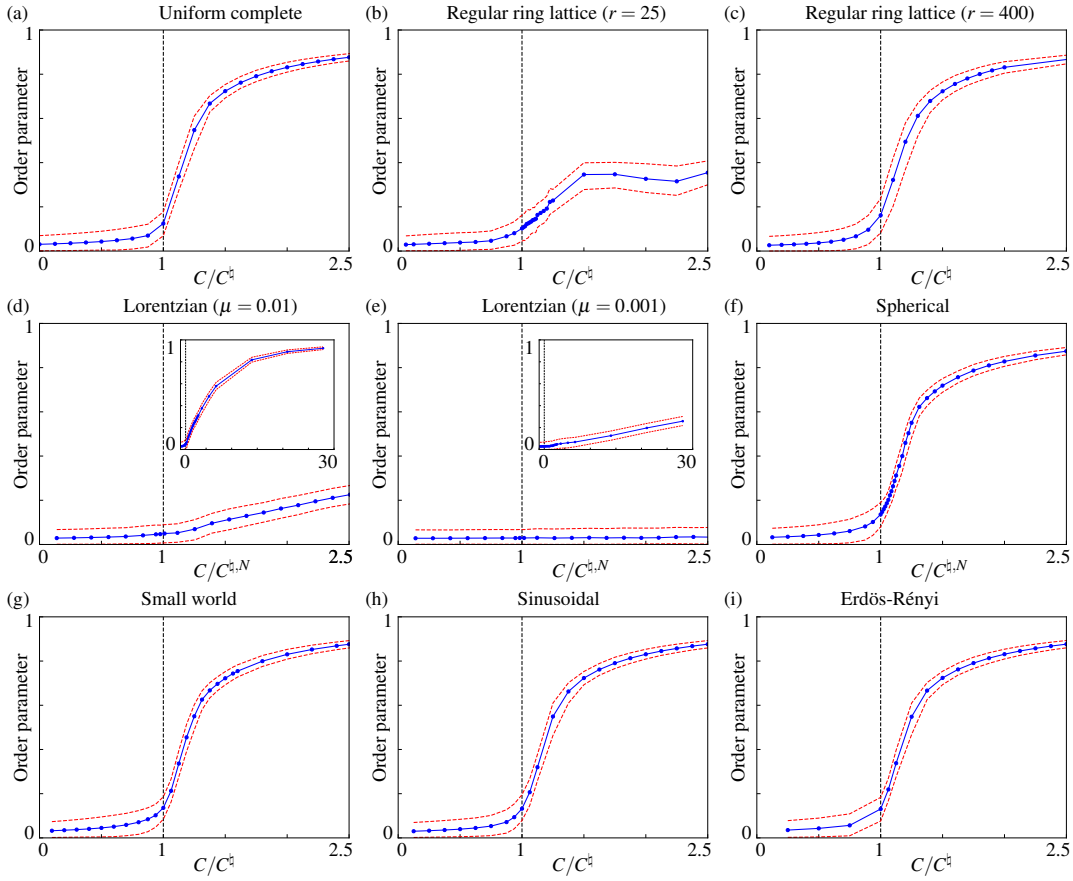

FIG. 2. Incoherence-coherence transition for numerical solutions of (2) for different coupling topologies. The dashed black lines show the respective value of $C^{\natural}$. The red dashed lines show $\langle r_{\min}\rangle$ and $\langle r_{\max}\rangle$, while the blue lines show $\langle \bar{r}\rangle$. a) Uniform complete graph, $C^{\natural} = 0.08$. b) Regular ring lattice with $r = 25, C^{\natural} = 0.8$. c) Regular ring lattice with $r = 400, C^{\natural} = 0.05$. d) Lorentzian graph with $\mu = 0.01, C^{\natural,N} = 0.0718$. e) Lorentzian graph with $\mu = 0.001, C^{\natural,N} = 0.0713$. f) Spherical graph with $M = 50, C^{\natural,N} = 0.8003$. g) Small-World graph with $k = 100, p = 0.5, C^{\natural} = 0.2$. h) Sinusoidal graph, $C^{\natural} = 0.08$. i) Erdös-Rényi graph with $p = 0.5, C^{\natural} = 0.08$. Parameters for all graphs: $N = 1000, \Delta t = 0.01, T_{\text{tr}} = 700, T = 1000, \beta = 50$, ten realizations of Brownian motion, eight realizations of the graph (if random). $C^{\natural,N}$ is evaluated when $C^{\natural}$ cannot be evaluated.

set of the incoherence-coherence transition. Results for the incoherence-coherence transitions for the various graph topologies are summarized in Fig. 2.

1. Incoherence-Coherence threshold for finite and infinite oscillator systems

We extend our analysis to different coupling topologies while using the coupling interaction $D(u) = \sin(u)$. The theoretically predicted threshold for the incoherence-coherence transition, $C^{\natural}$, valid in the mean-field limit is calculated using (22). We shall compare the numerical findings to this theoretical prediction for coupling topologies where it is possible, However, for certain graphops A, a characterization of $\sigma(A)$ exceeds the scope of this study (Spherical graph in Sec. IV B 2 d; Lorentzian graph in Sec. IV B 2 f). In such cases, we instead compute the eigenvalues $\sigma^N(A^N)$ of a discrete coupling matrix A^N that approximates A. We expect that the finite-dimensional matrices A^N can be used to provide an approximation to (at least the boundary of) the spectrum of the limiting graphop A as $N \to \infty$, and so $C^{\natural}$ can be approximated by its discrete corollary

$$C^{\natural,N} = \frac{2}{\beta \Lambda^N(A^N)} \tag{29}$$

where $\Lambda^N(A^N) := \max_{\lambda \in \sigma^N(N^{-1}A^N)} |\lambda|$ is the maximal eigenvalue associated with A^N. Finally, we also mention the pos-

sibility of "spectral pollution"[52] which in principle can occur when numerically approximating the spectrum of an operator with finite dimensional matrices. However, as we shall see, our numerical and analytical results are consistent so we therefore anticipate that the numerical calculations are sufficiently stable.

2. *Coupling topologies*

a. Regular ring lattice with r neighbors. Nodes for this coupling topology may be imagined to be arranged on a ring, such that every node is linked to a given number of r nearest neighbors. In the continuum limit $N \to \infty$, the ring lattice graphon can be defined as

$$K(x,y) = \begin{cases} 1 & \min\{|x-y|, 1-|x-y|\} \le h \\ 0 & \text{otherwise,} \end{cases} \tag{30}$$

where $0 \le h \le 1/2$ is the (continuous) coupling range for oscillators located at x and y on Ω. The graphop A defined via this graphon kernel K has $\Lambda(A) = 2h$ (this can be shown e.g. by writing $K(x,y)$ as a Fourier series and the values of $\sigma(A)$ are given in Ref. 53.)

For $N < \infty$ we simply define the regular ring lattice graph via

$$A_{kj} = \begin{cases} 1 & k \ne j \text{ and } \min\{|k-j|, 1-|k-j|\} \le r \\ 0 & \text{else} \end{cases} \tag{31}$$

where the (discrete) coupling range $r = r(h) \in [N]$ for oscillators located at k and j in $[N]$ satisfies $0 \le r \le N/2$ with N even. It is easy to check that $\Lambda^N(A^N) = 2r/N$. In our simulations we choose r from which the value h for the corresponding graphon kernel follows via $h = r/N$. We then have $\Lambda(A) = \Lambda^N(A^N) = 2r/N$. We note two limiting cases, namely, we obtain all-to-all coupling for $h = 1/2$, and zero coupling for $h = 0$.

b. Erdös-Rényi graph. The Erdös-Rényi (ER) graph(on) is constructed in a random process where the presence (or absence) of every edge (of the complete graph) is chosen with a probability $p \in [0,1]$.

In the continuum limit, $N \to \infty$, the Erdös-Rényi graphop simply becomes the complete (all-to-all) graphop with constant uniform coupling strength p, i.e., the corresponding graphon kernel is $K(x,y) = p$, see Ref. 54. It follows then that $C^\natural = 2/(\beta p)$.

For finite oscillators $N < \infty$, a realization of the ER graph on N nodes may be obtained by drawing $N(N-1)/2$ random numbers a_{kj}, $1 \le k < j \le N$, from the uniform distribution on the interval $[0,1]$. The adjacency matrix of the graph is then

$$A^N_{kj} = A^N_{jk} = \begin{cases} 1 & k < j,\ a_{kj} \le p \\ 0 & \text{else} \end{cases} \tag{32}$$

For $p = 1$ we obtain all-to-all coupling with uniform coupling strength 1 (complete graph), while $p = 0$ yields zero coupling.

c. Small-World graph. The small world (SW) graph[55] interpolates between a regular ring lattice and a ER graph structure, thus creating a topology that quite regular but also entertains random links across the network. This structure results in short path lengths even when nodes are far away on the ring.

For finite graphs, $N \to \infty$, the small world graphop A can be constructed via the graphon kernel[56,57] given by

$$K(x,y) = (1-p)W(x,y) + 2ph \tag{33}$$

where

$$W(x,y) = \begin{cases} 1 & \min\{|x-y|, 1-|x-y|\} \le h \\ 0 & \text{else} \end{cases} \tag{34}$$

with (continuous) coupling range $0 \le h \le 1/2$ (note that $W(x,y)$ is identical to $K(x,y)$ in (30) further above for the regular ring lattice). It can be shown that $\Lambda(A) = 2h$ (to see this, one needs to write $K(x,y)$ in terms of a Fourier series; the values of $\sigma(A)$ are given by Gao and Caines[53].).

For $N < \infty$, realizations of the SW graph on N nodes may be obtained via the procedure introduced by Watts and Strogatz[55]: One starts with a regular ring lattice on N nodes with r nearest neighbors (discrete coupling range). One selects a constant probability $p \in [0,1]$. For each node k and each link between k and its r nearest neighbors to the right, we draw a random number $X \in [0,1]$ i.i.d. from the uniform distribution. If $X \le p$, we draw a random integer j from the uniform distribution on $[N]$. If $k \ne j$ and the edge (k,j) does not yet exist, it is created and the old link deleted.

In our numerical setting we simply pick a value r and the value h for the corresponding graphon kernel follows from $h = r/N$. We numerically confirmed that $\Lambda^N(A^N) \approx \Lambda(A) = 2h$. We shall thus use the value $C^{\natural,N} \approx C^\natural = 1/(\beta h)$.

d. Spherical graph. The action of the spherical graphop $A : L^2(\mathbb{S}_2) \mapsto L^2(\mathbb{S}_2)$ on a function f is defined by

$$(Af)(x) = \int_{y \perp x} f(y) \mathrm{d}\nu_x \tag{35}$$

where ν_x is the uniform measure. The spherical graphop thus integrates f over the circle on the unit sphere that consists of all the points perpendicular to x. This circle is the *equator* of the point x. The spherical graphop does not have a graphon kernel nor a known spectrum, so we need to calculate $C^\natural$ via (29). Moreover, a matrix approximation to the spherical graphop has to our knowledge not yet been proposed. Here we propose a possible approximation without claiming any convergence properties as $N \to \infty$. Choosing N (approximately equidistant) sample points $x_1, \ldots, x_N$ on the unit sphere, we may obtain a matrix A^N approximating A by defining $A^N_{kj} = A^N_{jk} = 1$ if x_k and x_j are approximately perpendicular, otherwise $A^N_{kj} = A^N_{jk} = 0$. The discretized version of (35) then reads

$$(A^N f)_k = \frac{1}{N} \sum_{j=1}^{N} A^N_{kj} f(x_j) \tag{36}$$

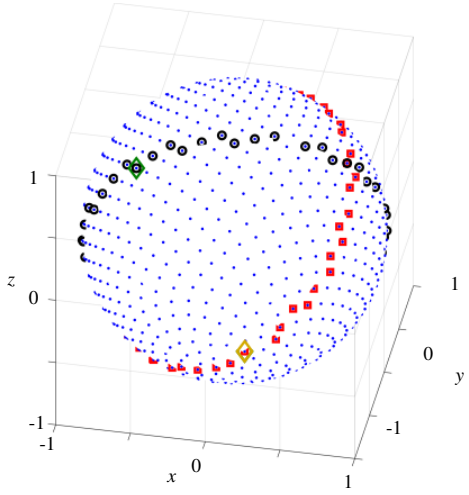

FIG. 3. Matrix approximation for the spherical graphop. Blue dots indicate the sample points, black circles mark points belonging to the discretized equator of one of the exemplary points (yellow diamond), red squares mark points belonging to the discretized equator of the other exemplary point (green diamond). The two exemplary points are thus members of each other's discretized equators. Parameters are $N = 1000$ and $M = 50$.

We refer to A^N as *spherical graph*. Three requirements should be made on A^N. For each point x_k, the points x_j for which $A^N_{kj} = 1$ should (i) lie sufficiently close to the equator of x_k, (ii) be sufficiently equidistant and (iii) be (almost) equally many for all k. Clearly, if we take an arbitrary point on the unit sphere, one can place M perfectly equidistant points on its equator. However, (i) and (ii) must be fulfilled reasonably well for *all* N points and their respective equators. So the points should form a regular grid. While a perfectly regular grid of $N > 6$ points on the sphere is impossible, there exist approximately regular grids[58]. Here, we place the points in a spiral of width $0.1 + 1.2N$ around the sphere, starting and ending (approximately) on the poles. This method is implemented in the Mathematica Software package[59]. We denote the set of points with this spacing on the unit sphere as P. The task is to determine subsets $E_k \subset P, 1 \leq k \leq N$, such that each E_k discretizes the equator of x_k. To this end, we first calculate $p_{kj} := |\langle x_k, x_j \rangle|$ for each $1 \leq k < j \leq N$, to determine how close the pairs of points are to being perpendicular. Then we specify M, the desired (approximate) cardinality of all E_k's. Now we can, for each k, find the (approximately) M points x_j with the smallest values of p_{kj} and make them members of E_k, under the constraint that if $x_k \in E_j$, then $x_j \in E_k$, to ensure that A^N is symmetric. We end up with a (symmetric) A^N that fulfills demands (i) and (ii) in an acceptable manner while demand (iii) is fulfilled well: $|E_k|$ is either M or $M-1$ for all $1 \leq k \leq N$ (see Fig. 3). We find $\Lambda^N(A^N) = 0.04998$ and thus $C^{\natural,N} = 0.8003$.

e. Sinusoidal graph. In the sinusoidal coupling topology, nodes are coupled most strongly to their nearest neighbors, the coupling then smoothly decreases the farther neighbors are apart, finally the coupling is zero between nodes opposite on the ring. We define the graphon kernel as

$$K(x,y) = \frac{1}{2}(1 + \cos 2\pi(x-y)). \tag{37}$$

It can be shown[53] that the graphop A induced by K has $\Lambda(A) = 1/2$ so that $C^{\natural} = 4/\beta = 0.08$.

For $N < \infty$, we define the matrix A^N by

$$A^N_{k,j} = \frac{1}{2}\left(1 + \cos\left(2\pi\frac{k-j}{N}\right)\right) \tag{38}$$

f. 'Lorentzian' graph. We also consider graphs for which a mean-field description is more challenging, and which therefore could potentially fail to exhibit the behavior predicted by Theorem III.1. A good candidate would be an irregular and sparse graph with few very strong links, while the vast majority of links is very weak. We can define such a topology based on the Lorentzian (graphon) kernel

$$\begin{aligned} K(x,y) = &\frac{\mu/\pi}{(x-x_0)^2 + (y-y_0)^2 + \mu^2} \\ &+ \frac{\mu/\pi}{(x-y_0)^2 + (y-x_0)^2 + \mu^2} \end{aligned} \tag{39}$$

where $x_0, y_0 \in [0,1]$. $K(x,y)$ peaks in the points (x_0,y_0) and (y_0,x_0), which converge to Dirac delta distributions as $\mu \to 0$. We approximate this graphon in the finite representation as

$$\begin{aligned} A^N_{kj} = &\frac{\mu/\pi}{\left(\frac{k}{N} - x_0\right)^2 + \left(\frac{j}{N} - y_0\right)^2 + \mu^2} \\ &+ \frac{\mu/\pi}{\left(\frac{k}{N} - y_0\right)^2 + \left(\frac{j}{N} - x_0\right)^2 + \mu^2} \end{aligned} \tag{40}$$

We use the values $x_0 = 0.25, y_0 = 0.75$ with $\mu = 0.01$ or $\mu = 0.001$. Computing the spectrum $\sigma(A)$ of the graphop A defined by K exceeds the scope of this work, and we use the eigenvalues of A^N,

$$\Lambda^N(A^N)\Big|_{\mu=0.01} = 0.5573, \quad \Lambda^N(A^N)\Big|_{\mu=0.001} = 0.5612,$$

to obtain

$$C^{\natural,N}\Big|_{\mu=0.01} = 0.0718, \quad C^{\natural,N}\Big|_{\mu=0.001} = 0.0713.$$

V. CONCLUSION AND OUTLOOK

We formulated a mean-field theory for stochastic phase oscillator models with nontrivial coupling, i.e., heterogenous graph topologies and coupling weights. Our analysis for Kuramoto-type models with odd symmetric coupling functions, obtained via linearization around the incoherent solution branch, yields an exact formula for the critical coupling strength $C^{\natural}$ at the incoherence-coherence transition in

the mean-field limit. Numerically integrating finite representations (see Eq. (1)) agree very well with the predicted threshold $C^\natural$ (Eq. (22)) for a wide range of heterogeneous graph structures (see Fig. 2)[60]. We therefore expect our theory to be applicable to a large range of applications with heterogeneous oscillator interactions, such as systems with non-uniform coupling associated with chimera states[61] or XY-oscillators type models with random coupling[34,62].

For certain graph topologies characterized by strong sparsity, large variance in coupling strengths, or other types of "clusterization" implying coupling fragmentation in the network, the mean-field description is expected to break down, in particular also in terms of correctly predicting the incoherence-coherence transition for finite-size systems. We found that such a problem occurs at least for one instance, namely for the Lorentzian graph topology (see Fig. 2 panels (d) and (e)), for which the detection of a sharp transition point numerically is difficult. The Lorentzian graph is characterized by only a few nodes with very strong edge weights, while the vast majority of edge weights are very weak: the graph topology is effectively very sparse. This implies that we need a much larger C to observe coherent oscillations. As becomes apparent from comparing panels (d) and (e), the different quality of the incoherence-coherence transition between the Lorentzian and the other graphs considered is especially pronounced as the effective sparsity increases ($\mu \to 0$). Note that not merely larger overall coupling strength C is needed to achieve (partial) coherence, when compared to other topologies; if that were the case, one would just observe larger $C^\natural$ for the Lorentzian graph as compared to the other graphs, and the coherence onset woudl still set in at $C = C^\natural$. Rather, the onset of coherence appears to be delayed beyond $C = C^\natural$, so that the increase of partial synchrony sets in very slowly as C increases. This observation becomes especially pronounced for very small μ so that the coupling kernel becomes effectively very sparse. Thus, the Lorentzian graph represents an interesting coupling topology that demarcates a possible class of graphs for which — at least for certain values of μ — our mean-field description and prediction for the incoherence-coherence transition for the finite-size representation break down.

While we extended the mean-field theory for the stochastic Kuramoto model with all-to-all connectivity and uniform coupling weights to heterogeneous connectivity with non-uniform coupling strengths, certain constraints apply to our model. These may limit the validity of our theory and prompt avenues for future research. For instance, we have assumed that the coupling function $D(u)$ is odd. This assumption excludes in particular the Kuramoto-Sakaguchi model which has a coupling function $D(u) = \sin(u+\alpha)$ with a phase-lag α. This phase-lag allows to tune the coupling interaction to be a sine function versus cosine, distinguishing gradient-like and integrable dynamics, respectively (compare with Eqs. (2) without noise, $\beta^{-1} = 0$) and implies different incoherence-coherence transitions (Note that a mix of such interaction also is essential to observe symmetry breaking chimera states with nonuniform synchronization patterns on the network[61,63]) — extending our theory to such interactions would be of interest. Coupling functions $D(u)$ of higher harmonic order have recently attracted much interest, which imply more complicated stability regimes and transitions between incoherence and coherence[64–67]. Moreover, interactions with arbitrary (e.g. non-symmetric) coupling interactions $D = D(u_k, u_l)$ are possible[68] which imply directed graph topologies[47]. While we studied the Kuramoto model with identical intrinsic frequencies, the presence of distributed frequencies is also of interest. Finally, extensions to other phase oscillator models, such as the Kuramoto model with inertia[26,69] or the theta neuron (or QIF neuron) that only perform rigid rotations corresponding to spiking above a threshold current, are worth mentioning. It would be very useful to derive rigorous mean-field descriptions for the above mentioned systems; today, mean-field descriptions are available only for full graph structures[70,71]. Finally, one might also consider transitions between — or bifurcations of — states other than incoherence or coherence, such as chimera states, or twisted states. Twisted states arise in bifurcations due to negative eigenvalues from the graph operator[72]. It would be interesting to extend the mean-field theory developed here to such cases. Some work in these directions has been done in the context hypergraphs[73].

Another important avenue for future research is to clarify the validity regime for mean-field descriptions for very sparse and very heterogeneous structures. Note carefully that the effective dimension of the VFPE mean-field equation (15a) will grow the more heterogeneous the graph is due to the dependence of the node type encoded by points in Ω. Hence, a mean-field description can still exist and our results indicate this mean-field is often still very useful to determine whether some number of nodes starts to transition from incoherence to partial synchronization. Yet, for more complex patterns, involving an interplay between all different mean-field node types on very sparse structures, we anticipate that the mean-field description will eventually not be of much use as it is also high-dimensional. In summary, to fully determine the theoretical and practical limitations of heterogeneous mean-field VFPEs remains a challenging problem for future work.

VI. ACKNOWLEDGMENTS

MAG and CK gratefully thank the TUM International Graduate School of Science and Engineering (IGSSE) for support via the project "Synchronization in Co-Evolutionary Network Dynamics (SEND)". BJ and EAM acknowledge the DTU International Graduate School for support via the EU-COFUND project "Synchronization in Co-Evolutionary Network Dynamics (SEND)". CK also acknowledges partial support by a Lichtenberg Professorship funded by the Volkswagen Stiftung.

VII. DATA AVAILABILITY STATEMENT

Data sharing is not applicable to this article as no new data were created or analyzed in this study.

REFERENCES

[1] Arkady Pikovsky, Michael Rosenblum, and Jürgen Kurths. *Synchronization. A universal concept in nonlinear sciences*. Cambridge University Press, New York, NY, USA, 2001.

[2] Steven H. Strogatz. *Sync: The Emerging Science of Spontaneous Order*. 2003.

[3] Gyorgy Buzsaki. *Rhythms of the Brain*. Oxford University Press, 2006.

[4] H. Arakai, editor. *International Symposium on Mathematical Problems in Theoretical Physics, Lecture Notes in Physics*, volume 39. Springer, New York, 1975.

[5] Yoshiki Kuramoto. *Chemical oscillations, waves, and turbulence*. Springer-Verlag, New York, 1984.

[6] Steven H Strogatz. From Kuramoto to Crawford: exploring the onset of synchronization in populations of coupled oscillators, 2000.

[7] Juan Acebrón, L. Bonilla, Conrad Pérez Vicente, Félix Ritort, and Renato Spigler. The Kuramoto model: A simple paradigm for synchronization phenomena. *Reviews of Modern Physics*, 77(1):137–185, apr 2005.

[8] James P. Gleeson, Sergey Melnik, Jonathan A. Ward, Mason A. Porter, and Peter J. Mucha. Accuracy of mean-field theory for dynamics on real-world networks. *Physical Review E*, 85(2):026106, Feb 2012.

[9] Christiaan Huygens. *Oeuvres complètes de Christiaan Huygens: L'horloge à pendule de 1651 à 1666. Travaux divers de physique, de mécanique et de technique de 1650 à 1666. Traité des couronnes et des parhélies (1662 ou 1663)*, volume 17. M. Nijhoff, Swets \& Zeitlinger Publishers, Amsterdam, 1967.

[10] Steven H. Strogatz. Norbert Wiener's brain waves. In *Frontiers in Mathematical Biology: Lecture Notes in Biomathematics, Vol. 100*, volume 100, pages 122–122. Springer, 1994.

[11] Arthur T Winfree. Biological rhythms and the behavior of populations of coupled oscillators. *Journal of Theoretical Biology*, 16(1):15–42, 1967.

[12] Hidetsugu Sakaguchi and Yoshiki Kuramoto. A soluble Active Rotator Modle Showing Phase Transitions via Mutual Entrainment. *Progress of Theoretical Physics*, 76(3):576–581, 1986.

[13] Shamik Gupta, Alessandro Campa, and Stefano Ruffo. *Statistical Physics of Synchronization*. Springer, 2018.

[14] Steven H Strogatz and Renato E Mirollo. Stability of Incoherence in a Population of Coupled Oscillators. *Journal of Statistical Physics*, 63:613–635, 1991.

[15] J.A. Acebron, LL Bonilla, S. De Leo, and R. Spigler. Breaking the symmetry in bimodal frequency distributions of globally coupled oscillators. *Physical Review E*, 57(5):5287–5290, 1998.

[16] R. Mirollo and S. H. Strogatz. The spectrum of the partially locked state for the Kuramoto model. *Journal of Nonlinear Science*, 17(4):309–347, 2007.

[17] Shinya Watanabe and Steven H. Strogatz. Integrability of a globally coupled oscillator array. *Physical Review Letters*, 70(16):2391–2394, 1993.

[18] Edward Ott and Thomas M Antonsen. Low dimensional behavior of large systems of globally coupled oscillators. *Chaos (Woodbury, N.Y.)*, 18(3):037113, sep 2008.

[19] Christian Bick, Marc Goodfellow, Carlo R. Laing, and Erik Andreas Martens. Understanding the dynamics of biological and neural oscillator networks through exact mean-field reductions: a review. *Journal of Mathematical Neuroscience*, 10(9):1–43, 2020.

[20] Jordi García-Ojalvo and José Sancho. *Noise in spatially extended systems*. Springer Science & Business Media, 2012.

[21] Hawoong Jeong, Bálint Tombor, Réka Albert, Zoltan N Oltvai, and A-L Barabási. The large-scale organization of metabolic networks. *Nature*, 407(6804):651–654, 2000.

[22] D Brockmann, L Hufnagel, and T Geisel. The scaling laws of human travel. *Nature*, 439(7075):462–465, jan 2006.

[23] Claudio Castellano, Santo Fortunato, and Vittorio Loreto. Statistical physics of social dynamics. *Reviews of Modern Physics*, 81(2):591–646, may 2009.

[24] Edward T Bullmore and Olaf Sporns. Complex brain networks: graph theoretical analysis of structural and functional systems. *Nature reviews. Neuroscience*, 10(3):186–98, 2009.

[25] B Suki, AL Barabasi, Z Hantos, F Peták, and HE Stanley. Avalanches and power-law behaviour in lung inflation. *Nature*, 368:615–618, 1994.

[26] Martin Rohden, Andreas Sorge, Marc Timme, and Dirk Witthaut. Self-organized synchronization in decentralized power grids. *Physical review letters*, 109(6):64101, 2012.

[27] Pablo Kaluza, Andrea Kölzsch, Michael T Gastner, and Bernd Blasius. The complex network of global cargo ship movements. *Journ. Roy. Society, Interface*, 7(48):1093–103, jul 2010.

[28] Seung Woo Son and Hyunsuk Hong. Thermal fluctuation effects on finite-size scaling of synchronization. *Physical Review E - Statistical, Nonlinear, and Soft Matter Physics*, 81(6):1–7, 2010.

[29] S H Strogatz. Exploring complex networks. *Nature*, 410(6825):268–76, mar 2001.

[30] Juan G Restrepo, Edward Ott, and Brian R Hunt. Emergence of Coherence in Complex Networks of Heterogeneous Dynamical Systems. *Physical Review Letters*, 96(25):1–4, jun 2006.

[31] Y Kuramoto and D Battogtokh. Coexistence of Coherence and Incoherence in Nonlocally Coupled Phase Oscillators. *Nonlinear Phenomena in Complex Systems*, 4:380 – 385, 2002.

[32] Mark J Panaggio and Daniel M Abrams. Chimera states: Coexistence of coherence and incoherence in networks of coupled oscillators. *Nonlinearity*, 28(3):R67–R87, 2015.

[33] Daniel A. Wiley, Steven H. Strogatz, and Michelle Girvan. The size of the sync basin. *Chaos*, 16(1), 2006.

[34] David Sherrington and Scott Kirkpatrick. Solvable model of a spin-glass. *Physical Review Letters*, 35(26):1792, 1975.

[35] Tae-Wook Ko and G. Ermentrout. Partially locked states in coupled oscillators due to inhomogeneous coupling. *Physical Review E*, 78(1):1–6, jul 2008.

[36] Istvan Z Kiss, Yumei Zhai, and John L Hudson. Emerging coherence in a population of chemical oscillators. *Science*

(New York, N.Y.), 296(5573):1676–8, may 2002.

[37]Annette F Taylor, Mark R Tinsley, Fang Wang, Zhaoyang Huang, and Kenneth Showalter. Dynamical quorum sensing and synchronization in large populations of chemical oscillators. *Science (New York, N.Y.)*, 323(5914):614–617, jan 2009.

[38]Dumitru Călugăru, Jan Frederik Totz, Erik A Martens, and Harald Engel. First-order synchronization transition in a large population of relaxation oscillators. *Science Advances*, 6(39):eabb2637, 2020.

[39]Erik Andreas Martens, Shashi Thutupalli, Antoine Fourrière, and Oskar Hallatschek. Chimera States in Mechanical Oscillator Networks. *Proc. Natl. Acad. Sci.*, 110(26):10563–10567, 2013.

[40]László Lovász and Balázs Szegedy. Limits of dense graph sequences. *Journal of Combinatorial Theory, Series B*, 96(6):933–957, 2006.

[41]László Lovász. *Large networks and graph limits*, volume 60. American Mathematical Soc., 2012.

[42]A. Backhausz and B. Szegedy. Action convergence of operators and graphs. *Canad. J. Math.*, 74(1):72–121, 2022.

[43]H. Chiba and G. Medvedev. The mean field analysis for the Kuramoto model on graphs I. the mean field equation and transition point formulas. *Discr. Cont. Dyn. Syst. A*, 39(1):131–155, 2019.

[44]D. Kaliuzhnyi-Verbovetskyi and G.S. Medvedev. The mean field equation for the Kuramoto model on graph sequences with non-Lipschitz limit. *SIAM J. Math. Analysis*, 50(3):2441–2465, 2018.

[45]C. Kuehn. Network dynamics on graphops. *New Journal of Physics*, 22(5):053030, 2020.

[46]M.A. Gkogkas and C. Kuehn. Graphop mean-field limits for Kuramoto-type models. *SIAM J. Appl. Dyn. Syst.*, 21(1):248–283, 2022.

[47]C. Kuehn and C. Xu. Vlasov equations on digraph measures. *arXiv:2107.08419*, pages 1–69, 2021.

[48]M.A. Gkogkas, C. Kuehn, and C. Xu. Mean field limits of co-evolutionary heterogeneous networks. *arXiv:2202.01742*, pages 1–51, 2022.

[49]Francisco A. Rodrigues, Thomas K. DM. Peron, Peng Ji, and Jürgen Kurths. The Kuramoto model in complex networks. *Physics Reports*, 610:1–98, 2016.

[50]H. Sakaguchi. Cooperative phenomena in coupled oscillator systems under external fields. *Prog. Theor. Phys.*, 79(1):39–46, 1988.

[51]Finite size fluctuations are pseudo-random: finitely many oscillators move around the unit circle with distinct velocity differences and thus perpetually change their relative locations on the unit circle).

[52]Edward B Davies and Michael Plum. Spectral pollution. *IMA journal of numerical analysis*, 24(3):417–438, 2004.

[53]Shuang Gao and Peter E Caines. Spectral representations of graphons in very large network systems control. In *2019 IEEE 58th conference on decision and Control (CDC)*, pages 5068–5075. IEEE, 2019.

[54]The nonlinear heat equation on dense graphs and graph limits. *SIAM Journal on Mathematical Analysis*, 46(4).

[55]D J Watts, D J Watts, S H Strogatz, and S H Strogatz. Collective dynamics of "small-world" networks. *Nature*, 393(6684):440–2, 1998.

[56]Georgi S. Medvedev. Small-world networks of kuramoto oscillators. *Physica D: Nonlinear Phenomena*, 266:13–22, 2014. arXiv: 1307.0798v2.

[57]Georgi S Medvedev. The nonlinear heat equation on w-random graphs. *Archive for Rational Mechanics and Analysis*, 212(3):781–803, 2014.

[58]Jonathan Kogan. A new computationally efficient method for spacing n points on a sphere. *Rose-Hulman Undergraduate Mathematics Journal*, 18(2):5, 2017.

[59]Spherepoints, 2017.

[60]Note that the regular ring lattice with $N = 1000$ displays imperfect synchronization ($0 \ll r \ll 1$) for $r = 25$ (Fig. 2 panel (b)), while $r = 400$ a more regular emergence of (partial) coherence (Fig. 2panel (c)); indeed, this case (with zero noise) is known to exhibit multistability between the coherent branch and a so-called twisted state as long as $r/N < 0.34$[33].

[61]M. J. Panaggio and D. M. Abrams. Chimera states: Coexistence of coherence and incoherence in networks of coupled oscillators. *Nonlinearity*, 28(3):R67–R87, 2015.

[62]Hyunsuk Hong and Erik Andreas Martens. First-order like phase transition induced by quenched coupling disorder. *arXiv*, 1(1):1–7, 2021.

[63]Oleksandr Burylko, Erik Andreas Martens, and Christian Bick. Symmetry breaking yields chimeras in two small populations of kuramoto-type oscillators. *arXiv:2202.10807 [nlin]*, Feb 2022. arXiv: 2202.10807.

[64]Peter Ashwin and Oleksandr Burylko. Weak chimeras in minimal networks of coupled phase oscillators. *Chaos*, 25(1), 2015. arXiv: 1407.8070.

[65]Peter Ashwin, Christian Bick, and Oleksandr Burylko. Identical phase oscillator networks: Bifurcations, symmetry and reversibility for generalized coupling. *Frontiers in Applied Mathematics and Statistics*, 2:7, 2016.

[66]Yoshiki Kuramoto. *Nonlinear dynamics and chaos: where do we go from here?* Taylor & Francis, 2003. Citation Key: Kuramoto2003.

[67]C. Bick, T. Böhle, and C. Kuehn. Multi-population phase oscillator networks with higher-order interactions. *arXiv:2012.04943*, pages 1–30, 2020.

[68]Bastian Pietras and Andreas Daffertshofer. Network dynamics of coupled oscillators and phase reduction techniques. *Physics Reports*, 2019. Citation Key: Pietras2019.

[69]G. Bard Ermentrout. An adaptive model for synchrony in the firefly Pteroptyx malaccae. *Journal of Mathematical Biology*, 29(6):571–585, 1991.

[70]Ernest Montbrió, Diego Pazó, and Alex Roxin. Macroscopic description for networks of spiking neurons. *Physical Review X*, 5(2):1–15, 2015. arXiv: 1506.06581v1 Citation Key: Montbrio2015.

[71]Christian Kuehn and Sebastian Throm. Power network dynamics on graphons. *SIAM Journal on Applied Mathematics*, 79(4):1271–1292, 2019.

[72]Hayato Chiba, Georgi S Medvedev, and Matthew S Mizuhara. Bifurcations in the kuramoto model on graphs.

Chaos: An Interdisciplinary Journal of Nonlinear Science, 28(7):073109, 2018.

[73] Christian Kuehn and Chuang Xu. Vlasov equations on directed hypergraph measures. *arXiv preprint arXiv:2207.03806*, 2022.

Article [3] – Complex dynamics in adaptive phase oscillator networks

---

Article [3], entitled *Complex dynamics in adaptive phase oscillator networks*, was written in collaboration with Erik A. Martens as a research output of the PhD. As of the 14^{th} of September 2022, article [3] has not yet been submitted to a journal. The manuscript in progress is attached here.

The authors of this article are: Benjamin Jüttner and Erik A. Martens.

Complex dynamics in adaptive phase oscillator networks

Benjamin Jüttner[a] and Erik A. Martens[b,c a)]
[a] Department of Applied Mathematics and Computer Science, Technical University of Denmark, 2800 Kgs. Lyngby, Denmark
[b] Centre for Mathematical Sciences, Lund University, Sölvegatan 18B, 221 00 Lund, Sweden
[c] Center for Translational Neurosciences, University of Copenhagen, Blegdamsvej 3, 2200 Copenhagen, Denmark

(Dated: September 13, 2022)

Networks of coupled dynamical units give rise to collective dynamics such as the synchronization of oscillators or neurons in the brain. The ability of the network to adjust coupling weights between units in accordance with their activity arises naturally in a variety of contexts, including neural plasticity in the brain, and adds an additional layer of complexity: the dynamics on the nodes influence the dynamics of the network and vice versa. We study a model of Kuramoto phase oscillators with a general adaptive learning rule with three parameters, including paradigms of (anti-)Hebbian learning and spike time dependent plasticity (STDP) as special cases. An important feature is the adaptivity parameter that allows to study the impact of adaptation on the collective dynamics as we move away from the non-adaptive manifold given by stationary coupling. First, we carry out a detailed bifurcation analysis for $N = 2$ oscillators with (un)directed coupling and provide stability diagrams. Adaptation dynamics in terms of nontrivial bifurcations arises only when the adaptivity parameter exceeds a critical threshold. While (anti-)Hebbian learning and STDP result in non-trivial multi-stability and bifurcation scenarios, mixed-type learning rules exhibit even more complicated and rich dynamics including a transition to chaotic dynamics. Second, we numerically investigate a larger system with $N = 50$ oscillators and explore dynamic similarities with the case of $N = 2$ oscillators.

PACS numbers: 05.45.-a, 05.45.Gg, 05.45.Xt, 02.30.Yy
Keywords: adaptive oscillator networks, Kuramoto model, synchronization, bifurcation analysis

Synchronization is a ubiquitous phenomenon manifesting itself in a range of natural and technological systems[1,2]. The presence or absence of synchronization orchestrates the proper functioning of complex networks, such as in neural networks in the brain[3,4] or power transmission networks[5]. A paradigmatic model to study synchronization is Kuramoto's model that describes the dynamics of phase oscillators. Many variants have been studied in literature[6,7]; here, we are concerned with the dynamics that emerges when coupling weights adapt according to the oscillator activity[8,9]. Such ability to adapt the coupling weight has been receiving much attention lately[10–13] and finds applications for models of synaptic plasticity and learning in the brain[14]. We consider the adaptive Kuramoto model with two oscillators in the limit of stationary coupling and investigate how the strength of adaptivity affects the dynamics of the network and find that generally, the synchronizability increases with a larger level of adaptivity. Nontrivial bifurcations, unknown to the Kuramoto model with stationary coupling, emerge at a critical adaptivity threshold. We analytically and numerically determine these bifurcations and their stability boundaries for several types of learning paradigms. Finally, numerical simulations give a glimpse into how the dynamics observed for small systems with two oscillators carries over to larger systems with a larger number of oscillators.

a) Electronic mail: erik.martens@math.lth.se

I. INTRODUCTION

The synchronization of coupled oscillators is a fascinating manifestation of self-organization — indeed, self-emergent synchronization is a central process to a spectacular range of natural and technological systems, including the beating of the heart[15], flashing fireflies[16], pedestrians on a bridge locking their gait[17], genetic clocks[18], pendulum clocks hanging on a beam[19],superconducting Josephson junctions[20], chemical oscillations[21,22], metabolic oscillations in yeast cells[23], and life cycles of phytoplankton[24], and networks of neurons in the brain[3,4].

A desirable property in real-world oscillator networks is the presence of synchronization whenever it ensures the proper functioning of the network: in the realm of technology, for instance, the AC current between generators and consumers in a power grid need to stay synchronized to ensure ideal power transmission and ultimately avoid power blackouts[5]; and wireless networks require synchronized clocks[25] to ensure safe data transmission; in the realm of biology, the proper functioning of the heart requires that the rhythmic electric activation of cardiac cells stays coordinated[15].

While the network interaction between dynamic units may give rise to intriguing collective behaviors such as synchronization, adding the ability to adapt the (coupling) weights on a network according to the dynamics on its nodes leads to co-evolutionary network dynamics [26]. Indeed — "Intelligence is the ability to adapt to change" (Stephen Hawking) — the adaptive dynamics of co-evolutionary networks may allow to increase their functional robustness. Adaptive co-evolutionary networks appear in a wide range of systems, including the vascular network[27–29], the glymphatic net-

work of the brain[30–32], osteocyte network formation[33], social networks[34], and, in particular, in neural networks in the brain where neural plasticity plays an important role for learning[14,35], but also for the progression of certain neurodegenerative diseases[36]. In the current context, this raises the question if adaptivity in a coupled oscillator network can increase its ability to synchronize.

We devise a special variation of the Kuramoto model with adaptive coupling weights. While previous studies have considered such systems from various perspectives, we here introduce a parameterization that allows to systematically deviate from the traditional Kuramoto system with stationary coupling and study the resulting bifurcation behavior in a systematic way.

This article is structured as follows. In Sec. II, we explain our adaptive Kuramoto model and how we parameterize it. In Sec. III, we consider $N = 2$ oscillators and carry out a detailed bifurcation analysis for several important parameter cases: III A non-adaptive Kuramoto model; III B (anti-)Hebbian learning limit $\alpha = \beta = 0$, i.e., adaptive network with undirected coupling; III C general case: adaptive network with directed coupling. In Sec. IV we briefly investigate via numerical simulation if larger oscillator systems with $N = 50$ display a behavior in terms of adaptivity and synchronizability that is similar to $N = 50$. In Sec. V, we summarize and discuss our results.

II. MODEL

A. General model

We consider a general model of N oscillators $l \in [N] := \{1, \dots, N\}$ with adaptive coupling. The oscillator phase $\phi_l = \phi_l(t) \in \mathbb{T} = \mathbb{R}/2\pi\mathbb{Z}$ then evolves according to

$$\frac{\mathrm{d}\phi_l}{\mathrm{d}t} = \omega_l + \frac{1}{N}\sum_{m=1}^{N} \kappa_{lm}\, g(\phi_m - \phi_l) \tag{1}$$

with intrinsic frequencies ω_l. Oscillators l and m interact via the interaction function g and are coupled with the time-dependent coupling weight $\kappa_{lm} \in \mathbb{R}$. The coupling weights evolve according to

$$\frac{\mathrm{d}\kappa_{lm}}{\mathrm{d}t} = \varepsilon(\mathcal{A}(\phi_l - \phi_m) - \kappa_{lm}) \tag{2}$$

where the adaptation or learning rule $\mathcal{A} = \mathcal{A}(\phi)$ defines how the coupling adapts according to the oscillator phases (states); i.e., the adaptation/learning rule is defined via a local interaction between oscillator's phases. The second term with κ_{lm} guarantees boundedness of the coupling weights. The time scale at which adaptation may occur is set by ε: oscillator phases evolve on time scales ~ 1 and coupling adapts on a time scale $\sim 1/\varepsilon$.

Specifically, we consider the simplest version of such a model and suppose that g and $\mathcal{A}$ are periodic functions in ϕ. We may think of them as truncations of Fourier series to first order, i.e.,

$$g(\phi) = \sin(\phi + \alpha), \tag{3}$$

and

$$\mathcal{A}(\phi) = a_0 + a_1 \cos(\phi + \beta). \tag{4}$$

Thus, the oscillator dynamics is defined by the Kuramoto-

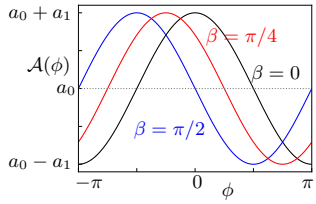

Figure 1. The adaptation rules $\mathcal{A}(\phi)$ for distinct values of adaptation shifts β (shown for $a_1 > 0$).

Sakaguchi model with phase-lag α; the adaptation/learning rule has an *adaptation offset*, $a_0 \neq 0$, and *adaptivity* a_1 (strength of adaptation). The adaptation rule is inspired by models of synaptic plasticity in neuroscience and can be related to models of neural spiking activity [9,10,12]. In this context, the *adaptation shift* β tunes the type of interaction: Restricting our attention to positive adaptivity, $a_1 > 0$, the following values of β, as illustrated in Fig. 1, may be interpreted in specific ways[10]:

1. Hebbian learning ($\beta = 0$): amplifies (or suppresses) the undirected coupling weight between oscillators that have phase difference close to 0 (or π).

2. Anti-Hebbian learning ($\beta = \pi$): amplifies (or suppresses) the undirected coupling weight between oscillators that have phase difference close to π (or 0).

3. Spike-time-dependent-plasticity (STDP) ($\beta = \pi/2$): amplifies (or suppresses) coupling weights between oscillators with phase difference close to $\pi/2$ (or $3\pi/2$).

Note that the 'self-couplings', $\kappa_{ll}(t)$, are decoupled from the oscillator phases; vice versa, if $g(0) = \sin\alpha = 0$, oscillators are independent from the self-coupling. But even if $\sin\alpha \neq 0$, the post-transient or asymptotic values $\kappa_{ll}(t \to \infty) \to a_0 + a_1 \cos\beta$ can be absorbed into the intrinsic frequencies, $\omega_l + \kappa_{ll}(\infty) \mapsto \omega_l$. We may therefore disregard all coupling terms κ_{ll}[37]. Furthermore, we may reduce the number of parameters involved by appropriately rescaling parameters and variables,

$$a_0 t \mapsto t, \quad \frac{\omega_l}{a_0} \mapsto \omega_l, \quad \frac{\kappa_{lm}}{a_0} \mapsto \kappa_{lm}, \quad \frac{\varepsilon}{a_0} \mapsto \varepsilon.$$

Since $\varepsilon > 0$, we restrict ourselves to $a_0 > 0$. Introducing the *(relative) adaptivity*, $a := a_1/a_0$, we then obtain the govern-

ing equations for the model:

$$\frac{\mathrm{d}\phi_l}{\mathrm{d}t} = \omega_l + \frac{1}{N}\sum_{m=1}^{N} \kappa_{lm} \sin(\phi_m - \phi_l + \alpha), \tag{5a}$$

$$\frac{\mathrm{d}\kappa_{lm}}{\mathrm{d}t} = \varepsilon(1 + a\cos(\phi_l - \phi_m + \beta) - \kappa_{lm}), \tag{5b}$$

where $l \neq m$.

Since $g(\phi)$ and $\mathcal{A}(\phi)$ only depend on phase differences, (5) is invariant to shifts in constant phase and frequency, i.e., $\phi_l(t) \mapsto \phi_l(t) + \Phi + \Omega t$ with constants $\Phi, \Omega \in \mathbb{R}$.

When $a = 0$, the model asymptotically strives to $\kappa_{lm} = 1$ for all $l, m \in [N]$, corresponding to the Kuramoto model with (rescaled) uniform stationary coupling. The emergent coherence in the model can be characterized by the order parameter

$$Z(t) = \frac{1}{N}\sum_{l=1}^{N} e^{\mathrm{i}\phi_l(t)}.$$

The Kuramoto model exhibits the following asymptotic behavior[7,38,39]. When the coupling is subcritical ($\kappa < \kappa_c$), $|Z| \to 0$ corresponding to low coherence; vice versa, for supercritical coupling ($\kappa > \kappa_c$), the order parameter approaches a constant positive value corresponding to partial coherence. The threshold in the continuum limit $N \to \infty$ is $\kappa_c = 2/(\pi g(0))$[39], where $g(\omega)$ is a unimodal frequency distribution with maximum $g(0)$ and standard deviation σ. Here we normalized the coupling κ to 1; thus, the synchronization threshold, σ_c, is indirectly determined via $1 = 2/(\pi g(0))$. Vice versa, if $a \neq 0$, we allow the network to be adaptive and we move away from the manifold corresponding to the Kuramoto model with stationary coupling.

a. Overview. Note that both Hebbian and anti-Hebbian learning is covered by $\beta = 0$ if both positive and negative values of a are taken into account; since we consider negative adaptivity, $a < 0$, we do not need to include the equivalent case of $\beta = \pi$ in our investigation. In addition to these special cases we are also interested in investigated mixed-type learning rules such as the case $\beta = \pi/4$, see Sec. III C 3.

B. Two oscillator model

We consider the minimal network with $N = 2$ oscillators. Introducing $\phi := \phi_1 - \phi_2$ and $\omega := \omega_1 - \omega_2$, the governing equations become

$$\frac{\mathrm{d}\phi}{\mathrm{d}t} = \omega + \frac{1}{2}\kappa_{12}\sin(\alpha - \phi) - \frac{1}{2}\kappa_{21}\sin(\alpha + \phi), \tag{6a}$$

$$\frac{\mathrm{d}\kappa_{12}}{\mathrm{d}t} = \varepsilon(1 + a\cos(\beta + \phi) - \kappa_{12}), \tag{6b}$$

$$\frac{\mathrm{d}\kappa_{21}}{\mathrm{d}t} = \varepsilon(1 + a\cos(\beta - \phi) - \kappa_{21}). \tag{6c}$$

This system of equations has the additional symmetries

$$(a, \beta) \mapsto (-a, \beta + \pi) \tag{7a}$$

$$(a, \alpha, \phi) \mapsto (-a, \alpha + \pi, \phi + \pi) \tag{7b}$$

$$(\alpha, \beta, \kappa_{12}, \kappa_{21}) \mapsto (-\alpha, -\beta, \kappa_{21}, \kappa_{12}), \tag{7c}$$

Due to (7a), we may restrict the parameter range to $-\pi/2 < \beta \leq \pi/2$; due to (7b), we may restrict the parameter range to $-\pi/2 < \alpha \leq \pi/2$; furthermore, (7c) allows to restrict either the range of β or α to positive values, and we chose to restrict $0 \leq \beta \leq \pi/2$. However, observe that all symmetry transformations also affect other parameters and variables; e.g., the symmetry (7b) effectively swaps (near-)phase-locked states where ϕ is close to zero, with (near-)antiphase states where ϕ is close to π. Thus, if a phase-locked stationary state is stable for $\alpha = 0$ with adaptivity a, then an antiphasic stationary state is also stable for $\alpha = \pi$ with $-a$. There are several other symmetries as listed in Appendix A.

Furthermore, we consider $\varepsilon > 0$. As our analysis will show, we find interesting nontrivial dynamic behavior for $\varepsilon = 0.2$ and we use this value throughout the analysis unless specified otherwise.

III. ANALYSIS

Certain parameter choices lead to effectively lower-dimensional dynamics. It is instructive to first consider these cases (Secs. III A and III B) before analyzing the more general case leading to three dimensional dynamics (Sec. III C).

A. Non-adaptive limit with stationary coupling (classical Kuramoto model)

Non-adaptive dynamics is obtained for two limiting cases: either $\varepsilon = 0$, so that κ_{12}, κ_{21} are constants; or the adaptivity is zero, $a = 0$, and the coupling weights asymptotically become identical with $\kappa_{12}(t), \kappa_{21}(t) \to 1$ as $t \to \infty$, irrespective of the value of β. In either cases, the system is effectively one-dimensional with the dynamics given by (6a), i.e., the system corresponds to the classical Kuramoto model. Since we are only interested in $\varepsilon > 0$ we consider the case of $a = 0$ and let $\kappa_{12} = \kappa_{21} = 1$ to consider the post-transient dynamics. Eq. (6a) can be cast as

$$\frac{\mathrm{d}\phi}{\mathrm{d}t} = \omega - \cos\alpha \sin\phi. \tag{8}$$

Since we restricted $\alpha \in (-\pi/2, \pi/2]$, we have $\cos\alpha \geq 0$. Excluding the effectively decoupled case with $\cos\alpha \neq 0$, we may rescale time and ω with $\cos\alpha$ to obtain

$$\frac{\mathrm{d}\phi}{\mathrm{d}t} = \omega - \sin\phi. \tag{9}$$

When the frequency mismatch exceeds the coupling, $|\omega| > 1$, there are no fixed points and the distance $\phi = \phi_1 - \phi_2$ keeps increasing, amounting to *drifting* oscillators. When the frequency mismatch is smaller, $|\omega| < 1$, we have the two equilibria

$$\phi_- := \arcsin\omega, \quad \phi_+ := \pi - \arcsin\omega, \tag{10}$$

ϕ_- is a stable equilibrium while ϕ_+ is unstable. These equilibria correspond to (frequency-)locked states with the two oscillators having constant phase difference. When the oscillators share their intrinsic frequencies, $\omega = 0$, the oscillators

are phase-locked . For $|\omega| = 1$, the two equilibria collide in a saddle-node bifurcation on an invariant cycle (SNIC). These drift/locked states, as well as the saddle-node bifurcation, remain as a basic dynamic structure when the system is adaptive with $a \neq 0$.

B. Adaptive network with undirected coupling ((anti-)Hebbian learning limit: $\beta = 0, \pi$)

1. Reduction

The adaptation rules in (6b) and (6c) for $\beta = 0, \pi$ attain identical structure and the three dimensional dynamics of (6) is asymptotically described by dynamics on a two dimensional subspace. To see this, we cast Eqs. (6b) and (6c) in terms of the difference $\Delta := \kappa_{12} - \kappa_{21}$ and sum $\Sigma := \kappa_{12} + \kappa_{21}$,

$$\frac{\mathrm{d}\Delta}{\mathrm{d}t} = \varepsilon(a[\cos(\beta+\phi) - \cos(\beta-\phi)] - \Delta) \tag{11a}$$

$$\frac{\mathrm{d}\Sigma}{\mathrm{d}t} = \varepsilon(2 + a[\cos(\beta+\phi) + \cos(\beta-\phi)] - \Sigma) \tag{11b}$$

Using $\beta = 0$ Eqs. (11) simplify to

$$\frac{\mathrm{d}\Delta}{\mathrm{d}t} = -\varepsilon\Delta \tag{12a}$$

$$\frac{\mathrm{d}\Sigma}{\mathrm{d}t} = \varepsilon(2[1 + a\cos\phi] - \Sigma) \tag{12b}$$

Defining $\kappa(t) := \kappa_{12}(t) = \kappa_{21}(t) = \Sigma(t)/2$, (6a) and (12b) become

$$\frac{\mathrm{d}\phi}{\mathrm{d}t} = \omega - \kappa\cos\alpha\sin\phi, \tag{13a}$$

$$\frac{\mathrm{d}\kappa}{\mathrm{d}t} = \varepsilon(1 + a\cos\phi - \kappa). \tag{13b}$$

This system describes the dynamics on a two-dimensional subspace, i.e. the plane defined by $\kappa_{12} = \kappa_{21}$ in the full $(\phi, \kappa_{12}, \kappa_{21})$ phase space. As is evident from inspecting (12a), this plane is globally attracting.

Eqs. (13) admit for two degenerate cases: (i) if $\omega = \cos\alpha = 0$, ϕ is constant and thus $\kappa(t) \to 1 + a\cos\phi$ exponentially fast; (ii) if $\cos\alpha = 0$ with $\omega \neq 0$, we have $\phi(t) = \phi_0 + \omega t$ so that oscillators drift apart and $\kappa(t)$ forever undergoes an oscillation.

Since we restricted $\alpha \in (-\pi/2, \pi/2]$, we may assume $\cos\alpha \geq 0$. Further restricting $\cos\alpha \neq 0$ we may rescale time and related parameters with $\cos\alpha$ and obtain

$$\frac{\mathrm{d}\phi}{\mathrm{d}t} = \omega - \kappa\sin\phi, \tag{14a}$$

$$\frac{\mathrm{d}\kappa}{\mathrm{d}t} = \varepsilon(1 + a\cos\phi - \kappa). \tag{14b}$$

2. Stability analysis

Equilibrium conditions are given by Eqs. (14b) and (14a) with

$$\kappa = 1 + a\cos\phi \tag{15}$$

and

$$\omega = \kappa\sin\phi = (1 + a\cos\phi)\sin\phi. \tag{16}$$

Using Euler's identity we may eliminate ϕ to obtain an equilibrium condition in κ only,

$$1 = \frac{\omega^2}{\kappa^2} + \frac{(\kappa-1)^2}{a^2}. \tag{17}$$

The equilibria for ϕ are given as

$$\tan\phi = \frac{\omega}{\kappa}\frac{a}{\kappa - 1} \tag{18}$$

as a function of κ. Equilibria (and their bifurcations) are shown in Fig. 2 for varying values of ω and a.

To determine the asymptotic stability of these equilibria, we consider the Jacobian of (14),

$$J = -\begin{bmatrix} \kappa\cos\phi & \sin\phi \\ \varepsilon a\sin\phi & \varepsilon \end{bmatrix}. \tag{19}$$

Using equilibrium conditions (15) and (16), we can eliminate ϕ to obtain the trace and determinant for equilibria,

$$\det(J^*) = \varepsilon(\kappa(\kappa-1)/a - a\omega^2/\kappa^2), \tag{20}$$

$$\mathrm{tr}(J^*) = \kappa(1-\kappa)/a - \varepsilon. \tag{21}$$

We seek to determine bifurcation curves in (ω, a)-parameter-space. Our system is planar so that saddle-node and Hopf bifurcations are determined via the conditions $\det(J) = 0$ and $\mathrm{tr}(J) = 0$ with $\det(J) > 0$, respectively. Bogdanov-Takens bifurcations occur at the intersection of these two conditions, i.e., $\det(J) = \mathrm{tr}(J) = 0$. Eliminating ϕ and κ corresponding to equilibria in $\det(J)$ or $\mathrm{tr}(J)$ appears not to be feasible since (17) neither can be solved for κ in closed form nor is there a suitable substitution to achieve the elimination. Instead, to determine the desired bifurcation curves we seek a parameterization of ω and a in terms of one of the equilibrium variables, κ.

a. Saddle-node bifurcation curve. To determine such a parameterization, instead of using the condition $\det J = 0$ for saddle-node bifurcations, we pursue another strategy. Solving the equilibrium condition (17) for

$$a(\kappa) = \pm\frac{\kappa(\kappa-1)}{\sqrt{\kappa^2 - \omega^2}} \tag{22}$$

and computing

$$\frac{\mathrm{d}a}{\mathrm{d}\kappa} = \pm(\kappa^3 + \omega^2(1-2\kappa))(\kappa^2-\omega^2)^{2/3}, \tag{23}$$

we find that $\mathrm{d}a/\mathrm{d}\kappa = 0$ corresponds to a saddle-node condition, resulting in

$$\omega_{\mathrm{SN}}(\kappa) = \pm\frac{\kappa^{3/2}}{\sqrt{2\kappa - 1}}. \tag{24}$$

With (24) and (22) (where (24) is inserted for ω), we have obtained the desired parameterization $(\omega_{\mathrm{SN}}(\kappa), a_{\mathrm{SN}}(\kappa))$ for the saddle-node bifurcation.

b. Hopf bifurcation curve. Solving $\mathrm{tr}(J^*) = 0$ for a in (21) we find that

$$a_{\mathrm{H}}(\kappa) = \kappa(1-\kappa)/\varepsilon. \tag{25}$$

From (17) we obtain the equilibrium value for

$$\omega_{\mathrm{H}}(\kappa) = \frac{\kappa}{a}\sqrt{a^2 - \kappa^2 + 2\kappa - 1}. \tag{26}$$

Hopf curves are thus determined via (25) and (26) with κ as parameter, provided that $\det(J^*)$ in (20) is positive. Note that all Hopf bifurcations in this system are subcritical so the limit cycles created in the Hopf bifurcations are unstable.

c. Homoclinic and heteroclinic bifurcations. When a limit cycle collides with a saddle point it gets destroyed in a homoclinic bifurcation. Homoclinic bifurcations have been determined numerically as follows. Since limit cycles in this planar system are unstable, Eqs. (14) have been numerically integrated backwards in time while continuing ω. The associated homoclinic bifurcation has been determined for a given value of a by determining the ω at which the limit cycle is destroyed in saddle collision. Doing so for several values of a allowed to construct the associated homoclinic bifurcation curve shown in Fig. 3. The same applies to heteroclinic bifurcations.

d. Bogdanov-Takens points. Curves of saddle-node, Hopf, and homoclinic bifurcations intersect in a codimension 2 Bogdanov-Takens bifurcation point (BT). This point is found by seeking solutions that simultaneously satisfy equilibrium conditions together with $\det(J) = \mathrm{tr}(J) = 0$.

e. Cusp bifurcation points. Another codimension 2 bifurcation point is the cusp bifurcation (CP) where two saddle-node bifurcations meet. Thus, CP points are located at $(\omega_{\mathrm{CP}}, a_{\mathrm{CP}}) = (0, \pm 1)$.

3. Stability and bifurcation diagrams

We explain the bifurcation scenarios and associated stability boundaries based on our previous analysis. We first observe that the bifurcation and stability diagram (see Figs. 2 and 3, respectively) exhibit certain symmetries regarding the reflection $\omega \mapsto -\omega$. It is easy to check that Eqs. (14), (17) and (18) obey the symmetry

$$(\phi, \omega) \mapsto (-\phi, -\omega), \tag{27}$$

which effectively swaps the labels of the two oscillators and thus preserves equilibria, their stabilities and bifurcations (as seen in Figs. 2, 3). A further symmetry that preserves equilibria is

$$(a, \phi) \mapsto (-a, -\phi + \pi), \tag{28}$$

but stability of the equilibria is not preserved as can be seen by inspecting the Jacobian in (19) (more specifically, saddle-node and cusp bifurcations are preserved, while Hopf bifurcations are not, see Figs. 3 and 2(b),(c), see also Appendix A).

The non-adaptive case ($a = 0$) represents the limit of the classical Kuramoto model (see Sec. III A). This case illustrates the perhaps most fundamental bifurcation organizing the structure of the stability diagram on a 'global' scale. When intrinsic frequencies are sufficiently similar, $\omega = \omega_1 - \omega_2 < 1$, oscillators lock their frequency; vice versa, if intrinsic frequencies are too dissimilar, $\omega > 1$, oscillator phases drift apart. Close to $\omega = 0$, oscillators are nearly in-phase, i.e., $\phi \approx 0$ (compare with Fig. 2 where $a \neq 0$); but the phase difference ϕ increases with larger $|\omega|$ until the locking breaks apart in a saddle-node bifurcation (black line) and a drifting state appears. This saddle-node bifurcation separates the stability regions for frequency-locked (L, light gray shaded region) and drifting (D, white region) solutions and can be followed throughout the stability diagram in Fig. 3. Note that this drift solution corresponds to a rotation on the cylinder $\mathbb{T} \times \mathbb{R}$.

For non-zero adaptivity ($a \neq 0$), the structure of the stability diagram in Fig. 3 is organized around two bifurcation points of codimension two, from where additional bifurcation curves emanate: i) cusp points (CP, black dots) located at $(\omega_{\mathrm{CP}}, a_{\mathrm{CP}}) = (0, \pm 1)$; and ii) Bogdanov-Takens points (BT, purple dots). Furthermore, several parameter regions of bi-stability (dark gray shaded regions, yellow regions) appear near the cusp bifurcation points and the saddle-node bifurcation leading up to the drifting solutions, respectively.

a. Positive adaptivity. We first consider positive adaptivity ($a > 0$). For smaller frequency mismatch ($\omega \lesssim 1$) and intermediate adaptivity ($0 < a < 1$), frequency-locked solutions (L, light gray shaded region Fig. 3) with positive coupling weights exist, stable nodes (black line in Fig. 2 (b)) closer to in-phase and saddles (black dashed line) closer to anti-phase configurations. For $a \geq 1$, two additional saddle-node bifurcation curves (black lines in Fig. 3 / black dots in Fig. 2 (a)) emerge in a cusp bifurcation (CP, black dot in Fig. 3) located at $(\omega_{\mathrm{CP}}, a_{\mathrm{CP}}) = (0, 1)$. Traversing these saddle-node bifurcation curves gives birth to an additional stable node and a saddle with negative coupling, see Fig. 2 (a). Thus, for $a > 1$, above the cusp point, between the inner SN bifurcation curves, we have a region of bi-stability (dark gray shaded region) with two stable locked solutions characterized by near in- and anti-phase configurations, respectively. For larger frequency mismatch ($\omega \gtrsim 1$), as we traverse the saddle-node bifurcation giving rise to the locked state (L), we first observe a region of bi-stability (yellow region) between the locked state (L) and a drift cycle (D). As the frequency mismatch ω is further diminished, the drift cycle collides with the saddle version of the locked state emanating from the saddle-node bifurcation and is thus destroyed in a heteroclinic bifurcation.

b. Negative adaptivity. Consider now negative adaptivity ($a < 0$). The symmetry (28) swaps near in-phase with anti-phase configurations and changes stabilities of equilibria. The overall bifurcation structure is thus similar to the one observed for $a > 0$; albeit, their structure is more intricate. We first restrict our attention to smaller frequency mismatch ($\omega < 1$). For $-1 < a < 0$, the saddle-node bifurcations (black line in Fig. 3 / black dot in Fig. 2 (c)) now give birth to an unstable node, which turns into an unstable spiral and

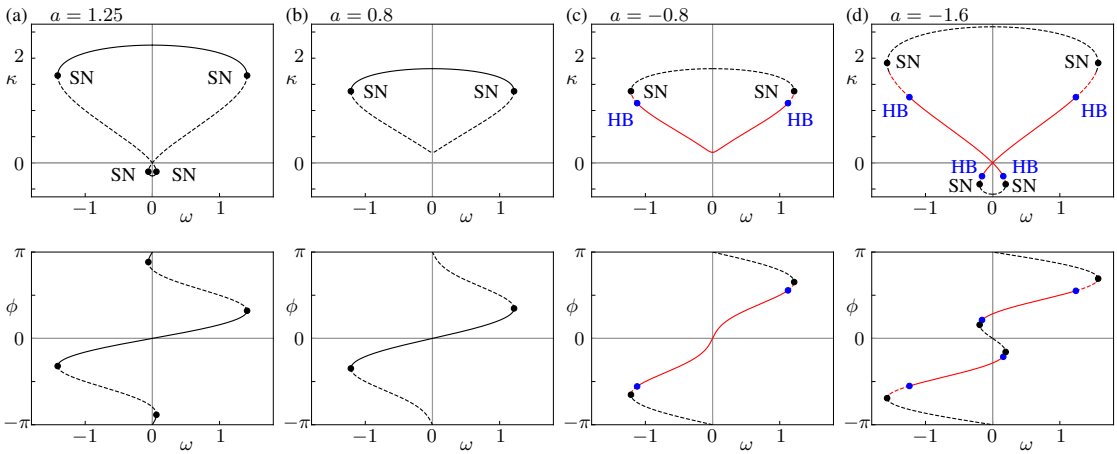

Figure 2. Bifurcation diagrams (equilibria only) in (ω, κ) and (ω, ϕ) for varying values of a (indicated as green lines in Fig.3) with $\alpha = \beta = 0$ and $\varepsilon = 0.2$. The diagrams show stable nodes (black lines), saddles, unstable nodes (both black dashed lines) stable spirals (red lines), and unstable spirals (red dashed lines). Unstable limit cycles (librations) (not shown) emerge from subcritical Hopf bifurcations.

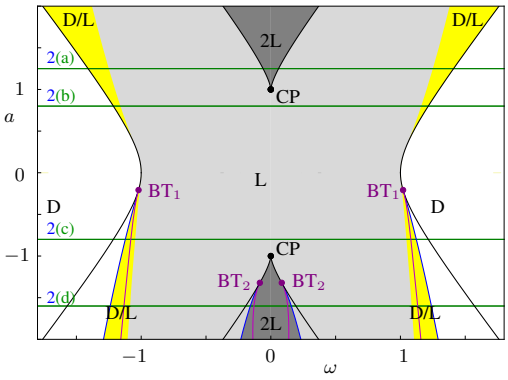

Figure 3. Stability diagram in (ω, a) for $\alpha = \beta = 0$ with $\varepsilon = 0.2$. (ω, a) parameter regions are shaded according to which stable states they contain: Drift (D) and/or locked states (L).

then a stable spiral (red line in Fig. 2 (c)), however now corresponding to a near in-phase state with positive but small coupling. We observe a cusp bifurcation (CP, black dot in Fig. 3) at $(\omega_{\text{CP}}, a_{\text{CP}}) = (0, -1)$. Below that, for smaller $a < -1$, a Bogdanov-Takens point (BT$_2$, purple dot in Fig. 3) appears on the new saddle-node bifurcation (black line in Fig. 3 / black dot in Fig. 2 (d)). BT$_2$ gives rise to a subcritical Hopf bifurcation (blue line in Fig. 3 / blue dot in Fig. 2 (d)) that stabilizes the second locked state, a stable spiral with small negative coupling and $\phi \approx \pm\pi/4$ (red line in Fig. 2 (d)). The unstable (libration) limit cycles emanating from the Hopf get destroyed in a homoclinic bifurcation (purple line in Fig. 3).

For larger frequency mismatch ($\omega > 1$), we observe a region of bi-stability (D/L, yellow region in Fig. 3) between locked (L) and drifting (D) states similar to the one observed for positive adaptivity, $a > 0$. However, there are important differences. First, below the Bogdanov-Takens point BT$_1$, the frequency-locked solution (L) loses stability in a subcritical Hopf bifurcation (blue line). More specifically, as shown in Fig. 2(c),(d), the saddle-node bifurcation (black dot) gives birth to a saddle (black dashed line) and an unstable node which first becomes an unstable spiral (red dashed line) and then becomes a stable spiral (red line) in a Hopf bifurcation (blue dot).

Second, for adaptivity values well above the BT$_1$ point, the drift cycle D is destroyed in a heteroclinic bifurcation; this scenario, however, appears to be quite different for adaptivity a somewhat below BT$_1$. On the boundary of the D/L (yellow region) and L regions (light gray shaded region) — before any heteroclinic bifurcation is possible to occur — the drift (limit) cycle loses its stability. Thus, trajectories emanating from the unstable drift end up spiraling into the stable spiral that arises in the Hopf bifurcation related to BT$_1$.

To summarize the respective differences regarding stability changes occurring for $a < 0$ and $a > 0$, the presence of Bogdanov-Takens bifurcation points BT$_1$ and BT$_2$ diminishes the size of the L locking region and the 2L bi-stability region (dark gray shaded region in Fig. 3). Furthermore, the size of the bi-stable D/L region is also effectively diminished.

C. Adaptive network with directed coupling

We now allow for arbitrary values of β; in general, this may lead to asymmetric coupling weights $\kappa_{lm} \neq \kappa_{ml}$ corresponding to a directed network.

1. Stability analysis

We first investigate equilibria of the full three dimensional system in Eqs. (6) which gives rise to the following fixed point conditions:

$$2\omega = \kappa_{21}\sin(\alpha+\phi) - \kappa_{12}\sin(\alpha-\phi), \tag{29a}$$
$$\kappa_{12} = 1 + a\cos(\beta+\phi) \tag{29b}$$
$$\kappa_{21} = 1 + a\cos(\beta-\phi) \tag{29c}$$

Eliminating κ_{12} and κ_{21}, we obtain a condition that only depends on ϕ and guarantees the existence of an equilibrium,

$$\omega = (\cos\alpha + a\cos(\alpha-\beta)\cos\phi)\sin\phi. \tag{30}$$

Note that Eqs. (29b), (29c) and (30) provide us with a parameterization of an equilibrium curve for $(\omega, \kappa_{12}, \kappa_{21})$ in variable ϕ.

To determine the stability of equilibria, we calculate the Jacobian for (6),

$$J = \begin{bmatrix} J_{\phi\phi} & \frac{1}{2}\sin(\alpha-\phi) & -\frac{1}{2}\sin(\alpha+\phi) \\ -\varepsilon a\sin(\beta+\phi) & -\varepsilon & 0 \\ \varepsilon a\sin(\beta-\phi) & 0 & -\varepsilon \end{bmatrix},$$

where $J_{\phi\phi} = -(\kappa_{12}\cos(\phi-\alpha) + \kappa_{21}\cos(\phi+\alpha))/2$. The Jacobian has the eigenvalues

$$\lambda_{1,2} = \mu \pm \sqrt{\delta}, \tag{31a}$$
$$\lambda_3 = -\varepsilon, \tag{31b}$$

where

$$\mu = -\frac{A}{4} - \frac{\varepsilon}{2}, \tag{32a}$$
$$\delta = \frac{\varepsilon}{2}(aB - A) + \frac{1}{16}(A+2\varepsilon)^2, \tag{32b}$$
$$A := \kappa_{12}\cos(\alpha-\phi) + \kappa_{21}\cos(\alpha+\phi), \tag{32c}$$
$$B := \cos(\alpha+\beta) - \cos 2\phi\cos(\alpha-\beta). \tag{32d}$$

Since by definition $\lambda_3 < 0$, it suffices to only consider $\lambda_{1,2}$.

If an equilibrium point satisfies $\mu^2 = \delta$, one eigenvalue becomes zero, and the equilibrium is a saddle-node point. One could use this condition to determine the associated saddle-node curves, but we instead use the following consideration. Since the equilibrium condition (30) only depends on ϕ, the conditions for an equilibrium and for a saddle-node bifurcation are reduced to a problem in a single variable, ϕ. Accordingly, we require in addition to (30) that $\mathrm{d}\omega/\mathrm{d}\phi = 0$. Solving the resulting two conditions for (ω, a) results in a parameterization of the saddle-node curves in ϕ,

$$\omega_{\mathrm{SN}} = -\cos\alpha\sec 2\phi\sin^3\phi, \tag{33a}$$
$$a_{\mathrm{SN}} = -\cos\alpha\cos\phi\sec(\alpha-\beta)\sec 2\phi. \tag{33b}$$

Next, we consider equilibria undergoing Hopf bifurcations. If a given equilibrium satisfies $\mu = 0, \delta < 0$, the real part of a complex conjugated pair of eigenvalues vanishes and the equilibrium is a Hopf point. We find a parameterization for the Hopf curves as follows. First, we require that the equilibrium condition in (30) is satisfied. Second, after substituting (29b) and (29c) into (32c) we require that $\mu = 0$. Solving the two resulting conditions for (ω, a) we obtain

$$\omega_{\mathrm{H}} = \frac{(\varepsilon\cos\alpha\cos\beta\cos\phi + (\cos\alpha + \varepsilon\cos\phi)\sin\alpha\sin\beta)\sin\phi}{\sin\alpha\sin\beta\sin^2\phi - \cos\alpha\cos\beta\cos^2\phi}, \tag{34a}$$

$$a_{\mathrm{H}} = \frac{\varepsilon + \cos\alpha\cos\phi}{\sin\alpha\sin\beta\sin^2\phi - \cos\alpha\cos\beta\cos^2\phi}. \tag{34b}$$

Now $(\omega_{\mathrm{H}}, a_{\mathrm{H}})$ with parameter ϕ delineates a Hopf curve provided that $\delta < 0$ in (32b).

Finally, if $\mu = \delta = 0$, two eigenvalues are zero and the equilibrium is a Bogdanov-Takens point. Thus, simultaneously solving $\mu = \delta = 0$ together with the fixed point conditions (29), given a value of ε we are able to obtain $(\phi, \kappa_{12}, \kappa_{21}, a, \omega)$ at a Bogdanov-Takens point.

2. Dynamics for $\beta = \pi/2$

We let $\beta = \pi/2$ and first discuss the simplest case with $\alpha = 0$. We consider locked states and assume that the equilibrium conditions (29b) and (29c) are satisfied. Substituting these two conditions into (6a) we see that the third equilibrium condition reduces to $\omega = \sin\phi$. The resulting equilibria are

$$\phi = \begin{cases} \pi - \arcsin\omega \\ \arcsin\omega, \end{cases} \tag{35a}$$
$$\kappa_{12} = 1 - a\omega, \tag{35b}$$
$$\kappa_{21} = 1 + a\omega. \tag{35c}$$

The third equilibrium condition, $\omega = \sin\phi$, informs us that a saddle-node bifurcation occurs for $\omega = \pm 1$, regardless of the value of a. The associated bifurcation curve is therefore the straight black line shown in Fig. 4(a). We are dealing with a special limiting case: for $|\omega| < 1$, the oscillators are locked; for $|\omega| > 1$, they are drifting. Thus, contrary to other parameter choices considered in this study, the dynamics and bifurcations do not increase in complexity as a is varied. We can rationalize this as follows. The full dynamics in (ϕ, Δ, Σ) are given by (6a) and (11):

$$\frac{\mathrm{d}\phi}{\mathrm{d}t} = \omega - \frac{1}{2}\Sigma\cdot\sin\phi \tag{36a}$$
$$\frac{\mathrm{d}\Delta}{\mathrm{d}t} = -\varepsilon(2a\sin\phi + \Delta) \tag{36b}$$
$$\frac{\mathrm{d}\Sigma}{\mathrm{d}t} = \varepsilon(2-\Sigma) \tag{36c}$$

Since $\Sigma(t) \to 2$ exponentially fast as $t \to \infty$, the asymptotic dynamics is attracted to the invariant two-dimensional subspace whose dynamics is governed by

$$\frac{\mathrm{d}\phi}{\mathrm{d}t} = \omega - \sin\phi, \tag{37a}$$
$$\frac{\mathrm{d}\Delta}{\mathrm{d}t} = -\varepsilon(2a\sin\phi + \Delta). \tag{37b}$$

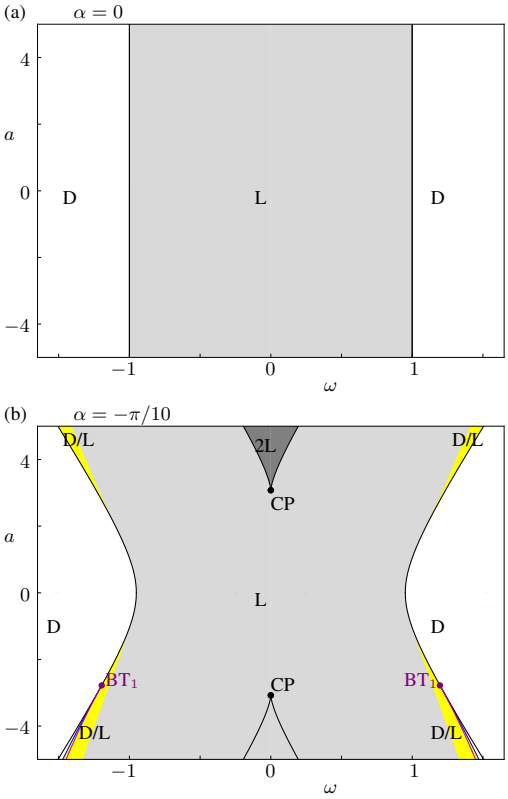

Figure 4. Stability diagrams for $\beta = \pi/2$. (ω, a) parameter regions are shaded according to which stable states they contain: Drift (D) and/or locked states (L).

While the variable ϕ drives Δ, its dynamics is independent of Δ. Thus, we effectively observe the one-dimensional dynamics known for the Kuramoto model (9) discussed in Sec. III A.

For $\beta = \pi/2$ and arbitrary α, the dynamics is

$$\frac{\mathrm{d}\phi}{\mathrm{d}t} = \omega + \frac{1}{2}\kappa_{12}\sin(\alpha - \phi) - \frac{1}{2}\kappa_{21}\sin(\alpha + \phi), \quad (38a)$$

$$\frac{\mathrm{d}\kappa_{12}}{\mathrm{d}t} = \varepsilon(1 - a\sin\phi - \kappa_{12}), \quad (38b)$$

$$\frac{\mathrm{d}\kappa_{21}}{\mathrm{d}t} = \varepsilon(1 + a\sin\phi - \kappa_{21}). \quad (38c)$$

As is easily checked, this system has the symmetry $(a, \alpha) \mapsto (-a, -\alpha)$. Since we were allowed to limit $\alpha \in (-\pi/2, \pi/2]$ in the original governing equations (6), we may restrict α further to either $[-\pi/2, 0]$ or $[0, \pi/2]$ while observing this symmetry.

To keep the analysis manageable, we consider only $\alpha = -\pi/10$. The resulting stability diagram is shown in Fig. 4(b). Even though this is just a small deviation, the bifurcation landscape differs drastically from the case where $\alpha = 0$. As was

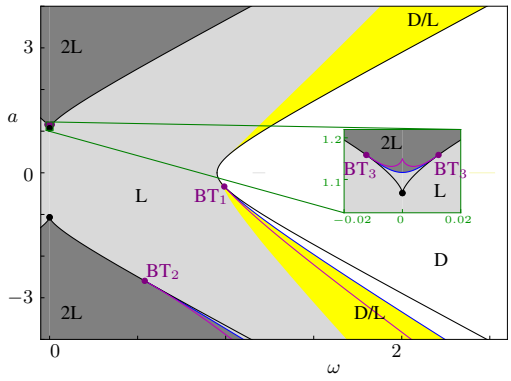

Figure 5. Stability diagram for $\alpha = \pi/10, \beta = \pi/4$. (ω, a) parameter regions are shaded according to which stable states they contain: Drift (D) and/or locked states (L).

the case for $\alpha = \beta = 0$ (Fig. 3), the stability diagram is symmetric regarding $\omega \mapsto -\omega$. More precisely, this symmetry also swaps oscillator indices,

$$(\phi, \omega, \kappa_{12}, \kappa_{21}) \mapsto (-\phi, -\omega, \kappa_{21}, \kappa_{12}), \quad (39)$$

and preserves equilibria, their stabilities, as well as all bifurcations since we are merely renaming the oscillators. Moreover, equilibria, and the SN and cusp bifurcations are symmetric about $a \mapsto -a$ (see Appendix A for an explanation), i.e.,

$$(a, \phi, \kappa_{12}, \kappa_{21}) \mapsto (-a, -\phi + \pi, \kappa_{21}, \kappa_{12}). \quad (40)$$

Note that these two symmetries are evident in all stability diagrams shown in this work, i.e., Figs. 3, 4, 5, and 6(a).

3. *Dynamics for* $\beta = \pi/4$

Next we consider the case where $\beta = \pi/4$. The stability diagram for $\alpha = 0$ (not shown) is qualitatively identical to the one obtained for $\alpha = \beta = 0$ (Fig. 3). Therefore, we instead consider small deviations from $\alpha = 0$, i.e., $\alpha = \pm\pi/10$.

a. Phase-lag $\alpha = \pi/10$. First, we consider the stability diagram for $\alpha = \pi/10$, see Fig. 5. There are three distinct Bogdanov-Takens points (BT_1 and BT_2 in the main plot of Fig. 5 and (two) BT_3 in the inset) which organize the bifurcation structure. The Hopf curves (blue lines) emanating from all three Bogdanov-Takens points (BT_1, BT_2, BT_3) are subcritical. These Hopf curves are adjacent to SN curves (black lines) giving birth to saddles and unstable nodes. The unstable nodes turn into unstable spirals, and, when undergoing the Hopf bifurcations, into stable spirals. The homoclinic curves (purple lines) adjacent to the SN curves destroy the unstable (libration) limit cycles created in the subcritical Hopf bifurcations.

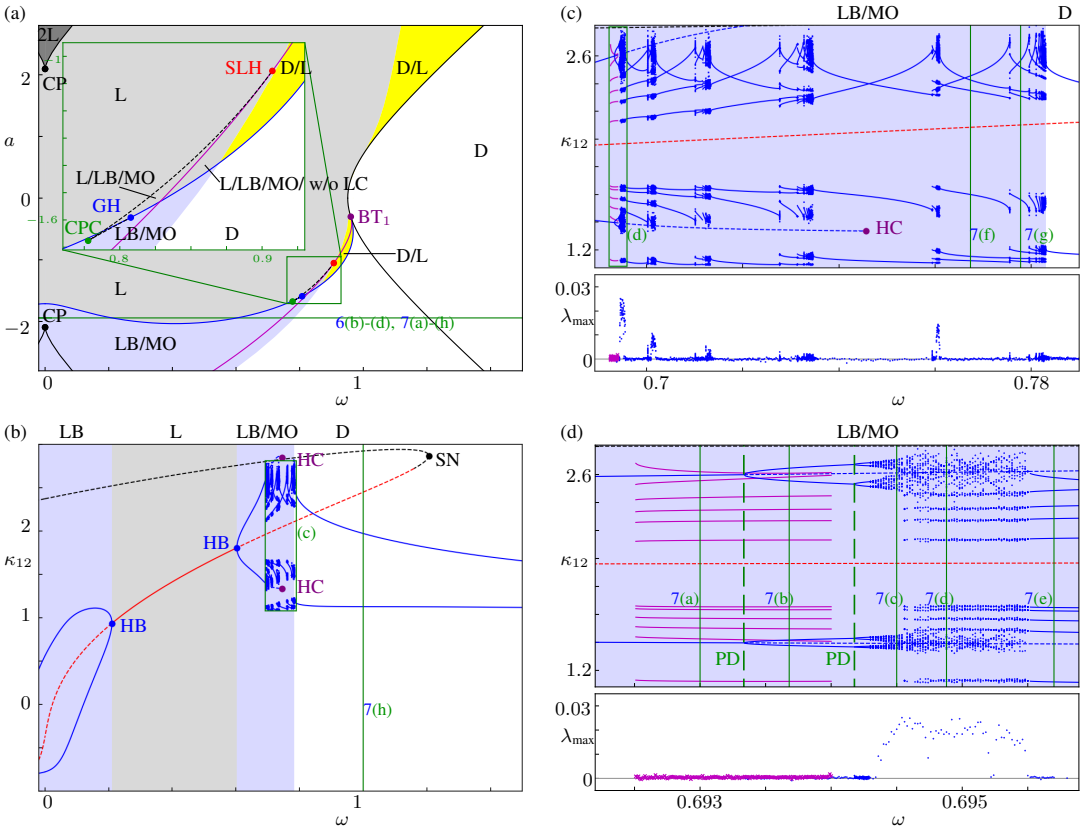

Figure 6. Dynamics for $\alpha = -\pi/10, \beta = \pi/4$. (a): stability diagram. (ω, a) parameter regions are shaded according to which stable states they contain: Drift (D, pure rotation around cylinder) locked states (L), librations (LB, periodic or chaotic), mixed (libration / rotation) drift oscillations (MO, periodic or chaotic). (b): Bifurcation diagram for $\alpha = -\pi/10, \beta = \pi/4, a = -1.9425$ (value of a is marked as green line in (a)). The diagram shows stable nodes (black lines), saddles, unstable nodes (both black dashed lines) stable spirals (red lines), unstable spirals (red dashed lines), stable oscillations (local extrema marked in blue) and unstable limit cycles (local extrema marked as blue dashed lines). (c): magnification of (b) (see green rectangle in (b)). The oscillations (LB/MO) alternate between periodic and chaotic as ω increases, and for $\omega > 0.78299$ the oscillations are exclusively pure rotation drift states (D). (d): magnification of (c) (see green rectangle in (c)). The first PD bifurcation (left green dashed line) produces an unstable limit cycle (blue dashed line) and a stable, period-2 limit cycle (LB, blue) which undergoes a second PD bifurcation (right green dashed line) and then a cascade of PD bifurcations (*not* marked, for readability), leading to stable chaos. (An MO state co-existing with the limit cycle is marked in magenta for dinstinguishability.) At $\omega \approx 0.6955$, the stable chaotic attractor turns into a stable periodic oscillation. The maximum Lyapunov exponent $\lambda_{\max}$ of the stable oscillatory states is shown beneath. For further explanations see text. For phase portraits of the oscillations see Fig.7.

b. Phase-lag $\alpha = -\pi/10$. Second, we consider the stability diagram for $\alpha = -\pi/10$ in Fig. 6. The resulting dynamics become far more involved when compared to the previously considered cases. The Hopf curve (blue line) that emanates from the BT_1 point (purple dot in Fig. 6(a)) contains a Generalized Hopf[40] (GH) point located at (ω_{GH},a_{GH}) (blue dot in Fig. 6(a)), which separates the Hopf curve (blue line) into a supercritical segment (below GH), and a subcritical segment (above GH).

Regime of subcritical Hopf bifurcations ($a > a_{GH}$). The subcritical Hopf curve (blue line in Fig. 6(a)) produces unstable (libration) limit cycles, which may undergo a saddle-node-of limit cycles (SNLC) bifurcation (black dashed line) before they die in a homoclinic bifurcation (purple line). The homoclinic bifurcation curve, which originates in the point BT_1 (purple dot), was found via numerical continuation using MatCont[41]. Below the GH point (blue dot), there are two branches of SNLC bifurcations which meet in a cusp of SNLCs (CPC, green dot). Thus, between the GH and the CPC points, limit cycles produced in the Hopf bifurcation (blue

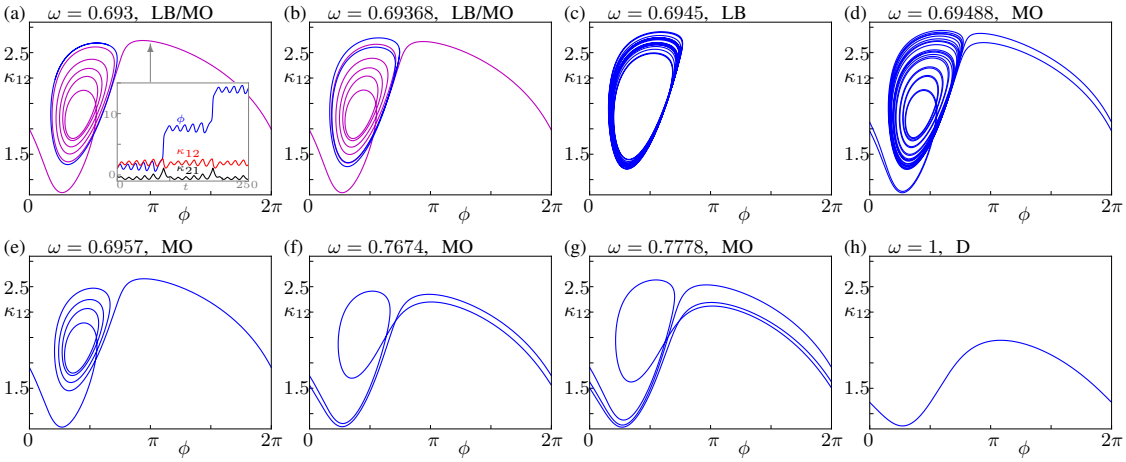

Figure 7. Regime of supercritical Hopf bifurcations ($a < a_{\mathrm{GH}}$): phase portraits of stable oscillations for $\alpha = -\pi/10, \beta = \pi/4, a = -1.9425$ and varying ω (shown as green lines in Figs. 6(b)-(d)). (a),(b): period-1 (a) or period-2 (b) libration cycle (LB, blue) co-exists with mixed rotational / librational drift cycle (MO, magenta). (c): chaotic libration (LB, blue). (d): chaotic mixed oscillation (MO), consisting of rotations and librations. (e): periodic MO with 1 rotation and 4 librations (blue). (f): periodic MO with 2 rotations and 1 libration. (g): periodic MO with 3 rotations and 1 libration. (h): pure rotation drift cycle (D, blue). See text for further details.

line) undergo *two* SNLC bifurcations before dying in the homoclinic bifurcation (purple line). One of the SNLC branches (black dashed line) meets the homoclinic bifurcation curve (purple line) in a point which we call SLH (red dot).

Regime of supercritical Hopf bifurcations ($a < a_{\mathrm{GH}}$). The supercritical Hopf bifurcations (blue line in Fig. 6(a)) below the GH (blue dot) produce stable (libration) limit cycles (LB) which can only exist on the same side of the supercritical Hopf curve as the unstable spirals, i.e., in the blue region between the HB curve (blue line) and the HC curve (purple line) that destroys the limit cycles. However, the stable limit cycle can be destroyed / destabilized before reaching the HC bifurcation (purple line) in an intriguing bifurcation scenario, which we now explain. Thereby, we let $a = -1.9425$ and follow the green line in the diagram Fig. 6(a)) while varying ω, and we also show example trajectories for chosen values of ω in Fig. 7.

After the supercritical Hopf bifurcation (right blue dot in Fig. 6(b)), i.e. for increasing ω, the stable (libration, LB) limit cycle (blue in Figs. 6(b),(d) and 7(a)) undergoes a Period-Doubling (PD) bifurcation (left green dashed line in Fig. 6(d)). The resulting stable limit cycle (blue in Figs. 6(d) and 7(b)) has period-2, i.e., it winds around twice per period. The original, period-1 cycle has become unstable (blue dashed line in Fig. 6(d)) in the PD (left green dashed line in Fig. 6(d)) and the associated branch ultimately is destroyed in the homoclinic bifurcation (purple dot in Fig. 6(b),(c)). Remarkably, the libration cycle LB co-exists with a (rotational) drift limit cycle in the region of period-1 and period-2 cycles, see magenta curves in Fig. 6(d) and magenta trajectories in Fig. 7 (a) and (b). This drift limit cycles consists of rotations *and* librations, we therefore refer to it as a mixed oscillation (MO). While the precise nature of the bifurcation mechanism giving rise to this MO on the left for smaller ω remained elusive to our analysis, inspection of trajectories for larger ω on the right strongly suggests that this MO drift cycle is destroyed in a collision with the unstable period-1 version of the libration cycle (blue dashed line in Fig. 6(d)).

As we increase ω further, the stable period-2 cycle undergoes a period doubling cascade (PDs are not explicitly marked to improve readability) resulting in a chaotic attractor with ϕ bounded, i.e., it can (still) be seen as a libration LB (blue in Figs. 6(c), (d) and 7(c)). To characterize this chaotic motion we numerically estimated the maximum Lyapunov exponent λ_{max}, and we found that $\lambda_{\mathrm{max}} > 0$ (close to zero) throughout the (non-)chaotic ranges of ω (Fig. 6(c),(d)). (Fluctuations in λ_{max} while varying ω are due to the fact that phase points of the original and the perturbed trajectory can lie anywhere on the chaotic attractor by the simulation time λ_{max} is computed.)

This chaotic attractor can be seen as a chaotic libration, since ϕ does not rotate around the cylinder $\mathbb{T} \times \mathbb{R}$ (Fig. 7(c)). Remarkably, as ω is further increased, the chaotic attractor at some point also includes oscillations characterized as *rotations*, where ϕ revolves around the cylinder (Fig. 7(d)), in a fashion that is reminiscent of *phase slips*. More precisely, the trajectory librates a number of times, until it escapes and becomes a rotation with drift character, while, however, remaining chaotic in nature. Presumably, this behavior is akin to a mixed mode oscillation seen characteristic of slow-fast systems, which is a reminiscence from low ε (recall that we use a fairly large $\varepsilon = 0.2$ here). Eventually, as ω is increased even further, the cycle ceases to display chaoticity and becomes a periodic oscillation including both librations (of a certain period) and (drift) rotations (Fig. 7(e)), which we therefore refer to as *mixed oscillations* (MO; not to be confused with mixed

mode oscillations). Ultimately, for $\omega > 0.78299$, the librations disappear and the cycle is a purely rotational drift cycle (Fig. 7(h)). This is remarkable, since — as already noted further above — a stable MO drift cycle was already present for smaller ω (magenta curves in Figs. 6(c),(d) and 7(a),(b)), destroyed in a bifurcation scenario different from the scenario seen here. Thus, the (rotational / librational) drift cycles just described are indeed distinct, as they seem to emerge from the libration cycles originally born in the supercritical Hopf bifurcation. To summarize, stable oscillations encountered are all either non-drifting libration cycles (LB, periodic or chaotic), purely rotational drift states (D, periodic), or mixed rotational / librational drift oscillations (MO, periodic or chaotic).

Furthermore, note that MO states exist, for $a = -1.9425$, in the range $\omega \in [0.69456, 0.78299)$ (Figs. 6(c) and 7(d)-(g)), where subintervals hosting periodic cycles alternate with subintervals hosting (aperiodic) chaotic motion. This was found via quasi-continuation of the stable oscillatory states in the interval $\omega \in [0.693, 1.25]$. Interestingly, the respective number of rotations and librations per period of the oscillation is different for each periodic subinterval (see Figs. 7(e)-(g)). Finally, based on quasi-continuation of the drift states in the direction of $\omega \to 0$ for several values of a, we find that stable purely rotational drift states (D) exist only in the white regions and yellow regions in Fig. 6(a). While the blue region *may* contain all aforementioned types of LB and MO cycles, none of these types emerges everywhere inside of the blue region; for readability, we do not distinguish existence regions for each type individually.

IV. SIMULATIONS FOR $N = 50$ OSCILLATORS

In Sec. III, we have studied in detail the behavior of the system (5) for $N = 2$ oscillators. The question abounds whether some of the behavior for $N = 2$ carries over to a larger version of the system with $N = 50$ oscillators. In order to address this question we restrict our attention to the simplest case with parameters $\alpha = \beta = 0, \varepsilon = 0.2$ (see Figs. 2, 3 for the results obtained for $N = 2$). While we could tune the frequency mismatch ω between the two oscillators, for the many oscillator system, we let the intrinsic frequencies ω_l follow a normal distribution with zero mean and standard deviation σ. Furthermore, instead of drawing these frequencies randomly, we constructed them via a an equidistant set of points mapped to the interval $[-3\sigma, 3\sigma]$ via the inverse error function. This symmetrization eliminates potential random effects that might otherwise obscure the dynamic effects we are interested in, such as to render comparison to the case of $N = 2$ more immediate.

We study the dynamic asymptotic behavior of this system on a grid in (σ, a) parameter space, the results of which are summarized in Fig. 8(a). We may distinguish four states: the (frequency-)locked state (L), the antipodal state (AP, which is a special kind of locked state), and two oscillatory states, partial coherence (P) and drift (D). The frequency-locked state (where all $\mathrm{d}\phi_l/\mathrm{d}t, \mathrm{d}\kappa_{lm}/dt$ tend to zero after some transient) and the drift state (where all $\frac{\mathrm{d}\phi_l}{\mathrm{d}t}$ stay non-zero) were already observed for the $N = 2$ system (L and D states, respectively). Note that the partially coherent state can be interpreted as a mixture of both L and D states, in the sense that the N oscillators are split into a frequency-locked and a drifting subset — naturally, this state requires $N > 2$ in order to be observed.

In the antipodal state (Fig. 8(b)), the phases of oscillators split into two groups inside which phases differ only very little from one another, but in between the groups phases differ by about π, i.e., the two oscillator groups are antipodal to one another on the phase circle; $\mathrm{d}\phi_l/\mathrm{d}t, \mathrm{d}\kappa_{lm}/\mathrm{d}t$ tend to zero asymptotically in time. This special configuration of the phases also impacts the coupling on the network: κ_{lm} that represent couplings between oscillator pairs residing in the same population (distinct populations) assume values close to the maximum possible value $1 + a$ (the minimum possible value $1 - a$), see black (white) κ_{lm} values in Fig. 8(b). Note that the antipodal state occurs when the distribution of ω_l is sufficiently narrow and the adaptivity $a > 0$ is sufficiently strong. This state may be interpreted as a corollary to the 2L coexistence observed for $N = 2, \alpha = \beta = 0, a \gg 0, |\omega| \ll 1$ (see Fig. 2(a)), where the two oscillators either occupy a phase configuration with 0 or π difference — here, oscillators form groups that mutually adhere to either of the two configurations. Note that a similar correspondence applies to the coupling weights both at the upper and the lower end of the applicable κ range.

For the (frequency-)locked state L (Fig. 8(c)), all phases are close to one another — thus, also the κ_{lm} are close to $1 + a$. Topologically, this essentially corresponds to an all-to-all network. This state is thus interpreted as the corollary of the locked state L for $N = 2$, see Fig. 2(b) for small ω.

For the partially coherent state P (in Fig. 8(d)), most oscillators are locked (blue dots), while others are drifters (red dots). Coupling weights κ_{lm} where l and/or m can be associated with drifting oscillators are thus oscillatory (red curves in Fig. 8(d)). By contrast, the locked oscillators (blue dots in Fig. 8(d)) display vanishingly small dynamic frequencies, thus the κ_{lm} for which neither l nor m are drifting oscillate close to $1 + a$ and with very small amplitude (blue time traces in Fig. 8(d)).

Just as for the $N = 2$ state, the locked state L occurs for both positive and negative a. For $N = 50$ and $a < 0$ with σ small, we observe locked states with oscillatory transients (corresponding to stable foci for $N = 2$) whose κ_{lm} are mostly close to the minimal value $1 - a$, in analogy to the case of $N = 2$ oscillators (see Fig. 2(c)).

For the $N = 2$ system, we found that (co)existence of one (L) or two (2L) stable locked state(s) is guaranteed for $|a|$ sufficiently large. Interestingly, Fig. 8(a) suggests that there is a stable locked state for $a > 0$ sufficiently large; yet, for $a < 0$ it appears as if the region of stable locked states is diminished in favor of partially coherent, or, even drift states. It would be interesting to investigate this aspect further in future research.

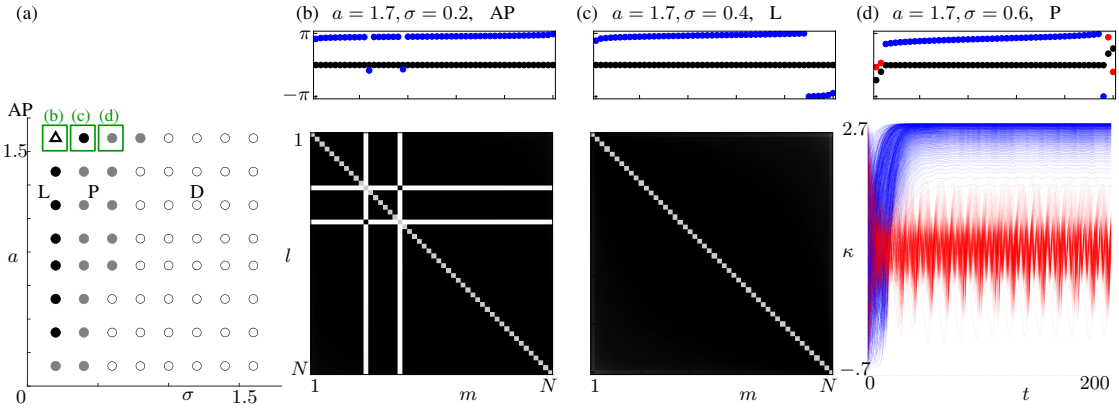

Figure 8. Summary of simulation results for $N = 50$ oscillators with $\alpha = \beta = 0, \varepsilon = 0.2$. (a) Stability diagram for varying a and σ summarizes the four post-transient final states (as observation for one realization only): antipodal (AP, triangle), locked (L, black circles), partially coherent (P, gray circles), drift (D, empty circles). Panels (b)-(d) display the behavior observed for three distinct parameter values (highlighted with green rectangles in (a)), i.e., AP for $a = 1.7, \sigma = 0.2$ (b), L for $a = 1.7, \sigma = 0.4$ (c), and P $a = 1.7, \sigma = 0.6$ (d), respectively. The top row in the panels displays phases (blue/red dots for locked/drifting oscillators) as well as dynamic frequencies (black dots) at the final simulation time T. The bottom row in panels (b) and (c) features the κ matrices at final time $T = 1500$, where white and black pixels correspond to $1 - a = -0.7$ and $1 + a = 2.7$, respectively (both matrices have zero diagonal shown in gray). The bottom row in panel (d) presents the time evolution of $\kappa_{lm}(t)$ during $0 \leq t \leq T = 200$ (transients have subsided for $t \leq 50$).

V. DISCUSSION

The model in Eqs. (5) is a Kuramoto-Sakaguchi model with phase-lag α and coupling weights that adapt according to a learning rule with adaptivity strength a and adaptation shift β. Our bifurcation analysis concerns the case of $N = 2$ oscillators, for which we — chiefly — may distinguish three cases: (i) the non-adaptive limit with stationary coupling ($a = 0$); (ii) the adaptive network with undirected coupling ($\beta = 0$ (or $\beta = \pi$) can be interpreted as a Hebbian (or anti-Hebbian) learning rule); and (iii) the adaptive network with directed coupling (arbitrary β). The non-adaptive limit ($a = 0$) trivially reduces to the classical Kuramoto model, where, for frequency locking to occur, the frequency mismatch must be smaller than the coupling that is rescaled to 1. Considering the case of undirected coupling ($\beta = 0$), we first observe that deviating from the non-adaptive limit ($a = 0$) with non-zero adaptivity ($a \neq 0$) leads to an overall larger locking region L, i.e., larger frequency mismatch is required to break locking. It is interesting to note that in the context of forced oscillations, the mode-locking region corresponds to an Arnol'd tongue; indeed, the strength of adaptivity could be related to a forcing strength, at least in the limit of slow adaptation ($\varepsilon \to 0$).

Furthermore, smaller frequency mismatch $|\omega|$ and sufficiently large adaptivity a allow for bi-stable regions 2L where two frequency locked modes co-exist, i.e., anti-phase (antipodal) configurations co-exist in addition to in-phase configurations. For larger $|\omega|$ and $a \neq 0$, a further bi-stability region D/L appears where locked states co-exist with drift cycles (rotations). While this general picture prevails for both positive and negative adaptivity, the situation is slightly more complicated in the region with $a < 0$, where additional bifurcations diminish the width of the various (bi-)stable regions (L, 2L and D/L). Note that drift cycles correspond to rotations around the cylindrical phase space, whereas Hopf bifurcations give rise to libration limit cycles; however, in the case of directed adaptive networks, these cycles remain always unstable.

We found that similar bifurcations scenarios also occur for directed adaptive networks with $\beta \neq 0$ and $a > 0$; however, even more intriguing dynamics is seen when $a < 0$ and $\beta = \pi/4, \alpha = -\pi/10$. Chiefly, the presence of a generalized Hopf bifurcation (GH) organizes a complex structure of bifurcations (including sub-/supercritical Hopf, saddle-node of limit cycles (SNLC), cusp of cycles (CPC), a homoclinic and SLH bifurcations, similar to a scenario seen for a system of Theta neurons, see Ref. 42); in particular, the GH enables a supercritical Hopf bifurcation for $a < 0$ that gives birth to stable librations. These libration cycles undergo a period-doubling cascade to chaos. Remarkably, period-1 and period-2 cycles may co-exist with a rotional drift cycle characterized by a non-trivial winding number; it appears to be destroyed in a collision with the unstable period-1 cycle emerging from the first period-doubling bifurcation before the stable libration cycle becomes chaotic. However, the period-doubling cascade of these librations features a surprise. As ω increases, after the librations become chaotic, they change to a mixed behavior characterized by features of both libration and rotation. The winding number of the libration changes, and mixed oscillations alternate between chaotic and periodic, until for large ω one finds a regular period-1 rotational drift cycle.

One would expect that the analysis of the $N = 2$ oscillator system might capture some of the dynamic behavior seen in larger systems. Our simulations for undirected networks ($\beta = 0$) with $N = 50$ revealed that such a correspondence exists, albeit with certain limitations. On one hand, we find a

relatively good correspondence for $a > 0$ between antipodal, locked, partially coherent and drifting states, with the 2L, L, and D states that are seen for $N = 2$. On the other hand, we found that increasing strength of adaptivity $|a|$ leads to larger locking regions for $N = 2$, whereas this effect does not appear to be present anylonger for $N = 50$ oscillators when $a < 0$.

We point out some similarities between the system we studied here and other systems studied previously in literature. These systems are retrieved from our model (5), which is most adequately seen in the original form of the model where adaptivity is not rescaled yet: Letting $a_0 = 0$ with $\alpha = \beta = 0$, we recover the model Eqs. (3) and (4) studied by Seliger *et al.*, Ref. 8. Similarly, if we set $a_0 = 0$ with $\omega_1 = \ldots = \omega_N = 0, a_1 = 1$, we recover the model by Berner *et al.*[10]. Our adaptation rule generalizes the one in Ref. 8 by inclusion of an adaptation shift $\beta \neq 0$, in accordance to Ref. 10 (e.g., in the Hebbian, STDP, and anti-Hebbian case); however, in contrast to Ref. 10, we introduced a nontrivial adapation offset a_0 and an adaptation strength a_1; this choice enabled us to systematically deviate from the classical Kuramoto-Sakaguchi model with stationary coupling, and thereby, to address the question how variation of the level of adaptivity impacts the dynamics of the network. Moreover, including non-identical frequencies ($\omega \neq 0$) breaks certain symmetries of the system, which distinguishes our study from Ref. 10 and enables us to study the size of the locking region in particular. Finally, note that the choice $a_0 = 1$ does not allow us to retrieve the model in Ref. 8 as $a_0 \to 0$ constitutes a singular limit.

Nevertheless, some of the basic dynamic behavior, such as the presence of frequency locking or antipodal or antiphasic clusters states seen in Ref. 10 naturally carry over to our system as long as intrinsic frequencies are kept relatively close to each other. However, the breaking of the symmetry by forcing a non-zero frequency mismatch $\omega \neq 0$ opens the possibility for bifurcations leading to novel states, e.g., the Hopf bifurcations producing small amplitude librations and the associated period-doubling cascade reported in this study. Furthermore, we mention a very recent study[43] which includes an analysis of our system with $a_0 = 0$ and $a_0 = 1$ in the slowly adapting limit where $\varepsilon \to 0$. This analysis results in a planar problem for the coupling dynamics in separation; as such, the resulting reduced dynamics cannot display a transition to chaos or intriguing phenomena concerning mixed oscillations with librations and rotations seen here.

Future research may study adaptive Kuramoto-Sakaguchi oscillator networks with larger oscillator numbers. To this end, it would be desirable to carry out further simulations, for instance to see if complex dynamics such as the period-doubling cascade reported here for the case of a directed adaptive network with $N = 2$ oscillators and $\beta \neq 0, \pi$ (Sec. III C) prevails for larger networks. Importantly, it would be desirable to develop a (finite) mean-field theory as well as a description for (5) in the continuum limit, e.g., using a formalism based on graphons/graphops[44–46], to study the dynamics for Eqs.(5) for large N. We leave these problems open for future studies.

VI. ACKNOWLEDGEMENTS

We thank M.P. Sørensen, C. Bick, S. Yanchuk and for useful discussions and comments throughout this study, and C. Bick for helpful correspondence. We acknowledge the DTU International Graduate School for support via the EU-COFUND project "Synchronization in Co-Evolutionary Network Dynamics (SEND)".

Appendix A: Symmetries

Eqs. (6) exhibit various symmetries that we survey here. The following symmetries allow us to reduce the α, β parameter range:

$$(a, \beta) \mapsto (-a, \beta + \pi) \tag{A1}$$
$$(a, \alpha, \phi) \mapsto (-a, \alpha + \pi, \phi + \pi) \tag{A2}$$
$$(\alpha, \beta, \kappa_{12}, \kappa_{21}) \mapsto (-\alpha, -\beta, \kappa_{21}, \kappa_{12}) \tag{A3}$$

Moreover, the following symmetries about the ω, a axes are visible in all stability diagrams:

$$(\phi, \omega, \kappa_{12}, \kappa_{21}) \mapsto (-\phi, -\omega, \kappa_{21}, \kappa_{12}) \tag{A4}$$
$$(a, \phi, \kappa_{12}, \kappa_{21}) \mapsto (-a, -\phi + \pi, \kappa_{21}, \kappa_{12}) \tag{A5}$$

As mentoned in the text, the $\omega \mapsto -\omega$ symmetry defined by (A4), (27) or (39) leaves equilibria of Eqs. (6), their types and their stabilities unchanged. Similarly, the $a \mapsto -a$ symmetry defined by the transformation in (A5), (28) or (40) also preserves equilibria of Eqs. (6), but the stabilities and bifurcations of these equilibria need to be discussed. For this, we look at the eigenvalues of the Jacobian specified in (31). Clearly, the SN condition $0 \neq \mu^2 = \delta$ is equivalent to

$$0 = aB - A \tag{A6}$$

if condition (A6) is fulfilled, then it is still fulfilled after applying the symmetry, since the symmetry leaves B unchanged and only inverts the sign of a and A. Looking at Hopf bifurcations, $\mu = 0$ in (32a) is a necessary condition for a Hopf point. If $\mu = 0$ is fulfilled, it is clearly not fulfilled after the symmetry is applied, since the symmetry inverts the sign of A. In summary, the symmetry (40) preserves SN, but not Hopf bifurcations, which agrees with what we see in the stability diagrams.

Finally, the following symmetries are not exploited in the text but mentioned here for the sake of completeness:

$$(\alpha, \beta, \phi) \mapsto (\alpha + \pi, \beta + \pi, \phi + \pi) \tag{A7}$$
$$(\alpha, \omega, \varepsilon, t) \mapsto (\alpha + \pi, -\omega, -\varepsilon, -t) \tag{A8}$$
$$(a, \omega, \varepsilon, \phi, t) \mapsto (-a, -\omega, -\varepsilon, \phi + \pi, -t) \tag{A9}$$
$$(\alpha, \omega, \varepsilon, t) \mapsto (\alpha + \pi, -\omega, -\varepsilon, -t) \tag{A10}$$

REFERENCES

[1] Steven H. Strogatz. *Sync: The Emerging Science of Spontaneous Order*. 2003.

[2]A. Pikovsky, M. Rosenblum, and J. Kurths. *Synchronization. A universal concept in nonlinear sciences*. Cambridge University Press, New York, NY, USA, 2001.

[3]W. Singer and C. M. Gray. Visual feature integration and the temporal correlation hypothesis. *Ann Rev Neurosci*, 18:555–586, 1995.

[4]P. J. Uhlhaas and W. Singer. Neural synchrony in brain disorders: relevance for cognitive dysfunctions and pathophysiology. *Neuron*, 52(1):155–68, 2006.

[5]Martin Rohden, Andreas Sorge, Marc Timme, and Dirk Witthaut. Self-Organized Synchronization in Decentralized Power Grids. *Physical Review Letters*, 109(6):064101, aug 2012.

[6]J. Acebrón, L. Bonilla, C. Pérez Vicente, F. Ritort, and R. Spigler. The Kuramoto model: A simple paradigm for synchronization phenomena. *Reviews of Modern Physics*, 77(1):137–185, apr 2005.

[7]C. Bick, C. Laing, M. Goodfellow, and E.A. Martens. Understanding the dynamics of biological and neural oscillator networks through exact mean-field reductions: a review. *Journal of Mathematical Neuroscience*, 9(10), 2020.

[8]Philip Seliger, Stephen C Young, and Lev S Tsimring. Plasticity and learning in a network of coupled phase oscillators. *Physical Review E*, 65(4):041906, 2002.

[9]Yuri L Maistrenko, Borys Lysyansky, Christian Hauptmann, Oleksandr Burylko, and Peter A Tass. Multistability in the kuramoto model with synaptic plasticity. *Physical Review E*, 75(6):066207, 2007.

[10]Rico Berner, Jan Fialkowski, Dmitry Kasatkin, Vladimir Nekorkin, Serhiy Yanchuk, and Eckehard Schöll. Hierarchical frequency clusters in adaptive networks of phase oscillators. *Chaos*, 29:103134, 2019.

[11]Rico Berner, Jakub Sawicki, and Eckehard Schöll. Birth and stabilization of phase clusters by multiplexing of adaptive networks. *Physical review letters*, 124(8):088301, 2020.

[12]Leonhard Lücken, Oleksandr V Popovych, Peter A Tass, and Serhiy Yanchuk. Noise-enhanced coupling between two oscillators with long-term plasticity. *Physical Review E*, 93(3):032210, 2016.

[13]Tachin Ruangkriengsin and Mason A Porter. Low-dimensional analysis of a kuramoto model with inertia and hebbian learning. *arXiv preprint arXiv:2203.12090*, 2022.

[14]Wulfrum Gerstner, Richard Kempter, J. Leo van Hemmen, and Hermann Wagner. A neuronal learning rule for sub-millisecond temporal coding. *Nature*, 383, 1996.

[15]Donald C Michaels, Edward P Matyas, and Jose Jalife. Mechanisms of sinoatrial pacemaker synchronization: a new hypothesis. *Circulation Research*, 61(5):704–714, 1987.

[16]J. Buck and E. Buck. Mechanism of Rhythmic Synchronous Flashing of Fireflies: Fireflies of Southeast Asia may use anticipatory time-measuring in synchronizing their flashing. *Science*, 159(3821):1319–1327, mar 1968.

[17]Steven H Strogatz, Daniel M Abrams, Allan McRobie, Bruno Eckhardt, and Edward Ott. Theoretical mechanics: crowd synchrony on the Millennium Bridge. *Nature*, 438(7064):43–4, nov 2005.

[18]Tal Danino, Octavio Mondragón-Palomino, Lev Tsimring, and Jeff Hasty. A synchronized quorum of genetic clocks. *Nature*, 463(7279):326–30, jan 2010.

[19]Christiaan Huygens. *Oeuvres Completes*. Swets & Zeitlinger Publishers, Amsterdam, 1967.

[20]Kurt Wiesenfeld, Pere Colet, and Steven Strogatz. Frequency locking in Josephson arrays: Connection with the Kuramoto model. *Physical Review E*, 57(2):1563–1569, feb 1998.

[21]Annette F Taylor, Mark R Tinsley, Fang Wang, Zhaoyang Huang, and Kenneth Showalter. Dynamical quorum sensing and synchronization in large populations of chemical oscillators. *Science (New York, N.Y.)*, 323(5914):614–7, jan 2009.

[22]Dumitru Călugăru, Jan Frederik Totz, Erik A. Martens, and Harald Engel. First-order synchronization transition in a large population of relaxation oscillators. (September):1–8, 2018.

[23]S Danø, P G Sørensen, and F Hynne. Sustained oscillations in living cells. *Nature*, 402(6759):320–2, nov 1999.

[24]Thomas M Massie, Bernd Blasius, Guntram Weithoff, Ursula Gaedke, and Gregor F Fussmann. Cycles, phase synchronization, and entrainment in single-species phytoplankton populations. *Proc. Natl. Acad. Sci.*, 107(9):4236–41, mar 2010.

[25]Johannes Klinglmayr, Christoph Kirst, Christian Bettstetter, and Marc Timme. Guaranteeing global synchronization in networks with stochastic interactions. *New Journal of Physics*, 14(7):073031, 2012.

[26]Thilo Gross and Bernd Blasius. Adaptive coevolutionary networks: a review. *Journal of the Royal Society . . .* , 2008.

[27]Erik Andreas Martens and Konstantin Klemm. Transitions from trees to cycles in adaptive flow networks. 5(November):1–10, 2017.

[28]Erik Andreas Martens and Konstantin Klemm. Cyclic structure induced by load fluctuations in adaptive transportation networks. In István Faragó, Ferenc Izsák, and Péter L. Simon, editors, *Progress in Industrial Mathematics at ECMI 2018*, pages 147–155. Springer International Publishing, 2019.

[29]*(submitted) arXiv:*.

[30]Humberto Mestre, Ting Du, Amanda M Sweeney, Guojun Liu, Andrew J Samson, Weiguo Peng, Kristian Nygaard Mortensen, Frederik Filip Stæger, Peter A R Bork, Logan Bashford, Edna R Toro, Jeffrey Tithof, Douglas H Kelley, John H Thomas, Poul G Hjorth, Erik A Martens, and Rupal I Mehta. Cerebrospinal fluid influx drives acute ischemic tissue swelling. *Science (New York, N.Y.)*, 367(6483):eaax7171, 2020.

[31]Ting Du, Humberto Mestre, Benjamin T Kress, Guojun Liu, Amanda M Sweeney, Andrew J Samson, Martin Kaag Rasmussen, Kristian Nygaard Mortensen, Peter A R Bork, Weiguo Peng, Genaro E Olveda, Logan Bashford, Edna R Toro, Jeffrey Tithof, Douglas H Kelley, John H Thomas, Poul G Hjorth, Erik A Martens, Rupal I Mehta, Hajime Hirase, Yuki Mori, and Maiken Nedergaard. Cerebrospinal fluid is a significant fluid source for anoxic cerebral oedema. *Brain*, awab293:1–28, 2021.

[32]The glymphatic system: Current understanding and modeling. *iScience (in press)*, 2022.

[33]Jake P Taylor-King, David Basanta, S Jonathan Chapman, and Mason A Porter. Mean-field approach to evolving spatial networks, with an application to osteocyte network formation. *Physical Review E*, 96(1):012301, 2017.

[34]Brian Skyrms and Robin Pemantle. A dynamic model of social network formation. In *Adaptive networks*, pages 231–251. Springer, 2009.

[35]Wulfram Gerstner and Werner M. Kistler. Mathematical formulations of Hebbian learning. *Biological Cybernetics*, 87(5-6):404–415, 2002.

[36]Alain Goriely, Ellen Kuhl, and Christian Bick. Neuronal oscillations on evolving networks: dynamics, damage, degradation, decline, dementia, and death. *Physical review letters*, 125(12):128102, 2020.

[37]Note that this property is due to the model's special form that is invariant with regards to stretching time; other models, e.g., with intrinsic dynamics of the form $\dot{\phi}_l = f(\phi_l) + \sum_l g(\phi_l, \phi_m)$ do not necessarily share this property, an example being the Theta neuron model.

[38]Y. Kuramoto. *Chemical oscillations, waves, and turbulence*. Springer-Verlag, New York, 1984.

[39]S. H. Strogatz. From Kuramoto to Crawford: exploring the onset of synchronization in populations of coupled oscillators. *Physica D*, 143:1–20, 2000.

[40]J. Guckenheimer and Y. Kuznetsov. Bautin bifurcation. *Scholarpedia*, 2007.

[41]A. Dhooge, W. Govaerts, Yu A. Kuznetsov, H. G.E. Meijer, and B. Sautois. New features of the software MatCont for bifurcation analysis of dynamical systems. *Mathematical and Computer Modelling of Dynamical Systems*, 2008.

[42]Benjamin Jüttner, Christian Henriksen, and Erik A. Martens. Birth and destruction of collective oscillations in a network of two populations of coupled type 1 neurons. *Chaos: An Interdisciplinary Journal of Nonlinear Science*, 31(February):023141, 2021.

[43]Max Thiele, Rico Berner, Peter A Tass, Eckehard Schöll, and Serhiy Yanchuk. Asymmetric adaptivity induces recurrent synchronization in complex networks. *arXiv preprint arXiv:2112.08697*, 2021.

[44]Marios Antonios Gkogkas, Benjamin Jüttner, Christian Kuehn, and Erik Andreas Martens. Graphop Mean-Field Limits and Synchronization for the Stochastic Kuramoto Model. *Chaos: An Interdisciplinary Journal of Nonlinear Science*, 2022.

[45]Marios Antonios Gkogkas, Christian Kuehn, and Chuang Xu. Continuum limits for adaptive network dynamics. *arXiv preprint arXiv:2109.05898*, 2021.

[46]Christian Kuehn and Chuang Xu. Vlasov equations on digraph measures. *arXiv preprint arXiv:2107.08419*, 2021.